KU LEUVEN

ARENBERG DOCTORAL SCHOOL
Faculty of Engineering Science

Prediction of the sound insulation of layered and periodic wall and floor systems while accounting for modal behaviour

Carolina Decraene

Supervisors:
Prof. dr. ir. E. Reynders
Prof. dr. ir. G. Lombaert

Dissertation presented in partial fulfillment of the requirements for the degree of Doctor of Engineering Science (PhD): Civil Engineering

March 2021

Prediction of the sound insulation of layered and periodic wall and floor systems while accounting for modal behaviour

Carolina DECRAENE

Examination committee:
Prof. dr. ir. C. Vandecasteele, chair
Prof. dr. ir. E. Reynders, supervisor
Prof. dr. ir. G. Lombaert, supervisor
Prof. dr. ir. W. Desmet
Prof. dr. ir. E. Deckers
Dr. ir. A. Dijckmans
(WTCB-CSTC-BBRI, Belgium)
Prof. dr. ir. B. Mace
(The University of Auckland, New Zealand)

Dissertation presented in partial fulfillment of the requirements for the degree of Doctor of Engineering Science (PhD): Civil Engineering

March 2021

© 2021 KU Leuven – Faculty of Engineering Science
Uitgegeven in eigen beheer, Carolina Decraene, Kasteelpark Arenberg 40, bus 2448, B-3001 Leuven (Belgium)
(Belgium)

Alle rechten voorbehouden. Niets uit deze uitgave mag worden vermenigvuldigd en/of openbaar gemaakt worden door middel van druk, fotokopie, microfilm, elektronisch of op welke andere wijze ook zonder voorafgaande schriftelijke toestemming van de uitgever.

All rights reserved. No part of the publication may be reproduced in any form by print, photoprint, microfilm, electronic or any other means without written permission from the publisher.

Preface

"*In research, result and effort are not always directly proportional.*"

. . . , which lead to a confusing mix of laughter and frustration in the past four years. Without willpower and support, I would not have been able to finish this project. In this preface, I take the opportunity to acknowledge the people, who helped me complete my goal.

I would like to express my deepest gratitude to my supervisors, Prof. Edwin Reynders and Prof. Geert Lombaert, for giving me a chance to work at the Structural Mechanics Section. They guided me throughout this PhD project via monthly progress meetings, in which they helped me with their expert technical knowledge.

I would like to extent my gratitude to the members of the examination committee: Dr. Arne Dijckmans, Prof. Wim Desmet, Prof. Elke Deckers and Prof. Brian Mace. Thank you for reading my thesis and your insightful comments. I would like to acknowledge Dr. Arne Dijckmans and Prof. Wim Desmet for being part of the Supervisory Committee of my thesis. My best wishes to Prof. Brian Mace as well, who hosted my visit at the University of Auckland. I would like to thank Prof. Vandecasteele for chairing the preliminary and the public doctoral defence.

This research was funded by a PhD Fellowship (fundamental research) from the Research Foundation – Flanders (FWO) and by an ERC Starting Grant from the European Research Council provided to Prof. Edwin Reynders under the Horizon 2020 framework program, project 714591 VirBAcous. Moreover, the visit at the University of Auckland was funded by a grant for a long stay abroad of the FWO. The financial support of the FWO and the ERC is gratefully acknowledged.

I enjoyed being part of the Structural Mechanics Section. Many friendships were formed during the years. We went cycling in Bruges as was tradition.

We started the Christmas Decoration Contest between offices, which is already organized five times in a row. We were almost sinking in an inflatable rubber boat in the ditch before the department. We appointed each week a 'victim' to make desserts for the next Friday for a while: ranging from two failed cakes and a dubious Greek dessert to almost divine tiramisu. We tried to beat another section with laser shooting. I am quite sure, we failed in this. We dined and drank together on conferences, had barbecues, went to weddings together,... For all those moments, I would like to acknowledge my colleagues: Bram, Cédric, Christiaan, Costas, Dimitris, Eline, Geert, Giancarlo, Guido, Hernan, Jan, Jacinto, Jasper, Jef, Jie, Jonas, Klaus, Kristof, Manthos, Matthias, Pengchao, Pieter, Stijn, Ramses, Wannes. Special thanks to the Alma crew. Good luck to the new people at the section: Daniele, Paul, Bruno, Sarah, Mina and Menno. I would like to thank Ann and Rita for handling all the administrative work, Freddy for blasting the dust out of my laptop in times of need and Danny for the talks about Formula 1.

Ik wil graag mijn familie en vrienden bedanken voor de steun. Mijn diepste dank aan mijn twee zussen, Francesca en Lisa, op wie ik altijd kan terugvallen. Weet dat jullie ook altijd bij mij terecht kunnen. Hopelijk dragen we binnenkort alle drie 'dr.' voor onze naam. Veel dank ook aan mijn ouders, Kristel en Bruno. Bedankt voor jullie advies in tijden van nood en mij te helpen mijn weg te vinden.

Glenn, van mij krijg je je eigen paragraaf in deze tekst. We hebben onze geloftes al afgelegd en het is geen geheim dat jij mijn grootste steun bent. Bedankt voor de nachtelijke wandelingen en me te overtuigen om door te gaan. Bedankt om mijn gedachten te verzetten. Bedankt om naar mijn geklaag te luisteren over al die jaren. Dit is als een afgesloten hoofdstuk en ik kijk uit naar de volgende dat we samen gaan beleven.

Carolina Decraene, Mechelen, February 2021

Abstract

Lightweight systems such as cross-laminated timber elements, sandwich panels, gypsum board walls, ... are emerging in building construction. Because of their relatively low weight and complex vibro-acoustic behaviour, achieving a sufficient level of sound insulation with such systems is however challenging. The aim of this research is to develop a sound transmission loss prediction method, which exhibits similar accuracy as a comparable numerical tool so as to avoid the need of extensive experimental prototype testing in a transmission suite, but proves to be more efficient allowing it to be used as a design tool. The new method considers a model of the transmission suite, consisting of a source room, the wall or floor and the receiver room. As a result, two novel prediction tools were developed in this PhD project for two different applications: (1) thick and layered building elements and (2) periodic building elements.

At high frequencies, the sound transmission loss through thick or layered structures can be computed with high accuracy in the frequency-wavenumber domain using the semi-analytical transfer matrix method, but it has important limitations. First, the system is assumed to be of infinite extent. At lower frequencies however, neglecting the modal behaviour of the wall can lead to large prediction errors. Second, only the mean of the sound transmission loss can be computed by the transfer matrix method, while the variance, inherent to the diffuse field assumption in the rooms, can not be obtained. Therefore, the transfer matrix approach is extended in two ways. The modal behaviour of rectangular walls and floors with simply supported boundary conditions is approximately accounted for by means of an approximate modal transfer matrix method. Using the diffuse reciprocity relationship, a hybrid approximate modal transfer matrix - statistical energy analysis method is then developed, enabling the rooms to carry a diffuse field (as in statistical energy analysis), while modelling the finite-sized wall deterministically with the modal transfer matrix method. The important advantage of the statistical room models is that the uncertainty on the transmission loss predictions due to the assumption of diffuse sound fields in the rooms, can be assessed. The approach is validated

against alternative numerical prediction models and experimental data.

The application of the proposed approach is however limited to thick and layered structures such as sandwich panels or laminated glazing. Therefore, the extension towards more complicated, finite-sized building elements which exhibit spatial periodicity, is considered in this work by invoking periodic structure theory. A hybridization between periodic finite element modelling and statistical energy analysis is achieved. Modal behaviour is accounted for within the periodic structure theory by combining the propagating waves resulting from the free wave propagation analysis of the periodic unit cell, into standing waves, which satisfy the simply supported boundary conditions. A spatial Fourier transformation of the system of equations allows for a fast conversion of the mode shapes of the unit cell to the entire finite-sized structure. The methodology is illustrated by verifying the predicted sound insulation for two orthotropic and two periodic structures with alternative predictions involving a full finite element model of the entire structure, and validating the results with experimental data.

Beknopte samenvatting

Lichte bouwsystemen zoals kruislaaghout elementen, sandwich panelen, gipsplaat wanden, ... zijn in opkomst in de bouwsector. Door hun lage massa en complexe dynamische gedrag is het echter een uitdaging om een voldoende geluidisolatie te behalen met zulke systemen. Het doel van dit onderzoek is om een voorspellingsmethode voor de geluidstransmissie te ontwikkelen die even accuraat is als een gelijkaardige numerieke methode om uitgebreid experimenteel prototype testen te vermijden in de transmissiekamer, maar tegelijkertijd ook sneller is om te worden gebruikt als een ontwerptool. De nieuwe methode beschouwt een transmissiekamer, die bestaat uit de zendruimte, de muur of vloer en de ontvangstruimte. Het resultaat van dit doctoraatsproject zijn twee nieuwe voorspellingsmethodes voor twee verschillende toepassingen: (1) dikke en gelaagde bouwsystemen en (2) periodische bouwsystemen.

De geluidisolatie doorheen dikke en gelaagde structuren kan bij hoge frequenties accuraat berekend worden in het frequentie-golfgetal domein met de transfer matrix methode, maar de methode heeft enkele belangrijke beperkingen. Ten eerste wordt aangenomen dat het element oneindige afmetingen heeft. Bij lagere frequenties kan het negeren van het modale gedrag van de wand echter leiden tot grote afwijkingen in de voorspellingen. Ten tweede kan enkel de gemiddelde geluidstransmissie worden berekend met de transfer matrix methode, terwijl de variantie, eigen aan de aanname van een diffuus veld in de kamers, niet kan worden bepaald. Daarom wordt de transfer matrix methode uitgebreid op twee manieren. Het modale gedrag van de rechthoekige wanden en vloeren met enkelvoudig opgelegde randvoorwaarden wordt benaderend in rekening gebracht door een modale transfer matrix methode. Daaropvolgend, wordt een hybride modale transfer matrix - statistische energie analyse methode ontwikkeld gebruikmakend van de diffuse wederkerigheidsrelatie, zodat er een diffuus veld is in de kamers (zoals in de statistische energie analyse), terwijl de eindige wand deterministisch gemodelleerd wordt met de modale transfer matrix methode. Het belangrijke voordeel van het statistische kamer model is dat de onzekerheid op de geluidstransmissie door de aanname van een diffuus veld in de kamers

kan worden bepaald. De methode wordt geverifieerd door een vergelijking met alternatieve voorspellingsmethodes en experimentele waardes.

De toepassingen van de voorgestelde methode zijn echter beperkt tot dikke en gelaagde structuren zoals sandwich panelen of gelamineerde beglazing. De uitbreiding naar meer complexe, periodische bouwelementen met eindige afmetingen wordt daarom benut met behulp van de periodische structuur theorie. Een hybridizatie tussen periodische eindige elementen en de statistische energie analyse wordt bestudeerd. Modaal gedrag wordt in rekening gebracht door de lopende golven die resulteren van de vrije golfanalyse van de periodische eenheidscel, te combineren tot staande golven die aan de enkelvoudig opgelegde randvoorwaarden voldoen. Een ruimtelijke Fourier transformatie van de vergelijkingen laat een snelle omzetting toe van de modevormen in de eenheidscel tot de modevormen van de volledige, eindige structuur. De methode wordt geïllustreerd door de voorspelde geluidisolatie van twee orthotrope wanden en twee geribde platen te vergelijken met een alternatieve voorspelling, waarvoor een eindige elementen model van de volledige structuur wordt gebruikt, en te valideren a.d.h.v. experimentele data.

List of Symbols

An overview of the adopted symbols, used throughout the text, is listed below. A more thorough discussion of the physical meaning of every symbol is to be found in the text.

Abbreviations

1D	One-Dimenionsal
2D	Two-Dimensional
AN	Analytical
BE	Boundary Element
BCs	Boundary Conditions
CLF	Coupling Loss Factor
CLT	Cross Laminated Timber
CMS	Component Mode Synthesis
DOF	Degree of freedom
EPS	Expanded Polystyrene
FE	Finite Element
FEM	Finite Element Method
FFT	Fast Fourier Transform
fTMM	finite-sized Transfer Matrix Method
mTMM	approximate modal Transfer Matrix Method
PFE	Periodic Finite Element
PFEM	Periodic Finite Element Method
PMMA	Polymethyl Methacrylate
TM	Transfer Matrix
TMM	Transfer Matrix Method
SEA	Statistical Energy Analysis
STL	Sound Transmission Loss
SWL	Sound Power Level

WB	Wave Based
WBM	Wave Based Method
WFE	Wave Finite Element
UC	Unit Cell

General notational conventions

δ_{kl}	Kronecker delta
log	Logarithm to base 10
$\mathbb{R}$	Field of real numbers
$\mathbb{C}$	Field of complex numbers
$\mathbb{N}$	Field of natural numbers
i	imaginary unit
x	Scalar
$\mathbf{x}$	Vector
$\mathbf{X}$	Matrix
$\tilde{\square}$	Variable $\square$ in the wavenumber domain
$\lvert\square\rvert$	Amplitude of a variable $\square$
$\lvert\lvert\square\rvert\rvert$	Euclidean distance of vector $\square$
$\square^*$	Complex conjugate of $\square$
$\langle\square\rangle_{\mathrm{t}}$	Time averaged value of a harmonic variable $\square$
$\langle\square\rangle_{\mathrm{s}}$	Spatial averaged value of a variable $\square$
$\langle\square\rangle_{\mathrm{k}}$	Wavenumber averaged value of a variable $\square$
$\square^{\mathrm{T}}$	Transpose of a matrix $\square$
$\square^{\mathrm{H}}$	Hermitian of a matrix $\square$
$\square^{-1}$	Inverse of a matrix $\square$
$\mathrm{Re}\{\square\}$	Real part of $\square$
$\mathrm{Im}\{\square\}$	Imaginary part of $\square$
$\mathrm{E}[\square]$	Expected value of $\square$
$\mathrm{Relco}[\square]$	Relative covariance of $\square$
(x, y, z)	Global Cartesian coordinate system
$\square_{\mathrm{x}}$	Variable $\square$ according to x-axis
$\square_{\mathrm{y}}$	Variable $\square$ according to y-axis
$\square_{\mathrm{z}}$	Variable $\square$ according to z-axis
$\square_{\mathrm{n}}$	Variable $\square$ according to normal direction

Dynamics

$a_j^{(hl)}$	Complex wave amplitude corresponding to the jth propagating wave with phase combination $(\epsilon_{\mathrm{x}h}, \epsilon_{\mathrm{y}l})$
$\mathbf{a}_{\mathrm{jinc}}$	Generalized coordinates corresponding to a set of jinc basis functions $\boldsymbol{\varphi}_{\mathrm{jinc}}$
a_{tr}	Truncation factor
$\mathbf{b}_{\mathrm{cav}}$	Generalized coordinates corresponding to a set of modeshapes of a hard-walled cavity $\boldsymbol{\chi}_{\mathrm{cav}}$
$\mathbf{C}$	Reduction matrix, obtained via Component Mode Synthesis
$\square_{\mathbf{C}}$	Component Mode Synthesis is applied on $\square$
$\mathbf{D}$	Dynamic stiffness matrix
$\mathbf{D}'$	Dynamic stiffness matrix of the unit cell
$\mathbf{D}_{\mathrm{d}}$	Deterministic dynamic stiffness matrix
$\mathbf{D}_{\mathrm{dir}}$	Direct field dynamic stiffness matrix
$\mathbf{D}_{\mathrm{rev}}$	Reverberant field dynamic stiffness matrix
$\mathbf{D}_{\mathrm{tot}}$	Summation of the direct field dynamic stiffness matrices and the deterministic dynamic stiffness matrices of the overall system
f	Frequency [Hz]
$\mathbf{f}$	Force vector
$\mathbf{f}'$	Force vector of the unit cell
$\mathbf{f}_{\mathrm{dir}}$	Forces generated by the direct field of the subsystem
$\mathbf{f}_{\mathrm{rev}}$	Blocked reverberant forces
g	Green's function in the frequency-spatial domain
$\mathbf{G}$	Global transfer matrix
k	Structural wavenumber [rad/m]
$\mathbf{K}$	Structural stiffness matrix
$\mathbf{K}'$	Structural stiffness matrix of the unit cell
l	Number of half wavelengths according to an indicated direction
$\mathbf{M}$	Structural mass matrix
$\mathbf{M}'$	Structural mass matrix of the unit cell
m_j	Scaling parameter for the basis functions
N	Number of unit cells according to an indicated direction
$\mathbf{q}$	Generalized coordinates corresponding to a set of basis functions $\boldsymbol{\psi}$
$\mathbf{Q}$	Coupling matrix, capturing fluid-structure interaction
r	Indication of the location of the unit cell in the global structure
$\mathbf{R}$	Reduction matrix, imposing the periodic boundary conditions
$\square_{\mathbf{R}}$	Periodic boundary conditions are applied on $\square$
T	Time period [s]
$\mathbf{u}$	Displacement vector

$\mathbf{u}'$	Displacement vector of the unit cell
$\mathbf{v}$	Velocity vector
$\mathbf{Z}$	Mechanical impedance matrix
ϵ	Phase [rad]
$\boldsymbol{\varphi}_{\text{jinc}}$	Set of jinc basis functions
$\boldsymbol{\chi}_{\text{cav}}$	Set of modeshapes of a hard-walled cavity
$\boldsymbol{\psi}$	Set of basis functions
ω	Angular Frequency [radHz]
Ω	Natural frequency [radHz]

Structural properties

D	Bending stiffness of a panel [Nm]
E	Young's modulus [Pa]
G	Shear modulus [Pa]
m	Area density [kg/m^2]
α_∞	Tortuosity of porous layer [-]
η	Damping loss factor [-]
Λ_{l}	Characteristic viscous length of a porous layer [m]
Λ_{t}	Characteristic thermal length of a porous layer [m]
ν	Poisson's ratio [-]
ρ	Density [kg/m^3]
σ	Flow resistivity of porous layer [Ns/m^4]
ϕ	Porosity of porous layer [-]
$\underline{\square}$	Complex variable to account for damping: $\square \cdot (1 + \mathrm{i}\eta)$

Geometric properties

l	Length of the unit cell [m]
L	Length of the structure [m]
L_{cav}	Cavity dimension [m]
S	Surface area [m^2]
t	Thickness [m]

Room properties

c_a	Speed of sound [m/s]
k_a	Acoustic wavenumber [rad/m]
$n_{\mathrm{a},k}$	Modal density of room k [#/Hz]
$T_{\mathrm{a},k}$	Reverberation time of room k [s]
V_k	Volume of room k [m^3]
Z_c	($= \rho_\mathrm{a} c_\mathrm{a}$) characteristic impedance of air [Pa s/m]
Γ_a	($= \mathrm{i}k_\mathrm{a}$) Propagation constant [rad/m]
$\eta_{\mathrm{a},k}$	Damping loss factor of a room k [-]
ρ_a	Air density [$\mathrm{kg/m}^3$]

Acoustic variables

E	Total energy [J]
L_P	Sound Power Level [-]
I	Sound Intensity [$\mathrm{W/m}^2$]
p	Acoustic pressure [Pa]
P	Power [W]
R	Sound transmission loss [dB]
z	Radiation impedance, normalized to the characteristic impedance of air Z_c [-]
η_{kl}	Coupling loss factor between subsystems k and l [-]
σ	Radiation efficiency [-]
σ_{L_P}	Standard deviation of the sound power level [-]
σ_R	Standard deviation of sound transmission loss [-]
σ_τ	Standard deviation of sound transmission [-]
τ	Sound transmission [-]

Contents

Abstract iii

Beknopte samenvatting v

List of Symbols vii

Contents xiii

List of Figures xvii

List of Tables xxi

1 Introduction 1
- 1.1 Problem outline . . . 1
- 1.2 Research context . . . 5
- 1.3 Objectives, methodology and contributions . . . 10
- 1.4 Organization of the text . . . 13

2 The hybrid det-SEA approach 15
- 2.1 Introduction to the hybrid framework . . . 15
- 2.2 General description of the hybrid framework . . . 18
  - 2.2.1 Assembling the equations of motion . . . 18
  - 2.2.2 The direct field reciprocity relationship . . . 20
- 2.3 Conservation of energy . . . 21
  - 2.3.1 Expressions for the power flows . . . 22
  - 2.3.2 Assembling the power balances of the subsystems . . . 24
- 2.4 A hybrid framework for the acoustic performance of building elements . . . 24
  - 2.4.1 Airborne sound prediction . . . 24
  - 2.4.2 Structure borne sound prediction . . . 27

2.5 General expressions for the direct field and deterministic dynamic stiffness matrix . . . 29
2.5.1 Defining the generalized coordinates . . . 29
2.5.2 The deterministic dynamic stiffness matrix . . . 31
2.5.3 The direct field dynamic stiffness matrix via a formulation in the wavenumber domain . . . 31
2.5.4 The direct field dynamic stiffness matrix via the wavelet approach . . . 35
2.6 Conclusions . . . 36

3 Layered building elements 39
3.1 Introduction . . . 39
3.2 General description of the conventional Transfer Matrix Method 40
3.2.1 Assembling the system of equations . . . 40
3.2.2 Airborne sound prediction . . . 46
3.3 Accounting for finite size effects . . . 48
3.3.1 Spatial windowing technique . . . 49
3.3.2 Approximating modal behaviour . . . 53
3.4 Hybridization of the Transfer Matrix Method and Statistical Energy Analysis . . . 56
3.4.1 Defining the generalized coordinates . . . 57
3.4.2 The deterministic dynamic stiffness matrix . . . 58
3.4.3 The direct field dynamic stiffness matrix . . . 59
3.5 Validation examples . . . 62
3.5.1 Sound transmission loss . . . 62
3.5.2 Radiated sound from a mechanically excited plate . . . 75
3.6 Conclusions . . . 80

4 Periodic building elements 83
4.1 Introduction . . . 83
4.2 General description of periodic structure theory . . . 84
4.2.1 Equations of motion of the periodic unit cell . . . 84
4.2.2 Airborne sound prediction . . . 86
4.3 Predicting the modal properties of a finite wall or floor using periodic structure theory . . . 87
4.4 Deterministic and direct field dynamic stiffness matrices . . . 92
4.5 Practicalities of the implementation . . . 95
4.6 Validation examples . . . 101
4.6.1 CLT panels . . . 102
4.6.2 Rib-stiffened panels . . . 109
4.7 Projection on sinusoidal basis functions . . . 115
4.8 Conclusions . . . 117

5 Conclusions and future research **119**
5.1 Conclusion of the PhD project 119
5.1.1 The mTM-SEA approach 119
5.1.2 The PFE-SEA approach 120
5.2 Recommendations for future research 121

Bibliography **125**

Curriculum vitae **137**

List of Figures

1.1 The general problem statement in building acoustics, illustrated for a school building [101]. 1
1.2 Examples from recent building developments [5, 7, 28]. 2
1.3 Examples of wooden building developments using CLT [40, 46]. 3
1.4 Representation of transmission paths for airborne sound transmission inside a building. 4
1.5 A new lightweight timber frame concept, as proposed in [30]. . 4
1.6 Reference curve of the STL of (a) a homogeneous, thin and infinite panel and [116] (b) a homogeneous, thin and finite panel [104]. 6

2.1 Measured sound pressure in a uniform room and a room with added small acoustic point masses, excited by a harmonic volume acceleration source at a frequency of 50 Hz [86]. 16
2.2 Measured sound pressure in a uniform room and a room with added small acoustic point masses, excited by a harmonic volume acceleration source at a frequency of 250 Hz [86]. 16
2.3 A system, composed of multiple subsystems, of which some are modelled statistically and others deterministically [103]. 17
2.4 Illustration of the direct field and the reverberant field for a subsystem, bounded by deterministic boundaries and random boundaries [103]. 18
2.5 The DOFs **q** describe the response of the deterministic subsystem and of the junction between statistical subsystems [102]. 19
2.6 Illustration of the ensemble energy flows within a stochastic subsystem (adapted from [103]). 21
2.7 (a) A section of the KU Leuven Laboratory of Acoustics [116]. (b) A plexiglass panel is built into the transmission opening [86]. 25
2.8 The first 12 identified mode shapes of a rib-stiffened panel, found via an experimental modal analysis [87]. 30

2.9 The free-field pressure field, due to a small baffled piston [41]. . 32
2.10 Illustration of the piece-wise constant Green's function, which is spatially averaged, according to the discretized wavenumber domain [126]. 35

3.1 Examples of multilayered building elements such as a decoupled anchorless hollow brick wall and a floor with floating screed [43]. 39
3.2 A multilayered system, consisting of n infinite, homogeneous layers (Adapted figure from [43]). 41
3.3 Incoming plane wave at an angle θ, exciting the multilayered system (Adapted figure from [43]). 46
3.4 The sound transmission loss of a polymethyl methacrylate panel as predicted by a conventional transfer matrix method, for which the upper bound of the angle of incidence is 89.99999° (black) or 78° (red). 48
3.5 (a)The infinite plate is excited by an incoming plane wave at angle θ. The excitation pressure field is shown in (b) [119]. . . 49
3.6 (a)The infinite plate is excited by an incoming plane wave inducing a travelling wave with trace wavenumber k_{tr}. The velocity field is shown in (b) [119]. 50
3.7 (a) The plate is excited by an incoming plane wave at angle θ. Spatial windowing accounts for diffraction effects. The velicoty field is shown in (b) [119]. 50
3.8 Indication of incidence angle θ and direction α of an incoming wave (adapted figure from [119]). 51
3.9 STL of a panel with $\mathbf{D}_{\mathrm{dir}}$ resulting from the wavelet approach, the approximate asymptotic formulae, the integral formulation of Davy or from the approximate formulae of Davy. 60
3.10 STL of a steel plate (a) as predicted with the mTM-SEA approach, the WBM approach, the AN-SEA approach, the TMM, the fTMM and (b) as measured in the laboratory. 64
3.11 STL of a PMMA panel (a) as predicted with the mTM-SEA approach, the FE-SEA approach, the TMM, the fTMM, and (b) as measured in the laboratory. 65
3.12 STL of a PMMA panel as predicted with the mTM-SEA approach and as measured in the laboratory in 1/3 octave bands. 65
3.13 STL of a perforated brick wall (a) as predicted with the mTM-SEA approach, the FE-SEA approach, the TMM, the fTMM, and (b) as measured in the laboratory. 67
3.14 STL of a perforated brick wall as predicted with the mTM-SEA approach and as measured in the laboratory in 1/3 octave bands. 67

3.15 STL of a sandwich panel (a) as predicted with the mTM-SEA approach, the WB-TMM approach, the TMM, the fTMM and (b) as measured in the laboratory. 69
3.16 STL of a sandwich panel as predicted with the mTM-SEA approach and as measured in the laboratory in 1/3 octave bands. 69
3.17 STL of a double-leaf wall with poro-elastic material in the cavity (a) as predicted with the mTM-SEA approach using an equivalent fluid model or a Biot-Allard model, the TMM, the fTMM and (b) as measured in 1/3 octave bands in [119]. 71
3.18 STL of a double glazing (a) as predicted with the mTM-SEA approach, the WBM, the TMM, the fTMM and (b) as measured in the laboratory. 75
3.19 (a) The absolute value of the out-of-plane displacement in (0.25m,0.25m) of panel due to a harmonic point force with unit amplitude at (0.5m,1m), predicted by the mTMM approach and an analytical method. (b) The corresponding SWL, predicted by the mTMM approach. 77
3.20 SWL of a concrete floor with floating screed due to a tapping machine, predicted by the TMM and the mTMM [114]. 77
3.21 The sound intensity level, due to rain noise on an inclined glass panel, predicted by Radiation model 1, Radiation model 2 and Radiation model 3 in 1/3-octave bands [96]. 79

4.1 Examples of periodic building elements [1, 121]. 83
4.2 (a) Illustration of a periodic unit cell. The selected periodic unit cell is the left-bottom cell (1,1) of the global structure. (b) Indication of the edge and corner DOFs of the periodic unit cell. 84
4.3 The phase constant surfaces of the bending waves of a thin plate. 88
4.4 A contour plot of the absolute displacement spectrum of four travelling waves in the wavenumber domain. A linear combination of these waves results in the Fourier transform of a sinusoidal function. 89
4.5 (a) A travelling wave in the unit cell and (b) the corresponding obtained mode shape in the spatial domain. 95
4.6 STL prediction of a panel by the PFE-SEA approach in case of a coarse and a fine spatial mesh. 96
4.7 (a) A travelling wave and (b) the obtained mode shape in the wavenumber domain. 97
4.8 The absolute value of the piece-wise constant Green's function in the dimensionless wavenumber domain. 97
4.9 STL prediction of a panel by the PFE-SEA approach in case of a coarse and a fine wavenumber mesh for the mode shapes. . . 98

4.10 STL prediction of a panel by the PFE-SEA approach for a wavenumber domain, truncated with $k_{\text{tol}} = 0$ and $k_{\text{tol}} = 10$. . . 98
4.11 STL prediction of a panel by the PFE-SEA approach in case of a coarse and a fine wavenumber mesh for the Green's function. 99
4.12 STL prediction of a panel as predicted by the PFE-SEA approach in case of a shortage of modes. 100
4.13 The normal displacement field of mode (3,2) of the 3-ply X-Y-X CLT panel with a detailed view on the x-displacements throughout the thickness of the panel. 104
4.14 Finite element mesh of (a) the global structure and (b) the unit cell for the 3-ply CLT panel. 105
4.15 STL of a 3-ply CLT panel (a) as predicted with the modal PFE-SEA approach and the FE-SEA approach for the lay out X-Y-X; and (b) as measured in 1/3 octave bands. 106
4.16 STL of a 3-ply CLT panel (a) as predicted with the modal PFE-SEA approach and the FE-SEA approach for the lay out Y-X-Y; and (b) as measured in 1/3 octave bands. 106
4.17 STL of a 3-ply CLT panel as predicted by the modal PFE-SEA approach for the lay outs X-Y-X and Y-X-Y and as measured in 1/3 octave bands [98]. 107
4.18 STL of a 5-ply CLT panel (a) as predicted with the modal PFE-SEA approach and the FE-SEA approach for the lay out X-Y-X-Y-X; and (b) as measured in 1/3 octave bands. 108
4.19 STL of a 5-ply CLT panel (a) as predicted with the modal PFE-SEA approach and the FE-SEA approach for the lay out Y-X-Y-X-Y; and (b) as measured in 1/3 octave bands. 108
4.20 Illustration of the rib-stiffened panel. Cropping the rib-stiffened gives a 1D periodic structure (adapted figure from [87]). 110
4.21 The mesh of the 1D periodic unit cell, used in the PFE-SEA approach. Shell elements were used for the ribs and base panel. 110
4.22 STL of a 1D periodic rib-stiffened panel (a) as predicted with the modal PFE-SEA approach and the hybrid FE-SEA approach; and (b) as measured. 112
4.23 The mesh of the 2D periodic unit cell for the rib-stiffened panel in the PFE-SEA approach. Shell elements were used for the ribs and base panel. 114
4.24 STL of a rib-stiffened panel with 2D periodicity as predicted with the modal PFE-SEA approach and the hybrid FE-SEA approach. 114
4.25 (a) The finite element mesh of the periodic unit cell of the brick wall. (b) STL of the brick wall as predicted with the sPFE-SEA approach, the FE-SEA approach, the mTMM-SEA approach and the PFE-SEA method. 117

List of Tables

3.1 Computation time for $\mathbf{D}_{\text{dir}}$ using the wavelet approach, the approximate asymptotic formulae, the integral formulation of Davy and the approximate formulae of Davy. 61
3.2 Measured damping loss factors η for the partition walls tested in the KU Leuven Laboratory of Acoustics. 63
3.3 Computation time of the STL for the mTM-SEA method, the FE-SEA method and the fTMM. 66

4.1 Computation time of the mean sound transmission loss for the hybrid PFE-SEA method and the hybrid FE-SEA method. . . 100
4.2 The material properties of spruce joists, according to the longitudinal (L), tangential (T) and radial (R) direction [78]. . 103
4.3 The material properties of (a) the base panel and (b) the steel ribs. The damping loss factor in 1/3 octave bands is given in (c) [87]. 111

Chapter 1

Introduction

1.1 Problem outline

Many people are affected by noise coming from traffic, industrial and construction activities or the neighbourhood. These multiple noise sources cause propagating sound waves, affecting the inhabitants of residential, industrial or school buildings as depicted in figure 1.1. This may result in activity disturbance, social tensions and health problems such as sleep deprivation, damage to hearing

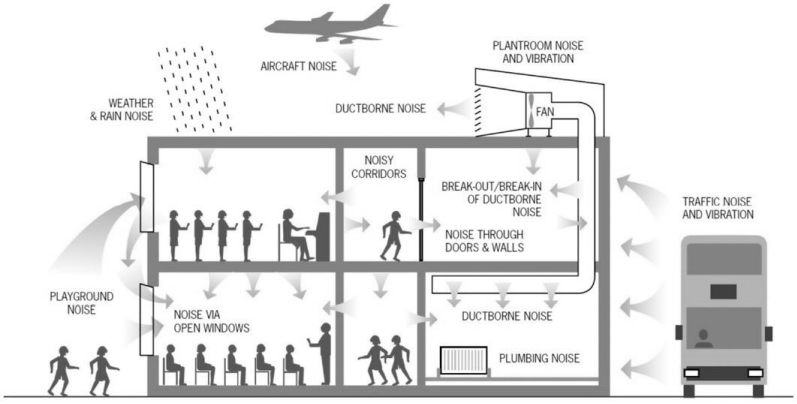

Figure 1.1: The general problem statement in building acoustics, illustrated for a school building [101].

and cardiovascular diseases. The European Environmental Agency considers noise pollution a major environmental health problem and the World Health Organization (WHO) estimates that at least one million healthy life years are lost every year from traffic-related noise alone in Western Europe [127]. An important way of protecting people from noise is by ensuring a sufficient overall sound insulation of buildings and building units.

(a)



(b)



(c)



Figure 1.2: Examples from recent building developments: (a) the office building 'PostX' in Antwerp [5], (b) the residential building 'Balk van Beel' in Leuven [28] and (c) renovation of the residential building 'Ieder zijn huis' in Evere [7].

As each building is a prototype on its own, novel building elements are often developed to meet the functional requirements of the new building. Some examples of recent building developments are shown in figure 1.2. New facade panels were designed for 'PostX' with extra care for the acoustic performance of the panels, because the office building is located next to one of the busiest highways of Belgium (cfr. Fig. 1.2(a)). For the luxurious apartments, seen in figure 1.2(b), the aim was to obtain enhanced acoustic comfort for both airborne and impact noise as defined in the Belgian standard [6]. This was challenging because lightweight gypsum board walls were deployed as separating walls between the apartments to maintain flexibility in the floor plan. Renovation

results in more complicated acoustic problems. The renovation project that is displayed in figure 1.2(c), was particularly challenging as the retrofitted apartments needed to satisfy the current standards, within the given geometric scheme. The main concern was the poor sound insulation of the facade panels and in between the apartments. Again, specially designed sandwich panels with a concrete layer were used during the renovation to preserve the architectural appearance of the building and extra attention was given to the multiple transmission paths in between the apartments. In addition, innovative prefab construction systems with attention for durability are emerging in Belgium. Cross Laminated Timber (CLT) for instance is a wooden construction technique, which is used to construct multi-story wooden buildings as shown in figure 1.3. Issues, regarding fire resistance and the acoustic performance of the lightweight CLT panels, are still investigated.

(a)  (b) 

Figure 1.3: Examples of wooden building developments using CLT: (a) student housing 'Woodskot' in Anderlecht [40]; (b) an 80-level residential building to be built in 2022 in Antwerp [46].

In practice, extensive numerical modelling is avoided in building acoustics due to the computational cost. ISO 12354 is an aim to estimate the acoustic performance by using measured data in the laboratory [51, 52]. The approach in ISO 12354 is a simplified Statistical Energy Anlysis (SEA) model which enables to incorporate measured quantities in the laboratory in the prediction. ISO 12354-1 and ISO 12354-2 handle respectively airborne and structure-borne sound transmission. Airborne transmission arises when a wall or floor is excited by the sound wave field in the room, while structure-borne transmission occurs when power is directly 'injected' into the wall or floor by an impact (e.g. footfall noise) or structural vibrations generated by a vibrating structure such as a washing machine. The sound transmission loss and the normalized impact sound pressure level describe the acoustic performance of a building element for respectively airborne and structure-borne transmission. To obtain the airborne sound insulation or impact sound insulation between two rooms, multiple transmission paths need to be evaluated: the direct transmission path, representing wave propagation across the separating wall or floor, and flanking transmission paths, causing wave propagation via the other transmission

paths (cfr. Fig. 1.4). Flanking sound transmission depends on the geometry of the building, characteristics of the considered junction and the direct sound insulation of the involved building elements. Empirical models are available to estimate the sound insulation of homogeneous structural elements [51, 52]. The standards also include models for massive wall, timber frame and CLT panel junctions.

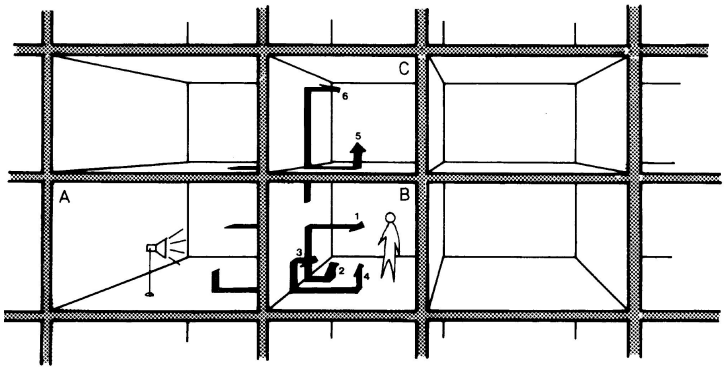

Figure 1.4: Representation of transmission paths for airborne sound transmission inside a building, for which path 1 is an example of direct sound transmission, while the other paths (2-6) are examples of flanking sound transmission [116].

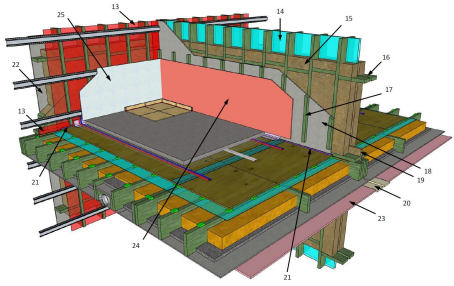

Figure 1.5: A new lightweight timber frame concept, as proposed in [30].

At present, the acoustic design of lightweight built-up, rather than monolithic, wall and floor systems is mostly based on a combination of general design rules and computationally cheap but insufficiently accurate models, necessitating a large number of experimental prototype tests. This trial and error process is quite time consuming. Optimizing such a structure is complex since small details (e.g. the connection between studs and the panels in a gypsum board wall) can have a large effect. Noise propagates through multiple transmission

paths and acoustic performance requirements often conflict with thermal and structural requirements. Consider the joisted floor in figure 1.5 [30]. This floor was designed to satisfy the airborne and impact sound insulation requirements prescribed by the NBN S 01-400-1 standard [6]. In total 30 alternatives were tested with changes in the resilient material, the number of plates, gravel thickness, ... resulting in a novel building concept for the floor element.

The focus of this work is therefore to develop design tools for direct sound transmission prediction, which are sufficiently accurate and efficient enough to be used for the optimization of building elements. Predicting the impact sound radiation, will be touched upon as well, but is not the main focus of this PhD project.

1.2 Research context

Sound transmission occurs when a propagating wave excites a wall or floor, resulting in waves travelling through the structure. Only waves that trigger out-of-plane motion, will in turn excite the adjacent fluid at the receiving side and thus contribute to sound transmission. Acoustic laboratory testing is performed to experimentally determine this sound transmission through a building element. When simulating a transmission suite or room-wall-room system of an acoustic laboratory for the prediction of the sound transmission loss (STL), one of the commonly made assumptions is that the sound field in the source room is a diffuse wave field. A diffuse sound field is a statistical model, consisting of uncorrelated plane waves with equal probability of a sound wave coming from any direction choosing any point in space. The sound field in the rooms can be considered to be homogeneous in the sense that the statistical properties (e.g. the mean and variance of the sound pressure level) are independent of the position in the room [41, 47].

As far as the wall is concerned, the diffuse STL behaviour of a single, acoustically thin, homogeneous panel with infinite lateral dimensions can be summarized as follows. Taking out-of-plane motion into account, only the bending waves contribute to the STL of the panel, while shear and longitudinal waves can be disregarded. Consider a reference curve of the STL of such a panel in figure 1.6(a). At lower frequencies, the STL prediction is mainly determined by the mass per surface area of the panel. Non-resonant sound transmission due to bending waves that have their natural frequencies outside the frequency band of interest, dominates this mass law region. The STL increases with 6 dB

when doubling the frequency. The critical frequency is the lowest frequency, at which coincidence happens. The bending wavelength in the plate corresponds then to the wavelength of the incident acoustic wave and the plate becomes to some extent transparent to the incident waves. At the critical frequency a dip appears in the curve where stiffness and damping have a larger effect than at lower frequencies. From the critical frequency onwards, resonant transmission dominates the curve. The STL curve at and above the critical frequency can be influenced by adding damping.

In reality, the test samples in a laboratory environment have finite dimensions. Figure 1.6(b) shows a typical curve for the STL of a homogeneous, finite panel. Comparing the STL predictions of finite versus infinite structures, only the STL prediction above the critical frequency is equivalent, as the sound radiation of the modes above this frequency is in general not affected by the plate boundaries [47]. This is true when the modal behaviour of the panel doesn't influence the STL. In that case, the panel displays 'high frequency behaviour' and a diffuse vibration field can be assumed in the structure. Below the critical frequency, boundary conditions influence the STL and the STL prediction of a finite and infinite panel do not agree. When the the panel is modally sparse, strong STL dips, caused by resonance of the plate modes, can be distinguished, as noted in figure 1.6(b). In the lower frequencies, the first panel resonance indicates the transition from the stiffness to mass law region. In this so-called stiffness region, the plate does not have modes and the static stiffness determines the STL.

Note that when dealing with lightweight structures which have a higher bending stiffness and lower mass per surface area, the eigenfrequencies of the corresponding modes can shift to higher frequencies into the frequency range of interest.

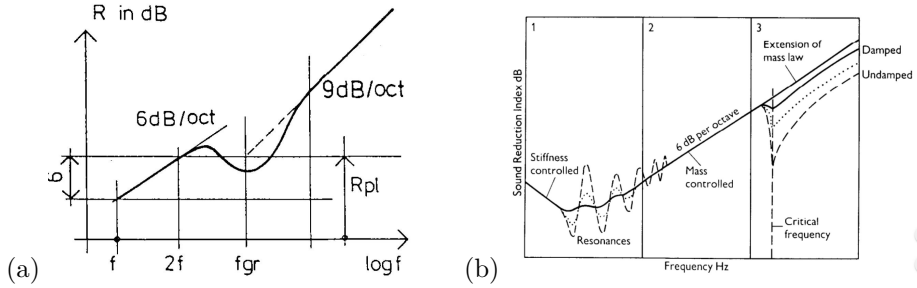

Figure 1.6: Reference curve of the STL of (a) a homogeneous, acoustically thin and infinite panel and [116] (b) a homogeneous, acoustically thin and finite panel [104] in function of frequency.

Below, an overview of existing (semi-)analytical, numerical, statistical and hybrid methods for STL modelling is given.

(semi-)Analytical models

Analytical models make use of simple analytical formulations, reducing the computation time and making them useful to optimize the material properties of structures in favour of the acoustic performance. The main physical phenomena such as the critical frequency or the mass law region, are accounted for [4, 106]. However, the applicability of most analytical methods is limited to homogeneous panels with infinite lateral dimensions.

At first, an analytical model was developed for a thin, homogeneous, infinite panel by Cremer [25]. The bending stiffness of the plate was accounted for by using Kirchhoff's thin plate theory, resulting in the distinctive STL dip at the critical frequency. Coincidence occurs at and above this frequency. However, thickness resonances might influence the STL at higher frequencies. Ljunggren for instance [66] then incorporated shear deformation and rotary inertia by generalizing the STL predictions for infinite thick walls. Thin plate theory has been further extended towards infinite, homogeneous orthotropic walls [44].

Analytical models have also been extensively investigated for the STL prediction of infinite double walls. The first studies considered infinite double walls without structural connections [8, 67, 77]. Sound-absorbing materials in the cavity are modelled as equivalent fluid layers. These models account for phenomena typical for double walls such as mass-spring-mass resonance and cavity resonances [41, 47]. Later on, several theoretical models to incorporate periodically placed studs were investigated, based on a spatial Fourier transform technique [91], in which the flexibility of the stud [18, 122] and finite dimensions of the cavities between the studs [16] can be approximately accounted for. In [69, 70] analytical expressions were derived respectively for two-dimensional periodic orthogonally stiffened panels and for periodic point supported plates, using the Bloch-Floquet theorem. Extension towards predicting the sound transmission loss of sandwich panels, led to multiple analytical expressions [38, 45, 57, 79].

A well-known analytical method to cope with multilayered systems, consisting of fluid, solid or poro-elastic layers of infinite lateral dimensions, is known as the transfer matrix method (TMM) [3, 15, 63]. The method captures the behaviour of the global structure using analytical expressions, describing the wave propagation through one layer and coupling it to the next one. This results in a general framework that can be used to replace the analytical models discussed above. To make the method applicable to a wide range of building elements, it has been expanded in order to include finite size dimensions. Villot

et al. [119] used a spatial windowing technique to take diffraction effects into account. Computing the quadruple integration within this technique is, however, computationally costly. More efficient models have been proposed in [12, 89, 118]. Mind that the TMM with a spatial windowing technique (fTMM) does not include modal behaviour of the wall or floor, as the boundary conditions are not accounted for: a window is placed over an underlying infinite wall.

Numerical models

Whereas the analytical models deal mostly with infinitely sized structures, numerical models account for aspects such as their finite size and boundary conditions, making them more suitable for predictions at low- and medium-frequencies. Numerical methods such as the finite element method (FEM) or boundary element method (BEM) can be deployed for STL predictions. However, straightforward applications are limited to low frequencies as higher frequencies demand a higher number of elements to capture the small wavelength deformations, resulting in higher computation times. Modal decomposition can be used to reduce the number of degrees of freedom of the system.

Finite element and boundary element modelling is not widely used in building acoustics. Nonetheless, both methods allow to account for all details of interest of the finite sized structure. Therefore, a number of authors have used numerical models for the STL prediction of more complicated structures [17, 55, 80, 86, 87, 107, 132], in which the structure is modelled using FEM or BEM.

To reduce the computational effort, Alimonti et al. proposed a coupled FE-TMM for vibro-acoustic systems with acoustic treatment, modelling the acoustic treatment using the TMM [2]. It was assumed that boundary effects in the added treatment are not important. Alternatively, periodic structure theory can be used to reduce the finite element model of the structure to a unit cell (UC), that is repeated within the structure [14, 58, 73, 75, 74]. Applying the Bloch-Floquet theorem to a model of the UC, results in an eigenvalue problem, in function of frequency and phase lags over the unit cell in both directions. Mace and Manconi [71, 72] imposed the periodicity conditions on a finite element model of a unit cell for a two-dimensional periodic structure, to solve the eigenvalue problem for the dispersion relations. These dispersion curves describe the wave propagation within the periodic structure. Yang et al. [130] extended this wave and finite element (WFE) method towards the prediction of the oblique sound transmission for infinitely-sized planar structures. The diffuse transmission was obtained by integration over all plane wave incidence angles. The extended WFE method was subsequently applied for predicting the sound transmission through infinite honeycomb panels and a Gaussian

weighting was applied when integrating the plane wave transmission over all angles of incidence [131]. Christen et al. predicted the sound transmission loss of infinite, planar structures using a WFE approach, while modelling the coupling with the adjacent acoustic volumes analytically [19]. Parrinello and Ghiringhelli [81] combined the TMM and periodic finite element (PFE) modelling for predicting the sound transmission through layered structures considering both homogeneous layers and heterogeneous layers with spatial periodicity. The validation examples considered structures of infinite extent. The approach was recently extended to account for Bloch modes in the periodic layers [82]. Periodic structure theory is also employed by Van Belle et al. [107] to study the effect of damping on the diffuse sound transmission loss of infinite, locally resonant metamaterial plates using the approach of Deckers et al. [31].

Statistical models

A method commonly used to estimate the sound transmission loss of building elements is Statistical Energy Analysis (SEA) [22, 68]. The overall system is divided into multiple modal subsystems (rooms, plate, cavities, ...). As each subsystem only has one degree of freedom, which is the mean total energy, the method is computationally very efficient. Coupling loss factors (CLFs) are used to describe the power transfer between subsystems. Applying conservation of energy to each subsystem then results in a set of linear coupled equations for the subsystem energies. Note that a mean response is predicted using SEA, which considers a population of systems that are nominally identical, but in reality have small differences, due to small imperfections for instance.

Fundamentally, SEA assumes a diffuse wave field in each subsystem. In case of a pure tonal excitation of the SEA subsystem, the variance on the total energy of the subsystem is high when the modal overlap factor of the subsystem is small. This quantity represents the number of modes that contribute to the mean response of the subsystem at a particular frequency. To reduce the uncertainty of the mean response, a higher modal overlap factor is needed or the results can be band-averaged [61]. The validity of the SEA assumptions can be checked via the statistical overlap factor, which indicates the uncertainty of a subsystem to local mass and stiffness variations [86]. If the statistical overlap factor is larger than unity, SEA modelling is typically valid. For acoustic volumes, a diffuse field can alternatively be assumed from the Schroeder frequency onwards [99], at which the variance of the response of the subsystem is small enough.

Both the wall or wall partitions and the rooms of the transmission suite are modelled as diffuse in conventional SEA. Mind that only resonant transmission is considered and that forced or non-resonant transmission needs to be accounted

for artificially [22]. SEA is used to predict the STL of infinite single, double and triple walls [13, 27, 83] and is extended to incorporate the connections between the two leaves [24, 23].

Modelling the transmission suite by means of SEA poses a challenge as the sound field in the rooms can be approximated using a diffuse wave field, whereas the test sample might still be modally sparse. The finite size effects of the wall or floor will then influence the STL prediction. Different modelling strategies are therefore preferred for the wall and rooms when modelling the transmission suite, which is basically a room-wall-room system. Shorter and Langley introduced a framework in which the vibro-acoustic system is subdivided into subsystems. These subsystems can either be modelled deterministically or stochastically [103]. This allows to model the rooms using SEA, assuming a diffuse wave field, while the wall is modelled deterministically. In addition, the hybrid framework offers a general manner to determine the CLF describing the coupling between the two rooms, overcoming the resonant problem of conventional SEA modelling. The diffuse STL follows automatically from the determined CLF. Note that this hybrid approach differs from most methodologies, which compute the diffuse STL via an integration of the oblique sound transmission. However, this integration results in a numerical issue at grazing incidence, which is circumvented by an arbitrary choice of the upper bound of the angle of incidence.

In a hybrid deterministic-SEA (det-SEA) context, the finite element method is a straightforward approach to model the wall [86, 103]. Since both the mean and the variance of the transmission loss can be computed via this hybrid FE-SEA approach [60], the uncertainty on the transmission loss predictions that is inherent to the assumption of diffuse sound fields in the rooms can be assessed [86]. Unlike most methods that account for modal behaviour, the framework allows to account for cross-modal coupling as well. In [20], a hybridization between periodic structure theory and SEA was investigated. Diffraction effects were accounted for using a spatial windowing technique.

1.3 Objectives, methodology and contributions

Objectives

The hybrid framework will be the starting point in this PhD project to develop alternative STL prediction tools. A hybrid FE-SEA approach, for which rooms and wall can be modelled differently, allows to determine statistical parameters, such as mean and variance response of the stochastic subsystems, while avoiding the numerical integration of the oblique sound transmission over all possible

angles of incidence to obtain the diffuse sound transmission loss. However, as stated earlier, FE modelling is less efficient when going up to higher frequencies. So instead of modelling the wall or floor system with finite elements, alternative deterministic models will be explored.

In order to maintain accuracy over a wide frequency range, the modal behaviour of the wall or floor system will be (approximately) accounted for, so that narrow band inspection of the sound transmission loss prediction is possible. This modal behaviour is highly dependent on the boundary conditions. The influence of the boundary conditions on the sound radiation and transmission has been demonstrated in literature [84, 105, 128]. However, there is a lot of uncertainty about the boundary conditions of a wall or floor in situ and in a laboratory environment. It is even possible that a mounted wall or floor has significantly different boundary conditions at each side of the building element. Throughout this PhD project, simply supported boundary conditions are assumed. In this case, the normal displacements at the edges of the wall or floor are restrained. This is a reasonable assumption when the wall or floor is connected to other components at the boundaries [47].

Methodology

Within the frame of this doctoral research, *two novel hybrid methodologies* were developed. First, the transfer matrix method was integrated into the hybrid framework to compute the diffuse sound transmission through finite sized walls and floors that consist of layers of solid, fluid and/or poro-elastic material. By decomposing the displacements of the structure using sinusoidal basis functions, modal behaviour of simply supported structures can be approximately accounted for in this approximated modal TMM (mTMM) [37, 90]. The *hybrid mTM-SEA approach* is a useful and efficient method for layered systems. For complicated building elements, a more general approach might be needed as small details become important for structural transmission. The second method therefore exploits the spatial periodic lay-out of many building elements and is a hybrid framework, which uses periodic finite elements (PFE) to model the wall or floor system. The focus was on including modal behaviour in this *hybrid PFE-SEA method*.

The advantages of each proposed methodology are summarized below:

- The hybrid mTM-SEA approach:

  The advantages of the hybrid mTM-SEA framework that is presented in this work, are in comparison to the TMM and related approaches (1a) that the variance, which is inherent to the diffuse field assumption in

the stochastic subsystems, can be computed at low computational cost, (1b) that interaction between the modes (or in other words cross-modal coupling) is accounted for, while keeping a similar computation cost as in the conventional mTMM; and (2) when compared to the hybrid FE-SEA approach: a substantial increase in computational efficiency when the system is simple enough to be modelled with mTMM.

- The hybrid PFE-SEA approach: The advantages of the hybrid PFE-SEA framework, presented in this thesis, are (1) with respect to the hybrid FE-SEA approach [86]: finite element modelling remains limited to the unit cell; (2) in regard with the PFE-SEA method proposed in [20]: (2a) computational efficiency is gained by performing a modal analysis, which avoids an integration over the phase domain, while also inherently accounting for modal behaviour, and (2b) cross-modal coupling is included; (3) with respect to the WFE approach [130, 131]: (3a) that modal behaviour is included, (3b) that the variance of the sound transmission loss, inherent to the diffuse field assumption, can be computed.

Contributions

The main contributions of the PhD work are summarized below:

- The hybridization of the mTMM and SEA has been achieved in this work for airborne sound prediction and structure borne sound prediction. The method is illustrated by multiple validation examples.
- Modal behaviour is accounted for within the hybrid modal PFE-SEA approach. Free wave propagation of a periodic unit cell results in the dispersion curves of the travelling waves in the structure. Novel is the use of these results to obtain the standing waves for a simply supported structure. The method is verified by comparing the resulting sound transmission loss of the modal PFE-SEA approach with the predictions of a hybrid FE-SEA approach, which is based on a full finite element model of the structure.
- A spatial Fourier transform of the travelling waves of the unit cell in the PFE-SEA approach allows for a quick conversion to the travelling waves of the full structure. The standing waves obtained from these travelling waves are used to compute the direct field response of the rooms. The conversion to the wavenumber domain results in more insight in phenomena such as the radiation of waves in free-field and the combination of travelling waves into standing waves.

- By including modal behaviour in the methodologies, narrow band inspection of the wall or floor systems is possible, resulting in more detailed discussions on the sound transmission loss predictions of the validation examples.
- Multiple approaches to compute the direct field response are considered and compared. The influence of cross-modal coupling, which is the interaction between the modes, is discussed. It is emphasized that in most methodologies cross-modal coupling is ignored.

1.4 Organization of the text

The PhD thesis is partitioned in three main chapters, each introducing a method. Chapter 2 describes the underlying theory of the hybrid framework. Chapters 3 and 4 discuss respectively the hybridization with the transfer matrix method and periodic finite element modelling. Validation examples are included in chapters 3 and 4.

Chapter 1 introduces the challenges in building acoustics and motivates the work presented in this thesis. After presenting the research context, the advantages of the two novel prediction tools are highlighted and the organization of the text is clarified.

Chapter 2 describes first a general formulation for the hybrid framework. In order to do so, the necessary definitions and concepts, used within the hybrid framework, are introduced. It is shown how these concepts are used to elaborate the power flows of the overall system. By applying conservation of energy, the mean total energy of each subsystem can be determined. A straightforward formulation for the CLFs in terms of the deterministic dynamic stiffness matrix and direct field dynamic stiffness matrix follows from this elaboration. Later on, this hybrid framework is applied for sound transmission modelling and the prediction of impact noise within the context of building acoustics. Finally, general expressions for the deterministic dynamic stiffness matrix of the wall and direct field dynamic stiffness matrices of the rooms are derived.

Chapter 3 introduces the conventional transfer matrix method for infinite, layered systems with flat and homogeneous layers. The resulting global transfer matrix is dependent on the material properties of the layers and is defined in terms of frequency and an imposed trace wavenumber. From the global

transfer matrix, the mechanical impedance matrix is derived, which relates the pressures and velocities at both sides of the layered system. Next, two finite size corrections are elaborated: a spatial windowing technique and an approximate modal transfer matrix method. The latter one accounts approximately for modal behaviour by decomposing the displacements using a set of sinusoidal basis functions, which satisfy the simply supported boundary conditions. The trace wavenumbers, necessary to solve for the mechanical impedance matrix, are chosen to be the wavenumbers corresponding to the sinusoidal basis functions. Then, a hybridization between the approximate modal transfer matrix method and statistical energy analysis is achieved. Finally, this novel method is verified by comparing the sound transmission loss results with other prediction tools and validated by comparing the results with experimental data for multiple structures of increasing complexity. The prediction of impact noise, caused by a harmonic point force, is briefly discussed as well.

Chapter 4 considers the integration of periodic finite element modelling into the hybrid framework, invoking the periodic lay-out of most building elements. First, periodic boundary conditions are imposed onto the periodic unit cell. It is then described how the modal properties of the full structure are derived from the free wave propagation analysis of the periodic unit cell. Afterwards, the deterministic and direct field dynamic stiffness matrices are determined using the obtained modal characteristics of the full structure. Practicalities of the implementation of the method are discussed next. Then, the proposed methodology is verified by comparing the sound transmission loss predictions of two orthotropic cross laminated timber panels and two rib-stiffened panels with the results of a hybrid approach, involving a full finite element model, and experimental data. Finally, an alternative approach is discussed, for which the displacements are projected onto a set of sinusoidal basis functions and the deterministic and direct field dynamic stiffness matrix are determined in terms of the corresponding sinusoidal coordinates.

Chapter 5 summarizes the most important conclusions of the work and gives recommendations for future research.

Chapter 2

The hybrid det-SEA approach

2.1 Introduction to the hybrid framework

Consider a vibro-acoustic system, consisting of multiple components. When the dynamic response of a component is dominated by modes with long wavelengths, it displays little sensitivity to small local mass and stiffness variations, and can be defined deterministically for fixed gross mass, stiffness and damping parameters. The component exhibits so-called 'low frequency behaviour'. Such a component is displayed in figure 2.1. Adding local masses changes the sound pressure field little at 50 Hz. The modes dominating the response at higher frequencies, have shorter wavelengths. The component displays 'high frequency behaviour' and becomes highly sensitive to small imperfections, as illustrated in Fig. 2.2. Due to the high sensitivity, the component can be stochastically modelled, using SEA. Modelling the component deterministically is in this case less suitable as (i) a high number of degrees of freedom is required to capture the detailed deformation pattern [34], and (ii) an ensemble of randomized models needs to be considered because of the possibly high sensitivity to small local mass and stiffness variations [9].

Built-up systems consist of multiple components, from which some exhibit low-frequency behaviour, while others exhibit high frequency behaviour. So, the vibro-acoustic system might not be entirely statistical or deterministic. Offering a solution to this mid-frequency problem, Shorter and Langley proposed a flexible framework which allows to introduce deterministic modelling within the SEA paradigm [103].

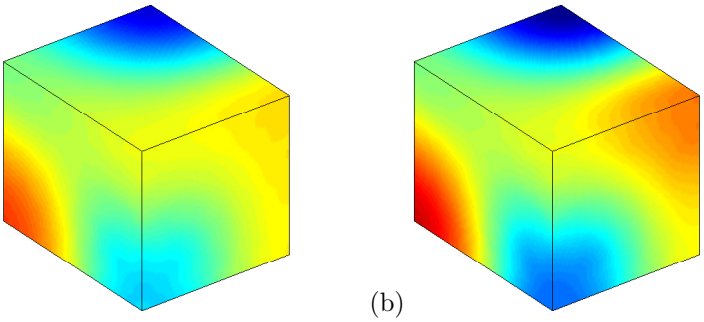

(a) (b)

Figure 2.1: Measured sound pressure on the surfaces of a hard-walled room, excited by a harmonic volume acceleration source at a frequency of 50 Hz: (a) the room is uniform; (b) the room is perturbed by adding small acoustic point masses [86].

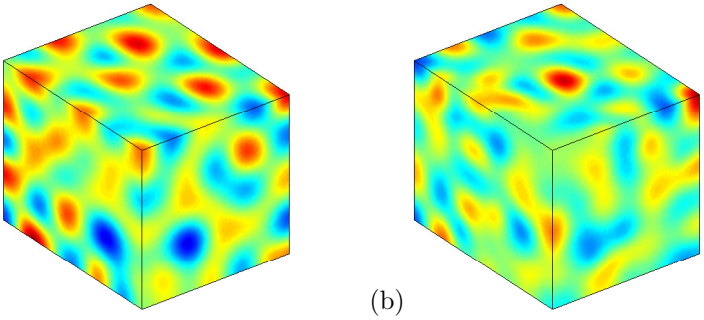

(a) (b)

Figure 2.2: Measured sound pressure on the surfaces of a hard-walled room, excited by a harmonic volume acceleration source at a frequency of 250 Hz: (a) the room is uniform; (b) the room is perturbed by adding small acoustic point masses [86].

Figure 2.3 shows a system, that is subdivided into a number of coupled subsystems. At the excitation frequency, some subsystems exhibit low-frequency behaviour and are modelled deterministically, while others show short wavelength deformation and are modelled statistically. The boundaries of the subsystems can be categorized into three options that are referred to as 'deterministic boundary' regions, 'random boundary' regions and 'connection' regions. When boundaries are known precisely, they are classified as 'deterministic boundary' regions, whereas if the remainder of the boundary is unknown, they are defined as 'random boundary' regions. Power is transferred

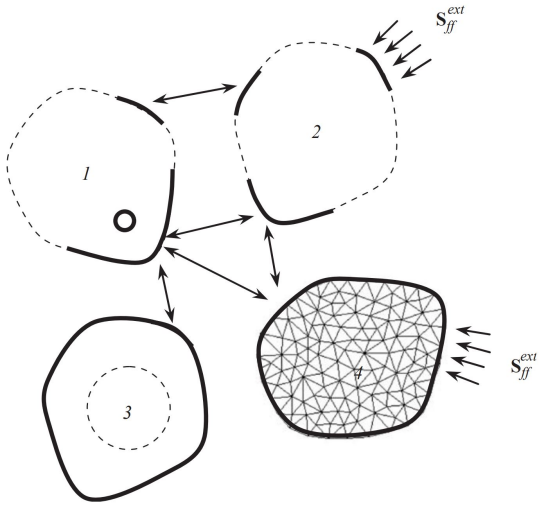

Figure 2.3: A system, composed of multiple subsystems, of which some are modelled statistically (blank) and others deterministically (meshed). Junctions, loads, random boundaries and deterministic boundaries are respectively indicated by double arrows, single arrows, dashed lines and solid lines [103].

into or out of a subsystem due to the coupled subsystems or external loading via the 'connection' regions. The connection regions of different subsystems are coupled by 'junctions', assuming that connection regions of a particular junction have compatible displacement fields. The 'master system' refers to the deterministic subsystems and the junctions between the several subsystems.

Within this framework, it is now clear that components can be deterministic or statistical. The statistical subsystems can be bounded by deterministic boundaries, random boundaries or both, assuming that the properties of the deterministic boundary are known precisely and the properties of the random boundary are highly uncertain. It was shown in [102], that the wave field in such a subsystem, as displayed in Fig. 2.4, can be decomposed into a direct field and a reverberant field. The direct field response describes the outgoing wave field, due to displacements of the deterministic boundary (cfr. fig. 2.4(a)). In other words, it is the response of the subsystem to the displacements at the deterministic boundary in the limit case where the random boundary is absent. It is therefore not dependent on the properties of the random boundary. The reverberant field, shown in figure 2.4(b), is then caused by reflections at this random boundary and highly sensitive to its properties. Satisfying a blocked

boundary condition or in other words zero displacements at the deterministic boundary, the field results in blocked reverberant forces at the deterministic boundary.

Several concepts and terms, necessary to understand the hybrid deterministic-SEA (det-SEA) framework, have been introduced in this section. In section 2.2, the equations of motion of the overall system are discussed and elaborated, with emphasis on treating the random boundaries of the statistical subsystems. Next, conservation of energy is applied to solve the SEA model for the total energies of the subsystems in section 2.3, providing an automatic way to determine the CLFs. Then, it is shown in section 2.4, how the framework can be used to obtain the sound transmission loss (STL) of a building element and the radiated sound power level (SWL) due to structural loading of the building element. Finally, section 2.5 gives general expressions for the deterministic dynamic stiffness matrix of the wall or floor and the direct field dynamic stiffness matrices of the rooms, necessary to solve for the STL and SWL.

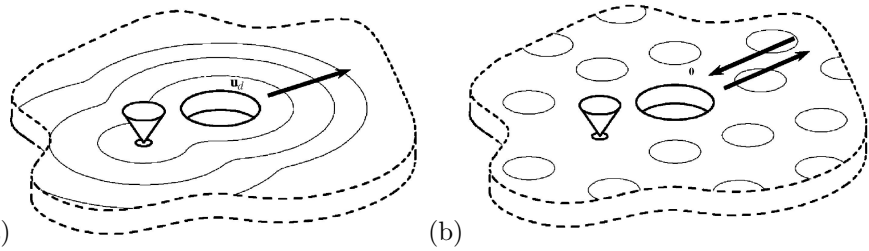

Figure 2.4: Illustration of (a) the direct field and (b) the reverberant field for a subsystem, which is bounded by a deterministic boundary (solid) and a random boundary (dashed) [103].

2.2 General description of the hybrid framework

2.2.1 Assembling the equations of motion

The generalized response degrees of freedom (DOFs) of the master system are collected in a vector $\mathbf{q}(\omega)$, so that the time-domain response is given by $\mathrm{Re}(\mathbf{q}\mathrm{e}^{\mathrm{i}\omega t})$, with t the time, ω the angular frequency and i the imaginary unit. The set of DOFs $\mathbf{q}(\omega)$ does not only include the DOFs of the deterministic subsystems, but also the DOFs of the junctions between the several subsystems, as illustrated in Fig. 2.5. Similarly, the corresponding generalized harmonic

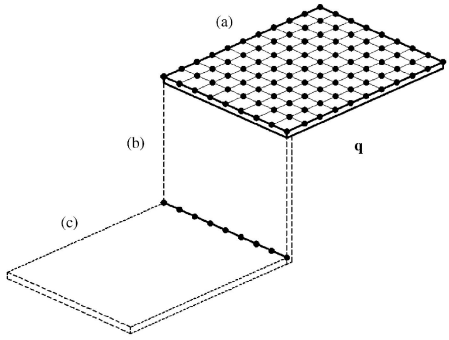

Figure 2.5: The DOFs $\mathbf{q}$ describe the response of the deterministic subsystem (a) and of the junction between statistical subsystems (b) and (c) [102].

loads are collected in the load amplitude vector $\mathbf{f}(\omega)$. The equations of motion of the overall system can then be written as:

$$\mathbf{D}\mathbf{q} = \mathbf{f}, \tag{2.1}$$

with $\mathbf{D}$ the dynamic stiffness matrix at frequency ω. $\mathbf{D}$ may be decomposed into the sum of the deterministic dynamic stiffness matrix $\mathbf{D}_{\mathrm{d}}$, capturing the contribution of the deterministic components, and the dynamic stiffness matrices of the N_{s} stochastic subsystems, with $\mathbf{D}^{(k)}$ the dynamic stiffness matrix of the k-th subsystem:

$$\mathbf{D} = \mathbf{D}_{\mathrm{d}} + \sum_{k=1}^{N_{\mathrm{s}}} \mathbf{D}^{(k)}. \tag{2.2}$$

The dynamic stiffness matrix of each stochastic subsystem k is then decomposed as

$$\mathbf{D}^{(k)} = \mathbf{D}^{(k)}_{\mathrm{dir}} + \mathbf{D}^{(k)}_{\mathrm{rev}}, \tag{2.3}$$

where $\mathbf{D}^{(k)}_{\mathrm{dir}}$ and $\mathbf{D}^{(k)}_{\mathrm{rev}}$ denote respectively the 'direct field dynamic stiffness matrix' and the 'reverberant field dynamic stiffness matrix', describing the direct field and reverberant field response of subsystem k [102, 103]. This decomposition allows to capture the deterministic part of $\mathbf{D}^{(k)}$ into $\mathbf{D}^{(k)}_{\mathrm{dir}} = \mathrm{E}[\mathbf{D}^{(k)}]$ with $\mathrm{E}[\square]$ the ensemble average of $\square$, while the random part of $\mathbf{D}^{(k)}$ is described by $\mathbf{D}^{(k)}_{\mathrm{rev}}$. The equations of motion of a random subsystem are then reformulated, so that:

$$\mathbf{D}^{(k)}_{\mathrm{dir}}\mathbf{q} = -\mathbf{f}^{(k)}_{\mathrm{dir}} \tag{2.4}$$

$$= -\mathbf{f}^{(k)} + \mathbf{f}^{(k)}_{\mathrm{rev}}, \tag{2.5}$$

where the reverberant blocked forces are defined as $\mathbf{f}_{\text{rev}}^{(k)} := -\mathbf{D}_{\text{rev}}^{(k)}\mathbf{q}$, $\mathbf{f}_{\text{dir}}^{(k)}$ represents the forces exerted on the master system due to the direct field of subsystem k and $\mathbf{f}^{(k)}$ denotes the sum of the loads applied to subsystem k at its DOFs.

Introducing Eq. (2.5) leads to a reformulation of Eq. (2.1) as follows:

$$\mathbf{D}_{\text{tot}}\mathbf{q} = \mathbf{f}_{\text{tot}}, \tag{2.6}$$

where $\mathbf{D}_{\text{tot}} := \mathbf{D}_{\text{d}} + \sum_{k=1}^{N_{\text{s}}} \mathbf{D}_{\text{dir}}^{(k)}$ is a purely deterministic matrix, and $\mathbf{f}_{\text{tot}} = \mathbf{f} + \sum_{k=1}^{N_{\text{s}}} \mathbf{f}_{\text{rev}}^{(k)}$.

2.2.2 The direct field reciprocity relationship

When rewriting the equations of motion in cross spectral format and averaging over an ensemble of random boundaries of the statistical subsystems, Eq. (2.6) becomes:

$$\text{E}[\mathbf{q}\mathbf{q}^{\text{H}}] = \mathbf{D}_{\text{tot}}^{-1}\text{E}[\mathbf{f}_{\text{tot}}\mathbf{f}_{\text{tot}}^{\text{H}}]\mathbf{D}_{\text{tot}}^{-\text{H}}, \tag{2.7}$$

with $\square^{\text{H}}$ the Hermitian of matrix $\square$ and with

$$\text{E}[\mathbf{f}_{\text{tot}}\mathbf{f}_{\text{tot}}^{\text{H}}] = \mathbf{f}\ \mathbf{f}^{\text{H}} + \sum_{k} \left(\mathbf{f}\ \text{E}[\mathbf{f}_{\text{rev}}^{(k)}] + \text{E}[\mathbf{f}_{\text{rev}}^{(k)}]\ \mathbf{f}^{\text{H}}\right) + \sum_{k,t} \text{E}[\mathbf{f}_{\text{rev}}^{(k)}\ \mathbf{f}_{\text{rev}}^{(t),\text{H}}]. \tag{2.8}$$

It can be noticed that the randomness of the master system response $\mathbf{q}$ resides solely in the random blocked reverberant forces. Given that the properties of the random boundary are unknown, the wave scattering at the random boundary is modelled statistically in a maximum entropy sense, i.e., the uncertainty induced by the wave scattering is maximized. Minimizing the information about the random boundary, Eq. (2.8) tends to the following [102, 103]:

$$\text{E}[\mathbf{f}_{\text{rev}}^{(k)}] = 0, \tag{2.9}$$

$$\text{E}[\mathbf{f}_{\text{tot}}\mathbf{f}_{\text{tot}}^{\text{H}}] = \mathbf{f}\ \mathbf{f}^{\text{H}} + \sum_{k} \text{E}[\mathbf{f}_{\text{rev}}^{(k)}\ \mathbf{f}_{\text{rev}}^{(k),\text{H}}], \tag{2.10}$$

with

$$\text{E}[\mathbf{f}_{\text{rev}}^{(k)}\mathbf{f}_{\text{rev}}^{(k),\text{H}}] = \frac{4\text{E}[E_k]}{\omega\pi n_k}\text{Im}\{\mathbf{D}_{\text{dir}}^{(k)}\}, \tag{2.11}$$

where E_k and n_k denote respectively the total energy and the modal density of the kth subsystem. Eq. (2.11) relates the blocked reverberant forces with the direct field response and is also known as the 'diffuse field reciprocity relationship': the random boundary is a diffusely reflecting boundary in the statistical sense.

Inserting equations (2.10) and (2.11) into equation (2.7), gives:

$$\mathrm{E}[\mathbf{q}\mathbf{q}^{\mathrm{H}}] = \mathbf{D}_{\mathrm{tot}}^{-1}\big(\mathbf{f}\ \mathbf{f}^{\mathrm{H}}\big)\mathbf{D}_{\mathrm{tot}}^{-\mathrm{H}} + \underbrace{\mathbf{D}_{\mathrm{tot}}^{-1}\Bigg(\sum_{k}\frac{4\mathrm{E}[E_k]}{\omega\pi n_k}\mathrm{Im}\{\mathbf{D}_{\mathrm{dir}}^{(k)}\}\Bigg)\mathbf{D}_{\mathrm{tot}}^{-\mathrm{H}}}_{\mathrm{E}[\mathbf{q}_{\mathrm{rev}}\mathbf{q}_{\mathrm{rev}}^{\mathrm{H}}]}, \tag{2.12}$$

in which the second term $\mathrm{E}[\mathbf{q}_{\mathrm{rev}}\mathbf{q}_{\mathrm{rev}}^{\mathrm{H}}]$ describes the DOFs of the master system, associated with the stochastically determined blocked reverberant forces in the subsystems. This equation will now be used in the next section when assembling the power flows in the overall system, and allows to obtain the mean total energies of the multiple subsystems in the hybrid framework.

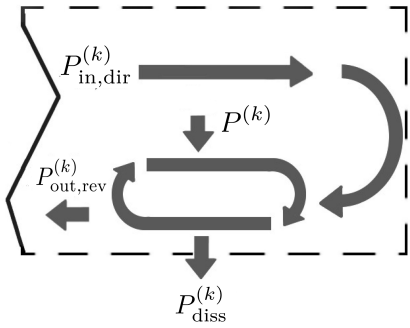

Figure 2.6: Illustration of the ensemble energy flows within a stochastic subsystem (adapted from [103]). Solid lines and dashed lines represent respectively deterministic and random boundaries.

2.3 Conservation of energy

Figure 2.6 shows the energy flows in statistical subsystem k. For each subsystem k, conservation of energy implies that:

$$P^{(k)}_{\mathrm{diss}} + P^{(k)}_{\mathrm{out,rev}} = P^{(k)}_{\mathrm{in,dir}} + P^{(k)}, \qquad k = 1, \ldots, N_{\mathrm{s}} \tag{2.13}$$

with $P^{(k)}_{\mathrm{in,dir}}$ the power injected into the direct field at the deterministic junctions, $P^{(k)}$ the power directly inserted into the reverberant field of the subsystem, $P^{(k)}_{\mathrm{diss}}$ the power dissipated within the reverberant field and $P^{(k)}_{\mathrm{out,rev}}$ the power leaving the reverberant field of the subsystem. Note that power injected into the subsystem acts on the direct field (before reflections), while power that leaves

the subsystem, flows from the reverberant field (after reflections). Although every input power is associated with a direct field, the current formulation allows to include a known power $P^{(k)}$ of an excitation source at a location remote from other interfaces. The powers defined above denote values averaged over time. However, for notational convenience $< P >_{\mathrm{t}}$ is indicated by P.

In the remainder of this section, the described power flows are elaborated in §2.3.1. The assembling of the power balances of the multiple subsystems is done in §2.3.2.

2.3.1 Expressions for the power flows

First, the dissipated power P_{diss} is determined. A damping loss factor η_k of the subsystem k is defined, so that the power dissipated within the kth reverberant field is:

$$P_{\mathrm{diss}}^{(k)} = \omega \eta_k E_k. \tag{2.14}$$

Secondly, an expression for $P_{\mathrm{in,dir}}^{(k)}$ is derived, starting from the general definition for the time-averaged power in generalized coordinates. The power is injected into the direct field of subsystem k by the structural vibrations at the deterministic junctions, described by the generalized coordinates $\mathbf{q}$ and corresponding load vector $\mathbf{f}_{\mathrm{dir}}^{(k)}$. Note that these forces do not include the forces due to the reverberant field. $P_{\mathrm{in,dir}}^{(k)}$ is then defined by:

$$P_{\mathrm{in,dir}}^{(k)} = -\frac{\omega}{2}\mathrm{Im}\{\mathbf{q}^{\mathrm{H}}\mathbf{f}_{\mathrm{dir}}\} \tag{2.15}$$

$$= \frac{\omega}{2}\mathrm{Im}\{\mathbf{q}^{\mathrm{H}}\mathbf{D}_{\mathrm{dir}}\mathbf{q}\} \tag{2.16}$$

$$= \frac{\omega}{2}\sum_{s,t}\mathrm{Im}\{q_s^* D_{\mathrm{dir},st}^{(k)} q_t\} \tag{2.17}$$

$$= \frac{\omega}{2}\sum_{s,t}\mathrm{Im}\{D_{\mathrm{dir},st}^{(k)}\}[q_s^* q_t], \tag{2.18}$$

where $\square^*$ denotes the complex conjugate of $\square$. Inserting Eq. (2.12) in Eq. (2.18) results in the ensemble averaged input power:

$$\mathrm{E}[P_{\mathrm{in,dir}}^{(k)}] = P_{\mathrm{in,ext}}^{(k)} + \sum_j \mathrm{E}[P_{\mathrm{in},jk}], \tag{2.19}$$

with

$$P_{\text{in,ext}}^{(k)} = \frac{\omega}{2} \sum_{s,t} \text{Im}\{D_{\text{dir},st}^{(k)}\} \left(\mathbf{D}_{\text{tot}}^{-1} (\mathbf{f} \ \mathbf{f}^{\text{H}}) \mathbf{D}_{\text{tot}}^{-\text{H}} \right)_{st}, \tag{2.20}$$

and

$$\text{E}[P_{\text{in},jk}] = \frac{2\text{E}[E_j]}{\pi n_j} \sum_{s,t} \text{Im}\{D_{\text{dir},st}^{(k)}\} \left(\mathbf{D}_{\text{tot}}^{-1} \text{Im}\{\mathbf{D}_{\text{dir}}^{(j)}\} \mathbf{D}_{\text{tot}}^{-\text{H}} \right)_{st}. \tag{2.21}$$

Similarly, $P_{\text{out,rev}}^{(k)}$ can be determined via the general definition of the time-averaged power. As stated earlier, the power leaving the subsystem flows from the reverberant field, resulting in the following equation:

$$P_{\text{out,rev}}^{(k)} = -\frac{\omega}{2} \text{Im}\{\mathbf{q}_{\text{rev}}^{(k),\text{H}} \mathbf{f}_{\text{rev}}^{(k)}\} \tag{2.22}$$

$$= \frac{\omega}{2} \text{Im}\{\mathbf{q}_{\text{rev}}^{(k),\text{H}} \mathbf{D}_{\text{tot}} \mathbf{q}_{\text{rev}}^{(k)}\} \tag{2.23}$$

$$= \frac{\omega}{2} \sum_{s,t} \text{Im}\{q_{\text{rev},s}^{(k),*} D_{\text{tot},st} q_{\text{rev},t}^{(k)}\} \tag{2.24}$$

$$= \frac{\omega}{2} \sum_{s,t} \text{Im}\{D_{\text{tot},st}\} [q_{\text{rev},s}^{(k),*} q_{\text{rev},t}^{(k)}], \tag{2.25}$$

with $\mathbf{q}_{\text{rev}}^{(k)}$ the master system displacements associated with the blocked reverberant forces in the kth subsystem. Inserting equation (2.12) in Eq. (2.25) gives:

$$\text{E}[P_{\text{out,rev}}^{(k)}] = \frac{2\text{E}[E_k]}{\pi n_k} \sum_{s,t} \text{Im}\{D_{\text{tot},st}\} \left(\mathbf{D}_{\text{tot}}^{-1} \text{Im}\{\mathbf{D}_{\text{dir}}^{(k)}\} \mathbf{D}_{\text{tot}}^{-\text{H}} \right)_{st}. \tag{2.26}$$

Given that

$$\text{Im}\{D_{\text{tot},st}\} = \text{Im}\{D_{\text{d},st}\} + \sum_{j=1}^{N_{\text{s}}} \text{Im}\{D_{\text{dir},st}^{j}\}, \tag{2.27}$$

Eq. (2.26) is then:

$$\begin{aligned} \text{E}[P_{\text{out,rev}}^{(k)}] = & \frac{2\text{E}[E_k]}{\pi n_k} \sum_{s,t} \text{Im}\{D_{\text{d},st}\} \left(\mathbf{D}_{\text{tot}}^{-1} \text{Im}\{\mathbf{D}_{\text{dir}}^{(k)}\} \mathbf{D}_{\text{tot}}^{-\text{H}} \right)_{st} \\ & + \frac{2\text{E}[E_k]}{\pi n_k} \sum_{j} \left(\sum_{s,t} \text{Im}\{D_{\text{dir},st}^{(j)}\} \left(\mathbf{D}_{\text{tot}}^{-1} \text{Im}\{\mathbf{D}_{\text{dir}}^{(k)}\} \mathbf{D}_{\text{tot}}^{-\text{H}} \right)_{st} \right). \end{aligned} \tag{2.28}$$

2.3.2 Assembling the power balances of the subsystems

When substituting the ensemble averaged power flows determined in Eqs. (2.14), (2.19) and (2.28) into Eq. (2.13), N_s power balances are found, which can be solved for the N_s unknown mean total energies $\mathrm{E}[E_k]$:

$$\omega\Big(\eta_k+\mathrm{E}[\eta_{\mathrm{d},k}]\Big)\mathrm{E}[E_k]+\sum_{j=1}^{N_\mathrm{s}}\omega\mathrm{E}[\eta_{kj}]n_k\left(\frac{\mathrm{E}[E_k]}{n_k}-\frac{\mathrm{E}[E_j]}{n_j}\right)=P_{\mathrm{in,ext}}^{(k)}+P^{(k)},\ \ k=1,\ldots,N_\mathrm{s}, \tag{2.29}$$

where

$$\mathrm{E}[\eta_{\mathrm{d},k}]=\frac{2}{\omega\pi n_k}\sum_{s,t}\mathrm{Im}\{D_{\mathrm{d},st}\}\left(\mathbf{D}_\mathrm{tot}^{-1}\mathrm{Im}\{\mathbf{D}_\mathrm{dir}^{(k)}\}\mathbf{D}_\mathrm{tot}^{-\mathrm{H}}\right)_{st}, \tag{2.30}$$

$$\mathrm{E}[\eta_{kj}]=\frac{2}{\pi\omega n_k}\sum_{s,t}\mathrm{Im}\{D_{\mathrm{dir},st}^{(k)}\}\left(\mathbf{D}_\mathrm{tot}^{-1}\mathrm{Im}\{\mathbf{D}_\mathrm{dir}^{(j)}\}\mathbf{D}_\mathrm{tot}^{-\mathrm{H}}\right)_{st}. \tag{2.31}$$

It can be noted that the power balance equation (2.29) has formally the same structure as in conventional SEA. Therefore, the factors η_{kj} can be interpreted as coupling loss factors (CLFs), which describe the power transfer between subsystems k and j, and equation (2.31) provides a rigorous way to compute their ensemble mean, even when the overall system is partly deterministic. Note that the derivation of Eq. (2.29) makes use of the symmetry of the CLFs, such that $\eta_{kj}n_k=\eta_{jk}n_j$, as was proven in [103]. Alternatively, the CLFs could also be determined directly from equation (2.21), as [22]:

$$P_{\mathrm{in},jk}=\omega\eta_{jk}E_j.$$

In a similar manner, Eq. (2.30) enables to rigorously estimate the power that is lost by energy dissipation in the master system.

2.4 A hybrid framework for the acoustic performance of building elements

2.4.1 Airborne sound prediction

Sound transmission loss measurements take place in an acoustic laboratory like the one depicted in Fig. 2.7. The test sample is built in between two rooms, the source and receiver room. This overall room-wall-room system is called a transmission suite.

The Schroeder frequency of a specific laboratory is a good indicator to mark the transition between low and high frequency behaviour [99]. Below this frequency,

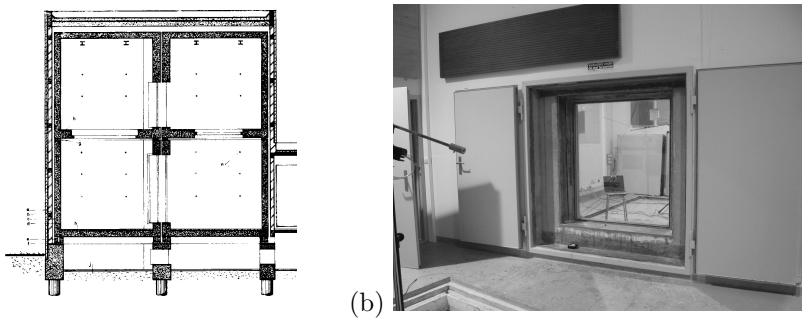

Figure 2.7: (a) A section of the KU Leuven Laboratory of Acoustics reveals four possible transmission openings [116]. A plexiglass panel is built into the smaller vertical transmission opening of the transmission suite in (b) [86].

the modal behaviour of the rooms results in strong oscillations in the STL data. Above this frequency, the sound field in the rooms can be approximated by a diffuse wave field with little uncertainty. The frequency is determined using the room volume and reverberation time. The Schroeder frequency of the four rooms in the KU Leuven Laboratory of Acoustics (cfr. Fig. 2.7) which have a volume of 87 m^3 and for which the reverberation time is taken to be 1.5 s, is equal to 263 Hz. Mind that besides STL differences caused by small variations of the test sample built in several lab environments or due to different dimensions of the building element, large deviations at lower frequencies between STL measurements for the same test sample are caused by differences between acoustic laboratories such as the volume or shape of the source and receiver room.

Ideally, the sound field in the rooms can be approximated by a diffuse wave field, in order to minimize the influence of the characteristics of the laboratory rooms on the STL of the test sample. When applying the hybrid framework on the room-wall-room system, the rooms are therefore modelled as SEA subsystems. Since the rooms are modelled stochastically, other statistical properties such as the variance of the sound transmission or radiated sound power, inherent to the assumption of diffuse sound fields in the rooms, can be assessed [86].

The wall is modelled deterministically, as to account for the modal behaviour that might influence the STL prediction.

So, the model of the room-wall-room system is decomposed into a deterministic model for the wall, and two SEA subsystems for the rooms. By solving for the mean coupling loss factor $E[\eta_{12}]$ between the two subsystems, the mean sound

transmission $\mathrm{E}[\tau_{12}]$ can be obtained from [26]

$$\mathrm{E}[\tau_{12}] = \mathrm{E}[\eta_{12}]\frac{4\omega V_1}{c_\mathrm{a} S}, \tag{2.32}$$

where S denotes the surface area of the wall, V_1 the volume of the source room, and c_a the speed of sound.

An important advantage of the general deterministic-SEA framework described above, is that not only the mean, but also the variance of the system's response can be computed. It was demonstrated by Langley and Cotoni [62] that the variance can be computed by a first-order perturbation analysis of the power balance in Eq. (2.29). Reynders et al. [86] then made the connection with the variance of the sound transmission σ_τ. It can be computed in closed form as follows:

$$\sigma_\tau^2 = \mathrm{Relcov}[C_{12}, C_{12}]\mathrm{E}[\tau_{12}]^2, \tag{2.33}$$

with $\mathrm{Relcov}[C_{12}, C_{12}]$ the relative covariance of the elements of the power balance matrix $\mathbf{C}_0$, as defined in [86]:

$$\begin{aligned}\mathrm{Relcov}[C_{12}, C_{12}] = \sum_k \left(\frac{1}{\pi m_k'}\right)\Bigg\{ &\frac{\mathrm{Tr}(\mathrm{Im}\{\mathbf{D}_\mathrm{dir}^{(k)}\}\mathbf{G}^{(2)})\mathrm{Tr}(\mathbf{H}_k\mathbf{G}^{(2)})}{\left(\mathrm{Tr}(\mathrm{Im}\{\mathbf{D}_\mathrm{dir}^{(1)}\}\mathbf{G}^{(2)})\right)^2} \\ &+ \frac{\mathrm{Tr}(\mathrm{Im}\{\mathbf{D}_\mathrm{dir}^{(k)}\}\mathbf{G}^{(2)}\mathbf{H}_k\mathbf{G}^{(2)})}{\left(\mathrm{Tr}(\mathrm{Im}\{\mathbf{D}_\mathrm{dir}^{(1)}\}\mathbf{G}^{(2)})\right)^2}\Bigg\} + \Bigg\{\frac{\mathrm{Tr}(\mathrm{Im}\{\mathbf{D}_\mathrm{dir}^{(1)}\}\mathbf{G}^{(2)}\mathrm{Im}\{\mathbf{D}_\mathrm{dir}^{(1)}\}\mathbf{G}^{(2)})}{\left(\mathrm{Tr}(\mathrm{Im}\{\mathbf{D}_\mathrm{dir}^{(1)}\}\mathbf{G}^{(2)})\right)^2}\Bigg\},\end{aligned} \tag{2.34}$$

where Tr is the trace matrix, and with

$$\mathbf{G}^{(2)} = \left(\frac{4}{\omega\pi}\right)\mathbf{D}_\mathrm{tot}^{-1}\mathrm{Im}\{\mathbf{D}_\mathrm{dir}^{(2)}\}\mathbf{D}_\mathrm{tot}^{-\mathrm{H}}, \tag{2.35}$$

$$\begin{aligned}\mathbf{H}_k =& 4\mathrm{Im}\{\mathbf{D}_\mathrm{dir}^{(1)}\}\mathbf{D}_\mathrm{tot}^{-1}\mathrm{Im}\{\mathbf{D}_\mathrm{dir}^{(k)}\}\mathbf{D}_\mathrm{tot}^{-\mathrm{H}}\mathrm{Im}\{\mathbf{D}_\mathrm{dir}^{(1)}\} + \mathrm{Im}\{\mathbf{D}_\mathrm{dir}^{(1)}\}\delta_{k1} \\ &- 2\delta_{k1}\mathrm{i}\mathrm{Im}\{\mathbf{D}_\mathrm{dir}^{(1)}\}\mathbf{D}_\mathrm{tot}^{-1}\mathrm{Im}\{\mathbf{D}_\mathrm{dir}^{(1)}\} + 2\delta_{k1}\mathrm{i}\mathrm{Im}\{\mathbf{D}_\mathrm{dir}^{(1)}\}\mathbf{D}_\mathrm{tot}^{-\mathrm{H}}\mathrm{Im}\{\mathbf{D}_\mathrm{dir}^{(1)}\}.\end{aligned} \tag{2.36}$$

δ_{k1} indicates the Kronecker delta. The effective modal overlap factor m_k', which appears in equation (2.34), is defined as [68]:

$$m_k' = \omega\eta_{\mathrm{a},k}n_{\mathrm{a},k}, \tag{2.37}$$

in which the damping loss factors $\eta_{\mathrm{a},k}$ and modal densities $n_{\mathrm{a},k}$ of the rooms can be estimated as [26, 117]:

$$\eta_{\mathrm{a},k} = \frac{4.4\pi}{\omega T_{\mathrm{a},k}} \qquad \text{and} \qquad n_{\mathrm{a},k} = \frac{\omega^2 V_k}{2\pi^2 c_\mathrm{a}^3}, \tag{2.38}$$

with $T_{\mathrm{a},k}$ the reverberation time of room k and V_k its volume. When the mean and variance of the sound transmission are known, the mean $\mathrm{E}[R]$ and variance σ_R of the sound transmission loss follow from

$$\mathrm{E}[R] = -10 \log \mathrm{E}[\tau_{12}], \tag{2.39}$$

and

$$\sigma_R^2 = \left(\frac{-10}{\ln(10)\mathrm{E}[\tau_{12}]} \right)^2 \sigma_\tau^2. \tag{2.40}$$

2.4.2 Structure borne sound prediction

In case of impact noise, power is injected directly into the structure due to structural loading, caused by a tapping machine in a standardized test or rain noise for instance. The radiated energy is then a measure of the structure borne sound insulation of the floor. Similarly as for airborne sound prediction, the receiver room is considered to be a stochastic subsystem, while the floor is treated deterministically.

The time-averaged power input into the underlying room at a certain frequency is determined as the sum of the input powers to the direct and reverberant fields [88]:

$$P_{\mathrm{in}} = P_{\mathrm{in,dir}} + P_{\mathrm{in,rev}}. \tag{2.41}$$

Elaborating the powers in generalized coordinates, results in:

$$P_{\mathrm{in}} = \frac{\omega}{2} \mathrm{Im}\{\mathbf{q}^{\mathrm{H}}(\mathbf{f}_{\mathrm{dir}} + \mathbf{f}_{\mathrm{rev}})\}. \tag{2.42}$$

When modelling the wave scattering due to the boundaries and objects in the room in a maximum entropy sense, the reverberant field becomes a diffuse wave field, which consists of plane waves coming from all directions, with equal amplitude and uncorrelated phase. From the central limit theorem [39, Sec. 5.5], it can be concluded that the complex phasor pressure amplitudes have zero mean, so that:

$$\mathrm{E}[\mathbf{f}_{\mathrm{rev}}] = \mathbf{0}. \tag{2.43}$$

Equation (2.42) now becomes:

$$\mathrm{E}[P_{\mathrm{in}}] = \frac{\omega}{2} \sum_{s,t} \mathrm{Im}\{D_{\mathrm{dir},st}\}[q_s^* q_t], \tag{2.44}$$

which is equivalent to equation (2.19). This is expected, as the input power acts solely on the direct field and not on the reverberant field. To obtain the

radiated power, the generalized coordinates $\mathbf{q}$ need to be determined first. This can be done via the equations of motion of the wall or floor system:

$$\mathbf{q} = \mathbf{D}_{\mathrm{d}}^{-1}\mathbf{f}, \tag{2.45}$$

in which $\mathbf{D}_{\mathrm{d}}$ is the deterministic dynamic stiffness matrix of the structure and $\mathbf{f}$ is the known external loading, due to the impact force. Fluid loading is not taken into account, but could be added if necessary. Mind that this can be significant at and around the coincidence frequency. By inserting the generalized coordinates $\mathbf{q}$ found in equation (2.45) into equation (2.44), the radiated power $\mathrm{E}[P_{\mathrm{in}}]$ can be computed.

To determine the variance of the sound power due to the diffuse field assumption of the receiver room, a modal representation of the sound field in the room is considered, in which the mode shapes are random as the wave scattering within the room is deemed to be random. When modelling this wave scattering in a maximum entropy sense, it is found that the statistics of the eigenvalues of the room are equivalent to the eigenvalues of a Gaussian Orthogonal Ensemble random matrix [76] and the mode shapes are independent Gaussian random fields [125]. This concept results in the derivation of the variance of the input power of a diffuse field under harmonic loading [62, 88]:

$$\sigma^2_{P_{\mathrm{in}}} \approx \left(\frac{1}{\pi m'} + \frac{1}{(\pi m')^2}\right) P^2_{\mathrm{in}}, \tag{2.46}$$

with m' the modal overlap factor of the room as defined in Eq. (2.37). The approximation in Eq. (2.46) is accurate when $m' \geqslant 0.2$.

Eq. (2.46) has been further extended to the band-averaged variance of the sound power [61, 88]:

$$\begin{aligned} < \sigma^2_{P_{\mathrm{in}}} >_f \approx \Bigg(& \frac{1}{\pi m' B_k^2}\big(2B_k \arctan(B_k) - \ln(1+B_k^2)\big) \\ & + \frac{1}{(\pi m' B_k)^2}\ln\big(1+B_k^2\big)\Bigg) < P_{\mathrm{in}} >_f^2, \end{aligned} \tag{2.47}$$

with

$$B_k = \frac{f_{\mathrm{u}} - f_{\mathrm{l}}}{f\eta_{\mathrm{a},k}}. \tag{2.48}$$

$< \square >_f$ refers to a band-averaged value. f, f_{u} and f_{l} represent respectively the centre frequency, upper limit frequency and lower limit frequency of the band. For 1/3-octave bands, $B_k \approx 0.23/\eta_{\mathrm{a},k}$, while for octave bands $B_k \approx 0.71/\eta_{\mathrm{a},k}$.

The sound power level $\mathrm{E}[L_{\mathrm{P}}]$ is computed using the found input power $\mathrm{E}[P_{\mathrm{in}}]$:

$$\mathrm{E}[L_{\mathrm{P}}] = 10\log\frac{\mathrm{E}[P_{\mathrm{in}}]}{P_0}, \quad \text{with} \quad P_0 = 10^{-12}\ \mathrm{W}, \tag{2.49}$$

with corresponding variance:

$$\sigma^2_{L_\mathrm{P}} = 10\log\left(\frac{10}{\ln(10)\mathrm{E}[P_\mathrm{in}]}\right)^2 \sigma^2_{P_\mathrm{in}}. \tag{2.50}$$

2.5 General expressions for the direct field and deterministic dynamic stiffness matrix

To solve for the sound transmission loss and/or the radiated power, a choice has to be made for the generalized coordinates and expressions for the deterministic dynamic stiffness matrix of the test sample and for the direct field dynamic stiffness matrix of the rooms are needed.

Section 2.5.1 discusses the choice of generalized coordinates. Next, a general expression for the deterministic dynamic stiffness matrix is given in § 2.5.2. Two general methods to obtain the direct field response are discussed in sections 2.5.3 and 2.5.4: section 2.5.3 handles the computation of the direct field response via an efficient spatial Fourier transform of the mode shapes, while § 2.5.4 proposes an alternative method which uses the displacement field of the mode in spatial coordinates.

2.5.1 Defining the generalized coordinates

When expressing the system of equations of the hybrid framework into generalized coordinates, the displacements of the wall or floor are decomposed using a set of basis functions with corresponding generalized coordinates. Consider $u(x, y, z)$ as the displacement field of the wall or floor, $\psi_j(x, y, z)$ as the jth basis function and q_j as the corresponding generalized coordinate, so that:

$$u(x, y, z) \approx \sum_j^{N_\mathrm{fun}} \psi_j(x, y, z) q_j. \tag{2.51}$$

The approximation in this equation is due to the truncation of the series, considering a finite set of N_fun basis functions. A possibility is working with local basis functions, e.g., FE basis functions in global coordinates. The coordinates are then nodal displacements. However, a well-chosen set of global basis functions can reduce the computational cost. This set of basis functions should be compatible with the considered boundary conditions.

If the harmonic motion of an infinite structure is considered, the basis functions can be a set of travelling waves $\boldsymbol{\psi}_\mathrm{wave}$ with corresponding coordinates $\mathbf{q}_\mathrm{wave}$.

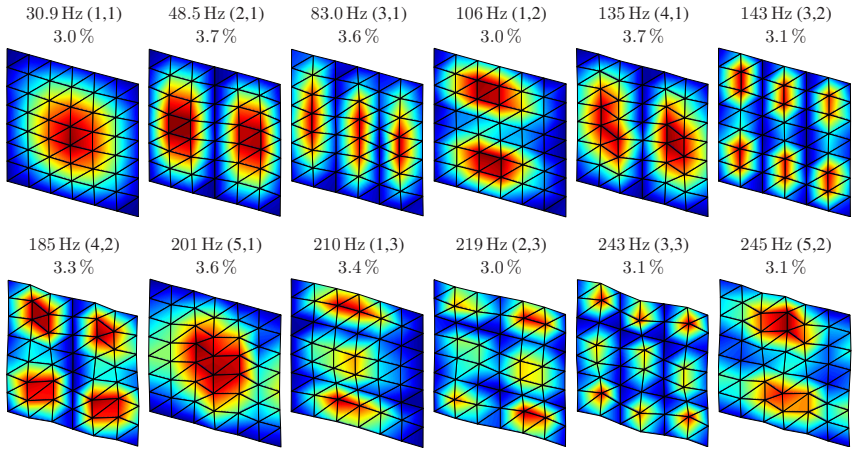

Figure 2.8: The first 12 identified mode shapes of a rib-stiffened panel with corresponding natural frequencies and damping ratios, found via an experimental modal analysis [87].

As a finite size correction, a spatial windowing technique could be used, which accounts for diffraction effects. In this case, the out-of-plane displacements outside the structure's dimensions are taken zero. For a finite structure with Neumann and/or Dirichlet boundary conditions, the displacements can be decomposed as in Eq. (2.51) using the mode shapes of the structure $\boldsymbol{\psi}_{\text{mod}}$. $\mathbf{q}_{\text{mod}}$ are termed the modal coordinates. FEM could for instance be used to compute the natural frequencies and the mode shapes for a structure with specific boundary conditions.

In the next two chapters, an assumption is made for the boundary conditions. It was discussed earlier in section 1.3 that there is a lot of uncertainty about boundary conditions of structures *in situ* and in a laboratory environment. For simplicity, simply supported boundary conditions are assumed. This makes sense for building elements, that are connected to other building elements at the edges [47]. Measurements on a rib-stiffened panel in the small transmission opening of the KU Leuven have also shown that the examined measured mode shapes suggest simply supported mode shapes (cfr. Fig. 2.8).

In case of a rectangular, thin plate with simply supported boundary conditions, the modal properties can be determined analytically. The displacement mode shapes are sinusoidal basis functions $\boldsymbol{\psi}_{\text{sin}}$ with corresponding coordinates $\mathbf{q}_{\text{sin}}$. For more complicated structures, other methods will be proposed in this work to approximate or compute the exact modal behaviour of the structure.

2.5.2 The deterministic dynamic stiffness matrix

A general expression for the deterministic dynamic stiffness matrix $\mathbf{D}_{\mathrm{d}}$ in terms of a discretized displacement field $\mathbf{u} \in \mathbb{C}^{N_{\mathrm{dof}} \times 1}$ is as follows:

$$\mathbf{D}_{\mathrm{d}}(\omega) = \Big((1+\mathrm{i}\eta)\mathbf{K} - \omega^2\mathbf{M}\Big), \tag{2.52}$$

with $\mathbf{M} \in \mathbb{C}^{N_{\mathrm{dof}} \times N_{\mathrm{dof}}}$ and $\mathbf{K} \in \mathbb{C}^{N_{\mathrm{dof}} \times N_{\mathrm{dof}}}$ respectively the mass and stiffness matrix of the structure. Damping is included by assuming frequency independent hysteretic damping with η the damping loss factor of the structure. The deterministic dynamic stiffness matrix can be converted into generalized coordinates by imposing the basis functions $\boldsymbol{\psi}_j \in \mathbb{C}^{N_{\mathrm{dof}} \times 1}$:

$$D_{\mathrm{d},hj}(\omega) = \boldsymbol{\psi}_h^{\mathrm{H}}\Big((1+\mathrm{i}\eta)\mathbf{K} - \omega^2\mathbf{M}\Big)\boldsymbol{\psi}_j, \tag{2.53}$$

In case of orthogonal basis functions e.g. the mode shapes of the structure, the deterministic dynamic stiffness matrix is a diagonal matrix:

$$D_{\mathrm{d},hj}(\omega) = \delta_{hj}\boldsymbol{\psi}_h^{\mathrm{H}}\Big((1+\mathrm{i}\eta)\mathbf{K} - \omega^2\mathbf{M}\Big)\boldsymbol{\psi}_j, \tag{2.54}$$

where δ_{hj} indicates the Kronecker delta. If the orthogonal basis functions are scaled as $\boldsymbol{\psi}_j^{\mathrm{H}}\mathbf{M}\boldsymbol{\psi}_j = m_j$, then Eq. (2.54) can be further simplified to:

$$D_{\mathrm{d},jj}(\omega) = m_j\Big((1+\mathrm{i}\eta)\Omega_j^2 - \omega^2\Big), \tag{2.55}$$

in which Ω_j denotes the eigenfrequency. Note that when the basis functions are mass normalized, m_j will be equal to one.

2.5.3 The direct field dynamic stiffness matrix via a formulation in the wavenumber domain

Motion of the air particles at the junction of room k and the structure is caused by normal displacements at the structure's surface in room k. When evaluating the direct field response in generalized coordinates, only the out-of-plane surface displacements of an imposed basis function j at the side of room k are therefore considered, which are indicated by $\psi_{\mathrm{n},j}^{(k)}$. The (h,j)-th element of the direct field dynamic stiffness matrix is then found via an integration of the multiplication of the surface pressure $p_h^{(k)}(\omega,x,y)$ $(z=0)$, due to the normal surface displacement field $\psi_{\mathrm{n},h}^{(k)}$ of basis function h, and the normal surface displacement field $\psi_{\mathrm{n},j}^{(k)}$ of basis function j:

$$D_{\mathrm{dir},hj}^{(k)}(\omega) = \int_{S_{\mathrm{s}}} p_h^{(k),*}(\omega,\mathbf{x})\psi_{\mathrm{n},j}^{(k)}(\mathbf{x})\mathrm{d}\mathbf{x}, \tag{2.56}$$

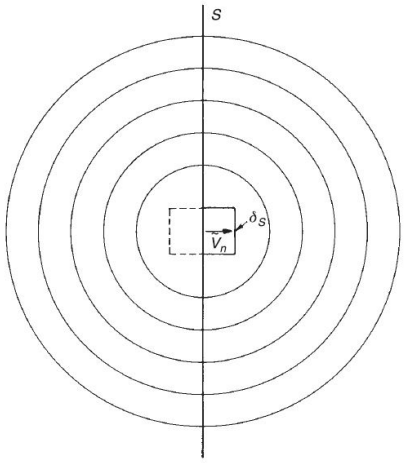

Figure 2.9: The free-field pressure field, due to a small baffled piston [41].

with S_s the surface area of the structure and $\mathbf{x} = (x, y)$ a location on the surface of the structure. The surface pressure at the point (x, y) is obtained using the Rayleigh integral [85]:

$$p_h^{(k)}(\omega, \mathbf{x}) = \int_{S_\mathrm{s}} \psi_{\mathrm{n},h}^{(k)}(\mathbf{x}') g(\omega, \mathbf{x} - \mathbf{x}') \mathrm{d}\mathbf{x}', \tag{2.57}$$

with $g(\omega, \mathbf{x} - \mathbf{x}')$ the acoustic Green's function which is the free-field pressure at location $\mathbf{x}$ resulting from a Dirac impulse displacement at location $\mathbf{x}'$, while there is a zero displacement at the other locations of the structure (cfr. Fig. 2.9):

$$g(\omega, \mathbf{r}) = \frac{\rho_\mathrm{a} \omega^2 \mathrm{e}^{-\mathrm{i}k_\mathrm{a}||\mathbf{r}||}}{2\pi||\mathbf{r}||}, \quad \mathbf{r} = (\mathbf{x} - \mathbf{x}'). \tag{2.58}$$

ρ_a and k_a are respectively the air density and the acoustic wavenumber. $||\square||$ indicates the modulus of a vector $\square$.

Inserting the Rayleigh integral into Eq. (2.56) results in:

$$D_{\mathrm{dir},hj}^{(k)}(\omega) = \int_{S_\mathrm{s}} \left[\int_{S_\mathrm{s}} \psi_{\mathrm{n},h}^{(k),*}(\mathbf{x}') g^*(\omega, \mathbf{x} - \mathbf{x}') \mathrm{d}\mathbf{x}' \right] \psi_{\mathrm{n},j}^{(k)}(\mathbf{x}) \mathrm{d}\mathbf{x}. \tag{2.59}$$

Transforming this expression to the wavenumber domain with the wavenumber vector $\mathbf{k} = (k_\mathrm{x}, k_\mathrm{y})$, results in a more efficient formulation for the direct field response as a quadruple integration over spatial coordinates is avoided. Defining

the inverse Fourier transformation of the Green's function as follows:

$$g(\omega, \mathbf{x} - \mathbf{x}') = \frac{1}{4\pi^2} \int_{-\infty}^{\infty} \tilde{g}(\omega, \mathbf{k}) \mathrm{e}^{-\mathrm{i}(\mathbf{k}(\mathbf{x}-\mathbf{x}'))} \mathrm{d}\mathbf{k}, \tag{2.60}$$

equation (2.59) becomes:

$$D^{(k)}_{\mathrm{dir,hj}}(\omega) = \frac{1}{4\pi^2} \int_{-\infty}^{\infty} \tilde{g}^*(\omega, \mathbf{k}) \left[\int_{S_\mathrm{s}} \psi^{(k),*}_{\mathrm{n},h}(\mathbf{x}') \mathrm{e}^{-\mathrm{i}\mathbf{k}\mathbf{x}'} \mathrm{d}\mathbf{x}' \right] \times \left[\int_{S_\mathrm{s}} \psi^{(k)}_{\mathrm{h},j}(\mathbf{x}) \mathrm{e}^{\mathrm{i}\mathbf{k}\mathbf{x}} \mathrm{d}\mathbf{x} \right] \mathrm{d}\mathbf{k}, \tag{2.61}$$

$$= \frac{1}{4\pi^2} \int_{-\infty}^{\infty} \tilde{g}^*(\omega, \mathbf{k}) \tilde{\psi}^{(k),*}_{\mathrm{n},h}(\mathbf{k}) \tilde{\psi}^{(k)}_{\mathrm{n},j}(\mathbf{k}) \mathrm{d}\mathbf{k}. \tag{2.62}$$

The tilde symbol indicates that the variable is defined in the wavenumber domain. In order to solve for the direct field response, an expression of the Green's function in the wavenumber domain is needed. A formulation for $\tilde{g}(\omega, \mathbf{k})$ is derived below.

The response in the free field at a location $(\mathbf{x}, z)$ to a displacement field $w(t, \mathbf{x})$, imposed on an infinite plate can be computed as follows:

$$p(t, \mathbf{x}, z) = \int_{-\infty}^{t} \left[\int_{-\infty}^{\infty} w(t', \mathbf{x}') g(t - t', \mathbf{r}, z) \mathrm{d}\mathbf{x}' \right] \mathrm{d}t'. \tag{2.63}$$

If the imposed displacement field is a travelling wave with unit amplitude, then

$$p(t, \mathbf{x}, z) = \mathrm{Re}\left\{ \int_{-\infty}^{t} \left[\int_{-\infty}^{\infty} \mathrm{e}^{\mathrm{i}(\omega t' - \mathbf{k}\mathbf{x}')} g(t - t', \mathbf{r}, z) \mathrm{d}\mathbf{x}' \right] \mathrm{d}t' \right\}, \tag{2.64}$$

$$= \mathrm{Re}\left\{ \mathrm{e}^{\mathrm{i}(\omega t - \mathbf{k}\mathbf{x})} \int_{-\infty}^{t} \mathrm{e}^{-\mathrm{i}\omega(t-t')} \tilde{g}(t - t', \mathbf{k}, z) \mathrm{d}t' \right\}, \tag{2.65}$$

$$= \mathrm{Re}\left\{ \mathrm{e}^{\mathrm{i}(\omega t - \mathbf{k}\mathbf{x})} \tilde{g}(\omega, \mathbf{k}, z) \right\}. \tag{2.66}$$

So, in order to obtain the acoustic Green's function in the wavenumber domain, one could impose a travelling wave with displacement field $w(\mathbf{x}, t) = \mathrm{Re}\left\{ \mathrm{e}^{\mathrm{i}(\omega t - \mathbf{k}\mathbf{x})} \right\}$ and compute the resulting pressure field. This pressure field will have the same frequency ω and wavenumbers $\mathbf{k} = (k_\mathrm{x}, k_\mathrm{y})$ as the imposed travelling wave, so that:

$$p(t, \mathbf{x}, z) = \mathrm{Re}\left\{ p_0 \mathrm{e}^{\mathrm{i}(\omega t - \mathbf{k}\mathbf{x} - k_z z)} \right\}, \tag{2.67}$$

with p_0 the unknown amplitude of the pressure field and with k_z the z-component of the wavenumber. Solving the Helmholtz equation:

$$\triangle^2 p + k_\mathrm{a}^2 p = 0, \tag{2.68}$$

results in:

$$\begin{cases} k_\mathrm{z} = \sqrt{k_\mathrm{a}^2 - ||\mathbf{k}||^2} & \text{if} \quad ||\mathbf{k}|| \leqslant k_\mathrm{a} \\ k_\mathrm{z} = -\mathrm{i}\sqrt{||\mathbf{k}||^2 - k_\mathrm{a}^2} & \text{if} \quad ||\mathbf{k}|| > k_\mathrm{a} \end{cases} \tag{2.69}$$

Note that the definition of k_z corresponds to an evanescent wave in the z-direction below coincidence ($||\mathbf{k}|| > k_\mathrm{a}$) and a propagating wave in the z-direction above coincidence ($||\mathbf{k}|| \leqslant k_\mathrm{a}$).

However, the unknown amplitude p_0 has yet to be determined. The travelling wave induces the same displacement field $w(t, \mathbf{x}, z = 0) = \mathrm{Re}\big(\mathrm{e}^{\mathrm{i}(\omega t - \mathbf{kx})}\big)$ on the air particles close to the surface. Using the continuity of the displacement field and the dynamic equilibrium of an elementary air volume, allows to obtain the unknown pressure amplitude p_0:

$$-\left.\frac{\partial p(t, \mathbf{x}, z)}{\partial z}\right|_{z=0} = \rho_\mathrm{a} \frac{\partial^2 w(t, \mathbf{x}, z = 0)}{\partial t^2}. \tag{2.70}$$

The unknown pressure becomes:

$$p_0 = \frac{\mathrm{i}\omega^2 \rho_\mathrm{a}}{k_\mathrm{z}}. \tag{2.71}$$

Inserting the found pressure into equation (2.67), results in the pressure field, caused by the travelling wave, imposed on an infinite plate:

$$p(t, \mathbf{x}, z) = \mathrm{Re}\big\{\mathrm{e}^{\mathrm{i}(\omega t - \mathbf{kx})} \tilde{g}(\omega, \mathbf{k}, z)\big\}, \tag{2.72}$$

$$\text{with} \quad \tilde{g}(\omega, \mathbf{k}, z) = \frac{\mathrm{i}\omega^2 \rho_\mathrm{a}}{k_\mathrm{z}} \mathrm{e}^{-\mathrm{i}k_\mathrm{z} z}, \tag{2.73}$$

and with k_z found from $\mathbf{k} = (k_\mathrm{x}, k_\mathrm{y})$ and the acoustic wavenumber k_a as in Eq. (2.69). The Green's function in Eq. (2.62) is found as $\tilde{g}(\omega, \mathbf{k}) = \tilde{g}(\omega, \mathbf{k}, z = 0)$.

A singularity appears for the Green's function in case of $k_\mathrm{a} = ||\mathbf{k}||$. The Green's function can be approximated to circumvent the singularity problem [126]. After the wavenumber domain is discretized into grid points $\mathbf{k}_0 = (k_{\mathrm{x}0}, k_{\mathrm{y}0})$ with equal grid spacing $\triangle k$ in both directions (cfr. Fig. 2.10(a)), the piece-wise constant Green's function $\tilde{g}'(\omega, \mathbf{k})$ is obtained by averaging the Green's function over a small segment with area $(\triangle k)^2$ (cfr. Fig. 2.10(b)):

$$\tilde{g}'(\omega, \mathbf{k}) = \frac{1}{(\triangle k)^2} \int_{(\triangle k)^2} \tilde{g}(\omega, \mathbf{k}) \mathrm{d}\mathbf{k} \tag{2.74}$$

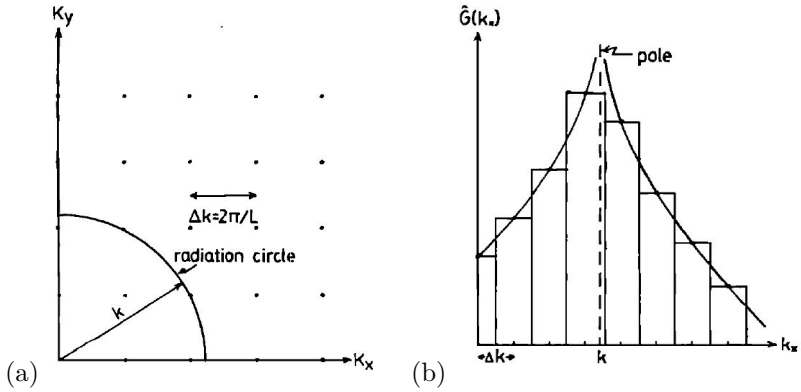

Figure 2.10: Illustration of the piece-wise constant Green's function, which is spatially averaged as shown in (b), according to the discretized wavenumber domain in (a) [126].

The integral is formulated in terms of polar coordinates with k_r and θ respectively the radial wavenumber and angular coordinate, so that the Green's function is averaged over a pie segment, approximating the square area $(\triangle k)^2$:

$$\tilde{g}'(\omega, \mathbf{k}) \approx \frac{1}{S} \int_{\theta_1}^{\theta_2} \int_{k_1}^{k_2} \frac{\mathrm{i}\omega^2 \rho_\mathrm{a}}{\sqrt{k_\mathrm{a}^2 - k_\mathrm{r}^2}} k_\mathrm{r} \mathrm{d}k_\mathrm{r} \mathrm{d}\theta. \tag{2.75}$$

For the considered surface area S around a grid point $\mathbf{k}_0$ the integral limits for k_r are fixed to $k_1 = ||\mathbf{k}_0|| - \triangle k/2$ and $k_2 = ||\mathbf{k}_0|| + \triangle k/2$, while the integral limits of θ are θ_1 and $\theta_2 = \theta_1 + \triangle\theta$. The area S is then approximately $||\mathbf{k}_0|| \triangle\theta \triangle k$, so that:

$$\tilde{g}'(\omega, \mathbf{k}) \approx \frac{\mathrm{i}\omega^2 \rho_\mathrm{a}}{||\mathbf{k}_0|| \triangle k} \int_{k_1}^{k_2} \frac{k_\mathrm{r}}{\sqrt{k_\mathrm{a}^2 - k_\mathrm{r}^2}} \mathrm{d}k_\mathrm{r}, \tag{2.76}$$

$$\approx \frac{\mathrm{i}\omega^2 \rho_\mathrm{a}}{||\mathbf{k}_0|| \triangle k} \left(\sqrt{k_\mathrm{a}^2 - k_1^2} - \sqrt{k_\mathrm{a}^2 - k_2^2} \right). \tag{2.77}$$

2.5.4 The direct field dynamic stiffness matrix via the wavelet approach

In order to evaluate the direct field response of equation (2.62) for an arbitrary displacement field $\psi_{\mathrm{n},j}^{(k)}(x, y)$, the interface between the room and the wall can be covered by a grid of points $\mathbf{x}_m = (x_m, y_m)$ $(h = 1, \ldots, N)$ with equal grid

spacing in both directions. The displacement fields $\psi_{\mathrm{n},j}^{(k)}$ are then approximated using a set of generalized degrees of freedom $a_m^{(k)}$ and shape functions $\varphi_m(x,y) = \varphi(x - x_m, y - y_m)$:

$$\psi_{\mathrm{n},j}^{(k)}(x,y) \approx \sum_{m=1}^{N} a_m^{(k)} \varphi(\mathbf{r}_m), \quad \text{with } \mathbf{r}_m = (x - x_m, y - y_m). \tag{2.78}$$

In the wavelet approach [59], the shape functions $\varphi(\mathbf{r}_m)$ are chosen to be jinc functions, $\mathrm{jinc}(x) = \mathrm{J}_1(x)/x$ with $\mathrm{J}_1(x)$ the Bessel function of the first kind and order 1, so that:

$$\varphi_{\mathrm{jinc}}(\mathbf{r}_m) = \frac{2\mathrm{J}_1\left(\frac{\sqrt{2}\pi}{\triangle x}||\mathbf{r}_m||\right)}{\left(\frac{\sqrt{2}\pi}{\triangle x}||\mathbf{r}_m||\right)}, \tag{2.79}$$

with $\triangle x$ the grid spacing in both directions. The corresponding generalized coordinates are denoted as $a_{\mathrm{jinc},h}^{(k)}$.

The decomposition of Eq. (2.78), based on the jinc basis functions given in Eq. (2.79), is then inserted into the general equation for the direct field response (cfr. Eq. (2.62)). The double integral reduces into a one-dimensional integral, using the radially symmetric lay out of the Bessel function and the Green's function. Further elaboration yields the following formula for the direct field response [59]:

$$D_{\mathrm{dir},hj}^{(k)}(\omega) = \mathbf{a}_{\mathrm{jinc},h}^{(k),\mathrm{H}} \mathbf{D}_{\mathrm{jinc}}(\omega) \mathbf{a}_{\mathrm{jinc},j}^{(k)}, \tag{2.80}$$

with

$$[\mathbf{a}_{\mathrm{jinc},j}^{(k)}]_m = \frac{\pi}{2} \boldsymbol{\psi}_{\mathrm{n},j}^{(k)}(x_m, y_m); \qquad [\mathbf{a}_{\mathrm{jinc},h}^{(k)}]_m = \frac{\pi}{2} \boldsymbol{\psi}_{\mathrm{n},h}^{(k)}(x_m, y_m). \tag{2.81}$$

The (s,t)-th element of the acoustic dynamic stiffness matrix $\mathbf{D}_{\mathrm{jinc}}$ is determined as follows:

$$D_{\mathrm{jinc},st} = D_{\mathrm{jinc}}(\mathbf{r}_{st}, \omega) = \frac{\mathrm{i}8\pi\omega\rho_a c_a k_a^2}{k_s^4} \Big(\mathrm{sinc}(k_a||\mathbf{r}_{st}||) + \mathrm{i}g(k_a||\mathbf{r}_{st}||)\Big), \tag{2.82}$$

$$\text{in which} \quad g(z) \approx \frac{\cos z - 1}{z} + \frac{2}{z} \sum_{k=1}^{\infty} \mathrm{J}_{2k+1}(z k_s/k_a), \tag{2.83}$$

$$\text{and} \quad \mathbf{r}_{st} = (x_s - x_t, y_s - y_t). \tag{2.84}$$

2.6 Conclusions

In this chapter, the hybrid framework was discussed. A different modelling strategy is preferred for the test sample and the rooms of the transmission

suite in the frequency range of interest, as modal behaviour of the wall might influence the sound transmission loss while the rooms exhibit high frequency behaviour. The transmission suite is therefore decomposed into two statistical room models and a deterministic wall or floor model which allows to account for finite size effects. A diffuse wave field is assumed, when modelling the rooms as SEA subsystems. A more traditional way to model the rooms as diffuse, is to integrate the oblique sound transmission over all possible angles of incidence. When comparing the hybrid method with the traditional integration over all angles of incidence, it is emphasized that not only the mean but also the variance, inherent to the diffuse field assumption, can be determined since the rooms are modelled statistically in the hybrid framework. Next, it was shown how the sound transmission loss and the radiated sound power level due to structural loading can be obtained in this framework. Note that the sound transmission loss is deduced from the coupling loss factor. Afterwards, the choice of general coordinates was investigated. To account for modal behaviour, a modal decomposition is performed. The displacements of the wall or floor are approximated by their decomposition on a finite set of modes or similar basis functions. Finally, in order to solve for the sound transmission loss and sound power level, the deterministic dynamic stiffness matrix of the wall or floor and the direct field dynamic stiffness matrix of the rooms need to be determined. General expressions were given in this chapter. For the direct field dynamic stiffness matrix, two possible methods were investigated. The first method makes use of an efficient Fourier transform, converting the quadruple integration in space into a double integration over the wavenumber domain. A piece-wise constant Green's function is used to avoid singularity around coincidence. Spatial windowing is implicitly applied as the out-of-plane displacements are taken to be zero outside the dimensions of the wall or floor when transforming the displacements into the wavenumber domain. Secondly, a wavelet approach was considered. By decomposing the displacement field into jinc functions, the direct field response was further elaborated, allowing to compute the direct field response using the displacement field of the basis function in spatial coordinates.

Chapter 3

Layered building elements

3.1 Introduction

Multilayered systems such as floors with a floating screed, decoupled hollow brick walls, laminated glazing etc. are nowadays crucial for noise control in buildings (cfr. Fig. 3.1). The transfer matrix method (TMM) is an analytical method capturing the dynamic behaviour of multilayered systems, composed of a stack of solid, poro-elastic or fluid layers [3, 35, 43]. The TMM is a useful and efficient tool to compute the acoustic performance of such systems.

(a)  (b) 

Figure 3.1: Examples of multilayered building elements: (a) A decoupled anchorless hollow brick wall [43]; (b) a floor with floating screed [43].

Being a wave-based approach, the vibro-acoustic behaviour of the multilayered system caused by plane wave excitation is considered. Plane wave propagation is expressed in terms of the transfer matrices for the various infinite layers, while the interaction between layers is described by interface matrices. In conventional

TMM, the layers are assumed to be of infinite extent. Consequently, conventional TMM is more appropriate for high frequencies, at which finite size effects are not important any more. Finite lateral dimensions can be approximately accounted for using a spatial windowing technique or an approximate modal TMM.

In this chapter, a general description of the conventional TMM for the prediction of airborne and impact noise is described in section 3.2. Generalizations that include finite-size effects are elaborated in section 3.3. After describing the methodology and the possible finite size corrections, it will be shown in section 3.4 how the hybridization between an approximate modal TMM (mTMM) and SEA can be achieved. Next, verification examples for the STL prediction are given in section 3.5. Impact noise, caused by a harmonic point force, is discussed briefly as well. Finally, the conclusions of this chapter are summarized in section 3.6.

3.2 General description of the conventional Transfer Matrix Method

3.2.1 Assembling the system of equations

Figure 3.2 shows a multilayered structure, consisting of n isotropic layers of infinite lateral dimensions, reducing the complexity to a two-dimensional problem. Three types of layers are defined: a poro-elastic layer, a solid layer or a fluid layer. Depending on the type of layer, variables are defined to describe the dynamic behaviour within a particular layer. These variables are expressed in terms of frequency f or, equivalently, the angular frequency ω and a trace wavenumber k_{tr}. The trace wavenumber k_{tr} equals the x-component of the wavenumber of the various waves that are travelling through the system. In case of oblique sound transmission with angle of incidence θ, the trace wavenumber follows from: $k_{\mathrm{tr}} = k_{\mathrm{a}} \sin\theta$. Mind that the z-component of the wavenumber k_{z} in air is found via Eq. (2.69).

Transfer Matrices

In order to describe sound propagation across a layer j, a transfer matrix $\mathbf{T}^{(j)}(\omega, k_{\mathrm{tr}})$ is defined so that:

$$\mathbf{m}_{\mathrm{M}_{2j-1}} = \mathbf{T}^{(j)}(\omega, k_{\mathrm{tr}})\mathbf{m}_{\mathrm{M}_{2j}}, \tag{3.1}$$

where the vector $\mathbf{m}_{\mathrm{M}}$ collects the variables, describing the acoustic field in a layer at point M in the system (cfr. Fig. 3.2).

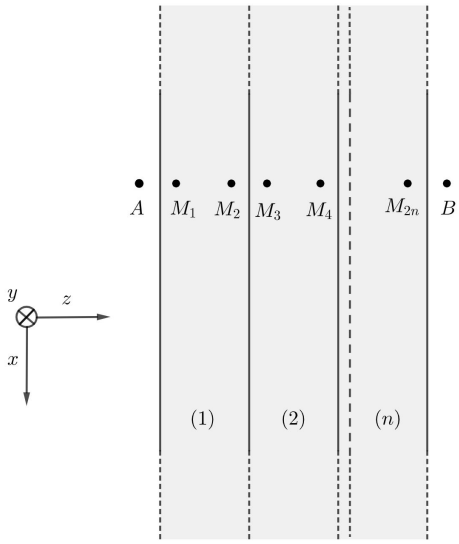

Figure 3.2: A multilayered system, consisting of n infinite, homogeneous layers (Adapted figure from [43]). A and B indicate points in the adjacent acoustic half spaces at the left and right of the system . The points M_{2j-1} and M_{2j} denote the left and right side within a layer j.

In case of a fluid (f) layer, only a longitudinal wave can propagate through the layer. The sound propagation within a fluid layer is then described in each point M by $\mathbf{m}^{\mathrm{f}}_{\mathrm{M}} = [p_{\mathrm{M}}\ v^{\mathrm{f}}_{\mathrm{z,M}}]^{\mathrm{T}}$, where p_{M} and $v^{\mathrm{f}}_{\mathrm{z,M}}$ indicate respectively the acoustic pressure and the z-component of the velocity of the fluid and T is the transpose. The transfer matrix $\mathbf{T}^{\mathrm{f},(j)}(k_{\mathrm{tr}}, \omega) \in \mathbb{C}^{2\times 2}$ relates the pressure and velocity at the right- and left-hand side of the fluid layer, as follows [3]:

$$\mathbf{m}^{\mathrm{f}}_{\mathrm{M}_{2j-1}} = \mathbf{T}^{\mathrm{f},(j)}(\omega, k_{\mathrm{tr}})\mathbf{m}^{\mathrm{f}}_{\mathrm{M}_{2j}}, \tag{3.2}$$

with

$$\mathbf{T}^{\mathrm{f},(j)}(\omega, k_{\mathrm{tr}}) = \begin{bmatrix} \cos(k^{\mathrm{f}}_{\mathrm{z}} t_{\mathrm{f}}) & \frac{\mathrm{i}\omega\rho_{\mathrm{f}}}{k^{\mathrm{f}}_{\mathrm{z}}} \sin(k^{\mathrm{f}}_{\mathrm{z}} t_{\mathrm{f}}) \\ \frac{\mathrm{i}k^{\mathrm{f}}_{\mathrm{z}}}{\omega\rho_{\mathrm{f}}} \sin(k^{\mathrm{f}}_{\mathrm{z}} t_{\mathrm{f}}) & \cos(k^{\mathrm{f}}_{\mathrm{z}} t_{\mathrm{f}}) \end{bmatrix}, \tag{3.3}$$

and

$$\begin{cases} k^{\mathrm{f}}_{\mathrm{z}} = \sqrt{k^2_{\mathrm{f}} - k^2_{\mathrm{tr}}} & \text{if} \quad k_{\mathrm{tr}} \leqslant k_{\mathrm{f}} \\ k^{\mathrm{f}}_{\mathrm{z}} = -\mathrm{i}\sqrt{k^2_{\mathrm{tr}} - k^2_{\mathrm{f}}} & \text{if} \quad k_{\mathrm{tr}} > k_{\mathrm{f}} \end{cases}, \tag{3.4}$$

where

$$k_{\mathrm{f}} = \omega/c_{\mathrm{f}}, \quad c_{\mathrm{f}} = K_{\mathrm{f}}/\rho_{\mathrm{f}}. \tag{3.5}$$

ρ_f, t_f and K_f are respectively the density in the fluid, the thickness of the fluid layer and the Bulk modulus of the fluid.

Both a longitudinal and a shear wave can travel through a solid (s) layer, resulting in four variables needed to characterize the acoustic field: $\mathbf{m}_\mathrm{M}^\mathrm{s} = [v_\mathrm{x,M}^\mathrm{s}\ v_\mathrm{z,M}^\mathrm{s}\ \sigma_\mathrm{zz,M}^\mathrm{s}\ \sigma_\mathrm{xz,M}^\mathrm{s}]^\mathrm{T}$. An explicit expression for the corresponding transfer matrix $\mathbf{T}^{\mathrm{s},(j)}(\omega, k_\mathrm{tr}) \in \mathbb{C}^{4\times4}$ can be found in [42]. To compute the transfer matrix of a solid layer with thickness t_s, the following material properties are needed: the Young's modulus E_s, the Poisson's ratio ν_s, the density ρ_s. The shear modulus G_s can be computed as follows:

$$G_\mathrm{s} = \frac{E_\mathrm{s}}{2(1+\nu_\mathrm{s})}. \tag{3.6}$$

Damping of the solid layer can be included via a complex Young's modulus $\underline{E} = E(1+\mathrm{i}\eta_\mathrm{s})$ with damping loss factor η_s.

A poro-elastic (p) layer with thickness t_p can be simplified as an equivalent fluid layer with complex and frequency-dependent material properties. When using this equivalent fluid model, it is assumed that the frame is motionless and that only a compressional wave will travel through the layer. Eq. (3.2) is then generalized into [117]:

$$\mathbf{m}_\mathrm{M_{2j-1}}^\mathrm{p} = \mathbf{T}^{\mathrm{p},(j)}(\omega, k_\mathrm{tr})\mathbf{m}_\mathrm{M_{2}}^\mathrm{p}, \qquad \mathbf{m}_\mathrm{M}^\mathrm{p} = [p_\mathrm{M}\ v_\mathrm{z,M}^\mathrm{p}]^\mathrm{T}, \tag{3.7}$$

with

$$\mathbf{T}^{\mathrm{p},(j)}(\omega, k_\mathrm{tr}) = \begin{bmatrix} \cosh(\frac{\Gamma_\mathrm{p} t_\mathrm{p} k_\mathrm{z}^\mathrm{p}}{k_\mathrm{p}}) & \frac{Z_\mathrm{c,p} k_\mathrm{p}}{k_\mathrm{z}^\mathrm{p}} \sinh(\frac{\Gamma_\mathrm{p} t_\mathrm{p} k_\mathrm{z}^\mathrm{p}}{k_\mathrm{p}}) \\ \frac{k_\mathrm{z}^\mathrm{p}}{Z_\mathrm{c,p} k_\mathrm{p}} \sinh(\frac{\Gamma_\mathrm{p} t_\mathrm{p} k_\mathrm{z}^\mathrm{p}}{k_\mathrm{p}}) & \cosh(\frac{\Gamma_\mathrm{p} t_\mathrm{p} k_\mathrm{z}^\mathrm{p}}{k_\mathrm{p}}) \end{bmatrix}, \tag{3.8}$$

and

$$\begin{cases} k_\mathrm{z}^\mathrm{p} = \sqrt{k_\mathrm{p}^2 - k_\mathrm{tr}^2} & \text{if} \quad k_\mathrm{tr} \leqslant k_\mathrm{p} \\ k_\mathrm{z}^\mathrm{p} = -\mathrm{i}\sqrt{k_\mathrm{tr}^2 - k_\mathrm{p}^2} & \text{if} \quad k_\mathrm{tr} > k_\mathrm{p} \end{cases}. \tag{3.9}$$

$Z_\mathrm{c,p}$ and $\Gamma_\mathrm{p} = \mathrm{i}k_\mathrm{p}$ represent respectively the complex characteristic impedance and the complex propagation coefficient. The empirical study in [33] resulted in the following expressions:

$$Z_\mathrm{c,p} = \rho_\mathrm{a} c_\mathrm{a}\left(1 + 0.0571\left(\frac{\rho_\mathrm{a} f}{\sigma_\mathrm{p}}\right)^{-0.754} - \mathrm{i}0.087\left(\frac{\rho_\mathrm{a} f}{\sigma_\mathrm{p}}\right)^{-0.732}\right), \tag{3.10}$$

$$\Gamma_\mathrm{p} = \frac{\mathrm{i}\omega}{c_\mathrm{a}}\left(1 + 0.0978\left(\frac{\rho_\mathrm{a} f}{\sigma_\mathrm{p}}\right)^{-0.7} - \mathrm{i}0.189\left(\frac{\rho_\mathrm{a} f}{\sigma_\mathrm{p}}\right)^{-0.595}\right). \tag{3.11}$$

The empirical relations are only a function of the flow resistivity σ_{p} of the porous layer. Due to its simplicity, it is a widely used model for poro-elastic layers.

When the frame of the poro-elastic material is mechanically excited e.g. when the layer is glued to a solid layer, a more elaborate model may be needed such as the Biot model [10, 11]. The Biot model was employed for acoustic purposes in a Biot-Allard model [3]. In this model, three sorts of waves propagate at the same time through the solid frame of the material and the fluid in the pores: two longitudinal waves and one shear wave. A set of six variables is used to characterize the acoustic field:

$$\mathbf{m}^{\mathrm{p}}_{\mathrm{M}_{2j-1}} = \mathbf{T}^{\mathrm{p},(j)}(\omega, k_{\mathrm{tr}})\mathbf{m}^{\mathrm{p}}_{\mathrm{M}_{2j}}, \tag{3.12}$$

$$\text{with} \quad \mathbf{m}^{\mathrm{p}}_{\mathrm{M}} = [v^{\mathrm{s}}_{\mathrm{x,M}}\ v^{\mathrm{s}}_{\mathrm{z,M}}\ \ v^{\mathrm{f}}_{\mathrm{z,M}}\ \sigma^{\mathrm{s}}_{\mathrm{zz,M}}\ \sigma^{\mathrm{s}}_{\mathrm{xz,M}}\ \sigma^{\mathrm{f}}_{\mathrm{zz,M}}]^{\mathrm{T}}, \tag{3.13}$$

in which subscript s denotes the solid frame, while subscript f indicates the fluid phase. An explicit expression for the elements of the transfer matrix $\mathbf{T}^{\mathrm{p},(j)}(\omega, k_{\mathrm{tr}}) \in \mathbb{C}^{6\times 6}$ are given in [3, 43]. The material properties needed to compute this transfer matrix are the density ρ_{p}, the Young's modulus E_{p}, the shear modulus G_{p}, the tortuosity $\alpha_{\mathrm{p},\infty}$, the porosity ϕ_{p}, the flow resistivity σ_{p}, the characteristic viscous length $\Lambda_{\mathrm{p,l}}$ and the characteristic thermal length $\Lambda_{\mathrm{p,t}}$ of the porous layer.

Interface Matrices

Compatibility between adjacent layers i and j is described by interface matrices $\mathbf{I}_{ij}$ and $\mathbf{J}_{ij}$, such that:

$$\mathbf{I}_{ij}\mathbf{m}_{\mathrm{M}_i} + \mathbf{J}_{ij}\mathbf{m}_{\mathrm{M}_j} = \mathbf{0}. \tag{3.14}$$

Dependent on the type of layers, the continuity conditions will differ.

In case of two adjacent (equivalent) fluid layers, the interface matrices $\mathbf{I}_{\mathrm{ff}}$ and $\mathbf{J}_{\mathrm{ff}}$ are respectively a 2×2 identity matrix and its negative such that $\mathbf{m}^{\mathrm{f}}_{\mathrm{M}_i} = \mathbf{m}^{\mathrm{f}}_{\mathrm{M}_j}$. Similar for two adjacent solid layers, $\mathbf{m}^{\mathrm{s}}_{\mathrm{M}_i} = \mathbf{m}^{\mathrm{s}}_{\mathrm{M}_j}$, the interface matrices $\mathbf{I}_{\mathrm{ss}}$ and $\mathbf{J}_{\mathrm{ss}}$ are respectively a 4×4 identity matrix and its negative. For two coupled poro-elastic layers modelled by Biot-Allard models, the continuity conditions depend on the porosities of the layers. By choosing $\mathbf{I}_{\mathrm{pp}}$ to be a 6×6 identity

matrix, $\mathbf{J}_{\mathrm{pp}}$ becomes:

$$\mathbf{I}_{\mathrm{pp}} = \begin{bmatrix} 1 & 0 & 0 & 0 & 0 & 0 \\ 0 & 1 & 0 & 0 & 0 & 0 \\ 0 & 0 & 1 & 0 & 0 & 0 \\ 0 & 0 & 0 & 1 & 0 & 0 \\ 0 & 0 & 0 & 0 & 1 & 0 \\ 0 & 0 & 0 & 0 & 0 & 1 \end{bmatrix}, \; \mathbf{J}_{\mathrm{pp}} = \begin{bmatrix} 1 & 0 & 0 & 0 & 0 & 0 \\ 0 & 1 & 0 & 0 & 0 & 0 \\ 0 & 1-\phi_j/\phi_i & \phi_j/\phi_i & 0 & 0 & 0 \\ 0 & 0 & 0 & 1 & 0 & 1-\phi_i/\phi_j \\ 0 & 0 & 0 & 0 & 1 & 0 \\ 0 & 0 & 0 & 0 & 0 & \phi_i/\phi_j \end{bmatrix}. \tag{3.15}$$

In case of a(n) (equivalent) fluid-solid interface or solid-(equivalent) fluid interface, the continuity conditions are captured by the following interface matrices:

$$\mathbf{I}_{\mathrm{fs}} = \mathbf{J}_{\mathrm{sf}} = \begin{bmatrix} 0 & -1 \\ 1 & 0 \\ 0 & 0 \end{bmatrix}, \; \mathbf{J}_{\mathrm{fs}} = \mathbf{I}_{\mathrm{sf}} = \begin{bmatrix} 0 & 1 & 0 & 0 \\ 0 & 0 & 1 & 0 \\ 0 & 0 & 0 & 1 \end{bmatrix}, \tag{3.16}$$

For a(n) (equivalent) fluid-porous interface or porous-(equivalent) fluid interface, the interface matrices are:

$$\mathbf{I}_{\mathrm{fp}} = \mathbf{J}_{\mathrm{pf}} = \begin{bmatrix} 0 & -1 \\ \phi_j & 0 \\ 1-\phi_j & 0 \\ 0 & 0 \end{bmatrix}, \; \mathbf{J}_{\mathrm{fp}} = \mathbf{I}_{\mathrm{pf}} = \begin{bmatrix} 0 & 1-\phi_j & \phi_j & 0 & 0 & 0 \\ 0 & 0 & 0 & 0 & 0 & 1 \\ 0 & 0 & 0 & 1 & 0 & 0 \\ 0 & 0 & 0 & 0 & 1 & 0 \end{bmatrix}, \tag{3.17}$$

The solid-porous interface matrices and the porous-solid interface matrices are given by:

$$\mathbf{I}_{\mathrm{sp}} = \mathbf{J}_{\mathrm{ps}} = \begin{bmatrix} 1 & 0 & 0 & 0 \\ 0 & 1 & 0 & 0 \\ 0 & 1 & 0 & 0 \\ 0 & 0 & 1 & 0 \\ 0 & 0 & 0 & 1 \end{bmatrix}, \; \mathbf{J}_{\mathrm{sp}} = \mathbf{I}_{\mathrm{ps}} = \begin{bmatrix} 1 & 0 & 0 & 0 & 0 & 0 \\ 0 & 1 & 0 & 0 & 0 & 0 \\ 0 & 0 & 1 & 0 & 0 & 0 \\ 0 & 0 & 0 & 1 & 0 & 1 \\ 0 & 0 & 0 & 0 & 0 & 1 \end{bmatrix}, \tag{3.18}$$

Global transfer matrix

Finally, the transfer matrices and interface matrices are assembled in a global transfer matrix, describing the dynamic behaviour of the multilayered system shown in Fig. 3.2. The system is enclosed by two semi-acoustic fluid halfspaces in A and B. The transition to the parameters in the fluid space i.e. the pressure and velocity in A and B, is accounted for by adding interface matrices connecting

the multilayered system to the adjacent fluid halfspaces. The global transfer matrix $\mathbf{G}(\omega, k_{\mathrm{tr}}) \in \mathbb{C}^{(R-2)\times R}$ becomes:

$$\mathbf{G}(\omega, k_{\mathrm{tr}}) = \begin{bmatrix} \mathbf{I}_{\mathrm{f1}} & \mathbf{J}_{\mathrm{f1}}\mathbf{T}^{(1)} & \mathbf{0} & \dots & \mathbf{0} & \mathbf{0} & \mathbf{0} \\ \mathbf{0} & \mathbf{I}_{12} & \mathbf{J}_{12}\mathbf{T}^{(2)} & \dots & \mathbf{0} & \mathbf{0} & \mathbf{0} \\ \vdots & \vdots & \vdots & \ddots & \vdots & \vdots & \vdots \\ \mathbf{0} & \mathbf{0} & \mathbf{0} & \dots & \mathbf{I}_{n-1,1} & \mathbf{J}_{n-1,n}\mathbf{T}^{(n)} & \mathbf{0} \\ \mathbf{0} & \mathbf{0} & \mathbf{0} & \dots & \mathbf{0} & \mathbf{I}_{nf} & \mathbf{J}_{nf} \end{bmatrix}, \tag{3.19}$$

so that the system of equations equals:

$$\mathbf{G}(\omega, k_{\mathrm{tr}})\mathbf{m} = \mathbf{0}, \tag{3.20}$$

with $\mathbf{m} \in \mathbb{C}^{R\times 1}$, the vector collecting the variables describing the propagation of the sound waves through the multilayered system:

$$\mathbf{m} = [{\mathbf{m}_{\mathrm{A}}^{\mathrm{f}}}^{\mathrm{T}} \; {\mathbf{m}_{\mathrm{M}_2}^{(1)}}^{\mathrm{T}} \; {\mathbf{m}_{\mathrm{M}_4}^{(2)}}^{\mathrm{T}} \; \dots \; {\mathbf{m}_{\mathrm{B}}^{\mathrm{f}}}^{\mathrm{T}}]^{\mathrm{T}}. \tag{3.21}$$

Mechanical impedance matrix

The mechanical impedance matrix $\mathbf{Z}(\omega, k_{\mathrm{tr}})$ relates the pressures and velocities at either sides of the wall:

$$\mathbf{Z}(\omega, k_{\mathrm{tr}}) \begin{bmatrix} v_{\mathrm{z,A}}^{\mathrm{f}} \\ v_{\mathrm{z,B}}^{\mathrm{f}} \end{bmatrix} = \begin{bmatrix} Z_{11} & Z_{12} \\ Z_{21} & Z_{22} \end{bmatrix} \begin{bmatrix} v_{\mathrm{z,A}}^{\mathrm{f}} \\ v_{\mathrm{z,B}}^{\mathrm{f}} \end{bmatrix} = \begin{bmatrix} p_{\mathrm{A}} \\ p_{\mathrm{B}} \end{bmatrix} \tag{3.22}$$

The elements of $\mathbf{Z}(\omega, k_{\mathrm{tr}}) \in \mathbb{C}^{4\times 4}$ are determined using the earlier defined global transfer matrix $\mathbf{G}(\omega, k_{\mathrm{tr}})$ [35]. The derivation is shown for Z_{12}. The other elements of $\mathbf{Z}$ can be determined in a similar manner. For Z_{12} , the following is true:

$$Z_{12} = \left.\frac{p_{\mathrm{A}}}{v_{\mathrm{z,B}}^{\mathrm{f}}}\right|_{v_{\mathrm{z,A}}^{\mathrm{f}}=0} \tag{3.23}$$

Adding this condition to the system of equations defined in Eq. (3.20), results in:

$$\mathbf{G}_{12}(\omega, k_{\mathrm{tr}})\mathbf{m} = \begin{bmatrix} -1 & 0 & 0 & \dots & 0 & 0 & Z_{12} \\ 0 & 1 & 0 & \dots & 0 & 0 & 0 \\ & & & \mathbf{G} & & & \end{bmatrix} \mathbf{m} = \mathbf{0}. \tag{3.24}$$

The square matrix $\mathbf{G}_{12}(\omega, k_{\mathrm{tr}}) \in \mathbb{C}^{R\times R}$ is linearly dependent. Therefore, the equations can be solved for Z_{12}, by taking the determinant of $\mathbf{G}_{12}$ and expanding it along the first two rows. This results in:

$$Z_{12}(\omega, k_{\mathrm{tr}}) = \frac{|\mathbf{G}_{1,2}|}{|\mathbf{G}_{2,R}|}, \tag{3.25}$$

where $|\mathbf{G}_{r,s}|$ is the determinant of $\mathbf{G}$, in which the columns r and s are eliminated.

Similarly, the other elements of $\mathbf{Z}(\omega, k_{\mathrm{tr}})$ are [32]:

$$Z_{11}(\omega, k_{\mathrm{tr}}) = -\frac{|\mathbf{G}_{1,R}|}{|\mathbf{G}_{2,R}|}, \quad Z_{12}(\omega, k_{\mathrm{tr}}) = \frac{|\mathbf{G}_{1,2}|}{|\mathbf{G}_{2,R}|},$$

$$Z_{21}(\omega, k_{\mathrm{tr}}) = -\frac{|\mathbf{G}_{R-1,R}|}{|\mathbf{G}_{2,R}|}, \quad Z_{22}(\omega, k_{\mathrm{tr}}) = -\frac{|\mathbf{G}_{2,R-1}|}{|\mathbf{G}_{2,R}|}$$

3.2.2 Airborne sound prediction

The conventional transfer matrix method can be used to compute oblique sound transmission [3, 43]. Consider an infinite multilayered system, excited by an incoming wave at a certain angle θ, as illustrated in figure 3.3. The trace wavenumber is then $k_{\mathrm{tr}} = k_{\mathrm{a}} \sin\theta$ with k_{a} the wavenumber in air.

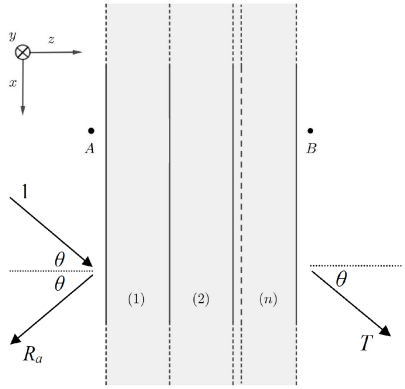

Figure 3.3: Incoming plane wave at an angle θ, exciting the multilayered system (Adapted figure from [43]).

To solve the system of equations in Eq. (3.20), two extra conditions, relating the pressures and velocities at both sides in A and B, are defined. In A the surface impedance of the multilayered system Z_{A} is defined, so that:

$$Z_{\mathrm{A}} = \frac{p_{\mathrm{A}}}{v^{\mathrm{f}}_{\mathrm{z,A}}}. \tag{3.26}$$

The pressure and velocity in B for a plane wave are related as follows:

$$Z_{\mathrm{B}} = \frac{p_{\mathrm{B}}}{v^{\mathrm{f}}_{\mathrm{z,B}}}, \tag{3.27}$$

with

$$Z_{\mathrm{B}} = \frac{Z_{\mathrm{c}} k_{\mathrm{a}}}{\sqrt{k_{\mathrm{a}}^2 - k_{\mathrm{tr}}^2}} = \frac{Z_{\mathrm{c}}}{\cos\theta}, \tag{3.28}$$

and with $Z_{\mathrm{c}} = \rho_{\mathrm{a}} c_{\mathrm{a}}$ the characteristic impedance of air. Eq. (3.28) is valid for all frequencies, as $k_{\mathrm{a}} \geq k_{\mathrm{tr}}$ for plane wave excitation.

Adding the two conditions described in Eqs. (3.26) and (3.27) to the system of equations in Eq. (3.20), gives:

$$\begin{bmatrix} -1 & Z_{\mathrm{A}} & \dots & 0 & 0 \\ 0 & 0 & \dots & -1 & Z_{\mathrm{c}}/\cos\theta \\ & & \mathbf{G} & & \end{bmatrix} \mathbf{m} = \begin{bmatrix} -1 & Z_{\mathrm{A}} & \dots & 0 & 0 \\ & & \mathbf{G}' & & \end{bmatrix} \mathbf{m} = \mathbf{0}. \tag{3.29}$$

The system of equations is solved for $Z_{\mathrm{A}}(\theta)$, via the determinant of the obtained square matrix and expanding it along the first row, so that:

$$Z_{\mathrm{A}}(\theta) = -\frac{|\mathbf{G}'_1|}{|\mathbf{G}'_2|}, \tag{3.30}$$

where $|\mathbf{G}'_r|$ is the determinant of $\mathbf{G}'$, in which the rth column is eliminated.

Next, the plane wave reflection coefficient R_{A} at the surface of a layer is defined as the ratio between the pressures created by the reflected and incident waves at the surface of that layer. It can be obtained via the surface impedance Z_{A}, determined in Eq. (3.30) [3]:

$$R_{\mathrm{A}}(\theta) = \frac{Z_{\mathrm{A}}(\theta)\cos\theta - Z_{\mathrm{c}}}{Z_{\mathrm{A}}(\theta)\cos\theta + Z_{\mathrm{c}}}. \tag{3.31}$$

Finally, the plane wave transmission coefficient $T(\theta)$ is the ratio of the pressure of the transmitted wave through a layer to the pressure caused by the incident wave on the other side of the layer. Combining the definitions of the reflection and transmission coefficient leads to:

$$p_{\mathrm{A}}\left(\frac{T(\theta)}{1 + R_{\mathrm{A}}(\theta)}\right) - p_{\mathrm{B}} = 0. \tag{3.32}$$

This equation is added to the system of equations, defined in Eq. (3.29). Again, the determinant of the obtained matrix is elaborated according to the first row:

$$T(\theta) = (1 + R_{\mathrm{A}}(\theta))\frac{|\mathbf{G}'_{R-1}|}{|\mathbf{G}'_R|}. \tag{3.33}$$

The oblique sound transmission loss $R(\theta)$ and the oblique sound transmission coefficient $\tau_{12}(\theta)$ are then:

$$R(\theta) = -10\log\tau_{12}(\theta), \qquad \text{and} \qquad \tau_{12}(\theta) = |T(\theta)|^2. \tag{3.34}$$

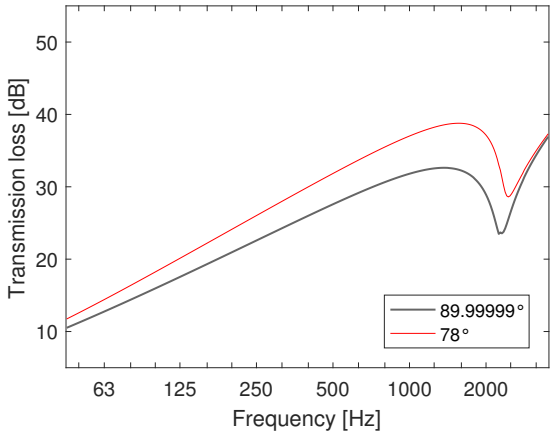

Figure 3.4: The sound transmission loss of a polymethyl methacrylate panel as predicted by a conventional transfer matrix method, for which the upper bound of the angle of incidence is chosen to be 89.99999° (black line) or 78° (red line).

In order to obtain the diffuse sound transmission loss, the sound transmission coefficient is integrated over all possible angles of incidence:

$$R = -10 \log \tau_{12}, \qquad \text{and} \qquad \tau_{12} = \frac{\int_0^{\pi/2} \tau_{12}(\theta) \sin\theta \cos\theta \mathrm{d}\theta}{\int_0^{\pi/2} \sin\theta \cos\theta \mathrm{d}\theta}. \tag{3.35}$$

Note that numerical issues occur for the sound transmission at grazing incidence. Therefore, an arbitrary choice is made for the upper bound in the integral. Some authors choose to limit the upper bound to 78° instead of 90° in order to account for the inevitable niche around the test sample in a laboratory environment and neglect waves close to grazing incidence [43, 118]. In the present work, the upper bound is chosen to be close to 90° with a tolerance of 10^{-5}°. The influence of the upper bound is illustrated in Fig. 3.4 for a polymethyl methacrylate panel, from which the material properties are detailed in section 3.5.1.

3.3 Accounting for finite size effects

The conventional TMM predicts the STL for infinite multilayered systems. Two techniques can be applied to account for finite size. The first technique to be introduced in section 3.3.1, is already widely used and known as the spatial windowing technique. In essence, out-of-plane motion outside the structure's dimensions is then neglected in the sound transmission loss prediction. The

method accounts however only for diffraction effects and neglects the modal behaviour of the test sample, which might influence the sound transmission loss in the considered frequency range. A second technique is therefore elaborated in section 3.3.2, which approximately accounts for modal behaviour by decomposing the displacements into a set of sinusoidal basis functions.

3.3.1 Spatial windowing technique

When an infinitely-sized plate is excited by a travelling wave with incident angle θ as depicted in figure 3.5(a), the associated excitation pressure field in the wavenumber domain is described by a Dirac delta function (cfr. Fig. 3.5(b)). A single peak at $k_{\mathrm{tr}} = k_{\mathrm{a}} \sin\theta$ is noticed in the excitation spectrum. Consequently, only a wave with trace wavenumber k_{tr} will travel through the infinite structure as illustrated in Fig. 3.6.

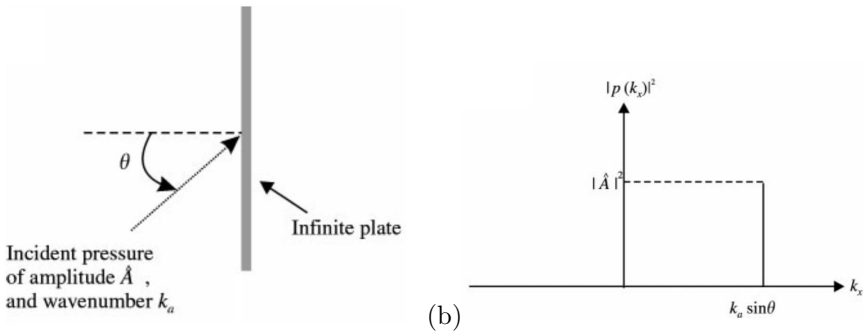

Figure 3.5: The infinite plate in (a) is excited by an incoming plane wave at a particular angle θ. The associated excitation pressure field in the wavenumber spectrum is shown in (b) [119].

Applying spatial windowing means that only a diaphragm with the same dimensions as the one of the finite system is considered as in Fig. 3.7(a) [119]. The finite size of the test sample is then approximately accounted for. Figure 3.7(b) shows that the velocity field is then distributed out over the wavenumber domain, with a peak at $k_{\mathrm{tr}} = k_{\mathrm{a}} \sin\theta$. Note that because of this windowed velocity field, also resonant transmission will be generated besides non-resonant transmission even when the excitation frequency is smaller than the critical frequency of the plate.

In case of a two-dimensional planar structure, the x- and y-component of the trace wavenumber $k_{\mathrm{tr}} = k_{\mathrm{a}} \sin\theta$ are respectively $k_{\mathrm{tr,x}} = k_{\mathrm{tr}} \cos\alpha$ and

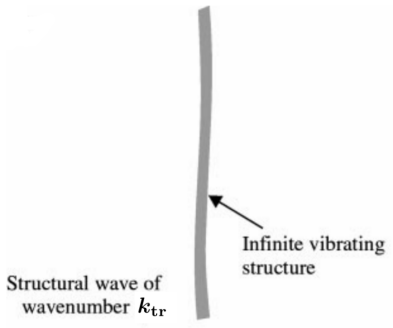

(a)

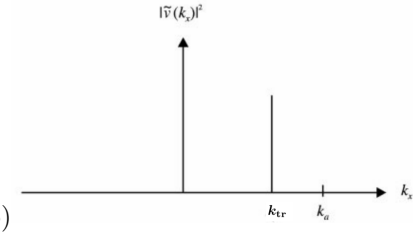

(b)

Figure 3.6: The infinite plate in (a) is excited by an incoming plane wave inducing a travelling wave in the plate with trace wavenumber k_{tr}. The associated velocity field in the wavenumber spectrum is shown in (b) [119].

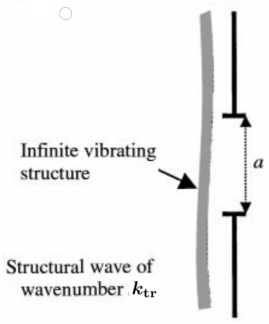

(a)

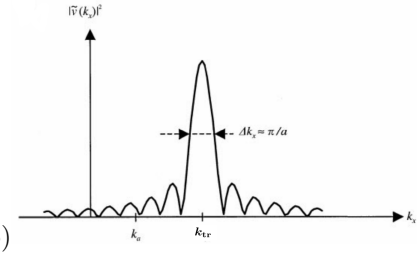

(b)

Figure 3.7: The plate in (a) is excited by an incoming plane wave at a particular angle θ. Spatial windowing accounts for diffraction effects. The associated velocity field in the wavenumber spectrum is shown in (b) [119].

$k_{\mathrm{tr,y}} = k_{\mathrm{tr}} \sin\alpha$ with α the direction of the wave as indicated in Fig. 3.8. The velocity field of a structural wave with wavenumbers $(k_{\mathrm{tr,x}}, k_{\mathrm{tr,y}})$ is:

$$v_{\mathrm{z}}(x, y, k_{\mathrm{tr}}, \alpha) = v_0 \mathrm{e}^{-\mathrm{i}k_{\mathrm{tr,x}}x} \mathrm{e}^{-\mathrm{i}k_{\mathrm{tr,y}}y}, \tag{3.36}$$

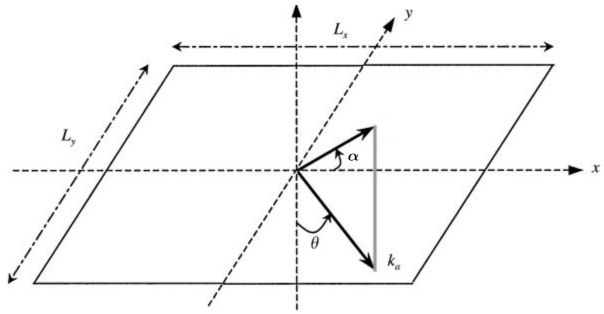

Figure 3.8: Indication of incidence angle θ and direction α of an incoming wave (adapted figure from [119]).

The finite size of the panel is accounted for by transforming the velocity field into the wavenumber domain, as follows [119]:

$$\tilde{v}_\mathrm{z}(k_\mathrm{x}, k_\mathrm{y}, k_\mathrm{tr}, \alpha) = v_0 \int_{-L_\mathrm{x}/2}^{L_\mathrm{x}/2} \int_{-L_\mathrm{y}/2}^{L_\mathrm{y}/2} \mathrm{e}^{-\mathrm{i}k_{\mathrm{tr,x}}x} \mathrm{e}^{-\mathrm{i}k_{\mathrm{tr,y}}y} \mathrm{e}^{\mathrm{i}k_\mathrm{x}x} \mathrm{e}^{\mathrm{i}k_\mathrm{y}y} \mathrm{d}x\mathrm{d}y \tag{3.37}$$

$$= v_0 L_\mathrm{x} L_\mathrm{y} \frac{\sin((k_\mathrm{x} - k_{\mathrm{tr,x}})L_\mathrm{x}/2)}{((k_\mathrm{x} - k_{\mathrm{tr,x}})L_\mathrm{x}/2)} \cdot \frac{\sin((k_\mathrm{y} - k_{\mathrm{tr,y}})L_\mathrm{y}/2)}{((k_\mathrm{y} - k_{\mathrm{tr,y}})L_\mathrm{y}/2)}. \tag{3.38}$$

In the transformation, it is important that only the part of the surface area of the panel $L_\mathrm{x} \times L_\mathrm{y}$ is accounted for. Next, the radiated power due to this velocity distribution is determined. The time-averaged radiated power P for a velocity distribution and corresponding surface pressure field is:

$$P(k_\mathrm{tr}, \alpha) = \frac{1}{2}\mathrm{Re}\left\{ \int_{-L_\mathrm{x}/2}^{L_\mathrm{x}/2} \int_{-L_\mathrm{y}/2}^{L_\mathrm{y}/2} p(x, y, k_\mathrm{tr}, \alpha) v_\mathrm{z}^*(x, y, k_\mathrm{tr}, \alpha) \mathrm{d}x\mathrm{d}y \right\}. \tag{3.39}$$

Further elaboration of this equation involves transforming the pressure and velocity field into the wavenumber domain and relating the pressure field to the velocity field via the Green's function in a similar manner as in §2.5.3. Conversion into polar coordinates (k_r, ϕ) results in [41, 119]:

$$P(k_\mathrm{tr}, \alpha) = \frac{Z_\mathrm{c}}{8\pi^2} \int_0^{k_\mathrm{a}} \int_0^{2\pi} \frac{|\tilde{v}(k_\mathrm{r}\cos\phi, k_\mathrm{r}\sin\phi, k_\mathrm{tr}, \alpha)|^2}{\sqrt{k_\mathrm{a}^2 - k_\mathrm{r}^2}} k_\mathrm{a} k_\mathrm{r} \mathrm{d}\phi \mathrm{d}k_\mathrm{r}. \tag{3.40}$$

Inserting the found radiated power $P(k_\mathrm{tr}, \alpha)$ into:

$$\sigma(k_\mathrm{tr}, \alpha) = \frac{2P(k_\mathrm{tr}, \alpha)}{Z_\mathrm{c} L_\mathrm{x} L_\mathrm{x} |v_0|^2}, \tag{3.41}$$

leads to the following expression of the radiation efficiency $\sigma(k_{\mathrm{tr}}, \alpha)$ for a structural plane wave:

$$\sigma(k_{\mathrm{tr}}, \alpha) = \frac{L_{\mathrm{x}} L_{\mathrm{y}}}{\pi^2} \int_0^{k_{\mathrm{a}}} \int_0^{2\pi} \left[\frac{1 - \cos((k_{\mathrm{r}} \cos\phi - k_{\mathrm{tr,x}}) L_{\mathrm{x}}/2)}{((k_{\mathrm{r}} \cos\phi - k_{\mathrm{tr,x}}) L_{\mathrm{x}}/2)^2} \right] \times \left[\frac{1 - \cos((k_{\mathrm{r}} \sin\phi - k_{\mathrm{tr,y}}) L_{\mathrm{y}}/2)}{((k_{\mathrm{r}} \sin\phi - k_{\mathrm{tr,y}}) L_{\mathrm{y}}/2)^2} \right] \cdot \frac{k_{\mathrm{a}} k_{\mathrm{r}}}{\sqrt{k_{\mathrm{a}}^2 - k_{\mathrm{r}}^2}} \mathrm{d}\phi \mathrm{d}k_{\mathrm{r}}. \tag{3.42}$$

The sound transmission $\tau_{12,\mathrm{fin}}(\theta, \alpha)$ for a finite-sized multilayered building element is the ratio of the transmitted sound power $P_{\mathrm{t,fin}}$ to the incident power $P_{\mathrm{inc,fin}}$. For the sound transmission of an infinite panel $\tau_{12,\mathrm{inf}}$, this can be simplified to the ratio of transmitted intensity $I_{\mathrm{t,inf}}$ to the incident intensity $I_{\mathrm{inc,inf}}$. Using the definition of the sound transmission, it can be found that the sound transmission of the finite-sized panel $\tau_{12,\mathrm{fin}}(\theta, \alpha)$ relates to the radiation efficiency of the finite-sized plate $\sigma(k_{\mathrm{tr}}, \alpha)$ as follows [120]:

$$\tau_{12,\mathrm{fin}}(\theta, \alpha) = \frac{P_{\mathrm{t,fin}}(k_{\mathrm{tr}}, \alpha)}{P_{\mathrm{inc,fin}}}, \tag{3.43}$$

$$= \frac{P_{\mathrm{t,fin}}(k_{\mathrm{tr}}, \alpha)}{I_{\mathrm{inc,inf}} L_{\mathrm{x}} L_{\mathrm{y}}}, \tag{3.44}$$

$$= \frac{I_{\mathrm{t,inf}}}{I_{\mathrm{inc,inf}}} \cdot \frac{P_{\mathrm{t,fin}}(k_{\mathrm{tr}}, \alpha)}{I_{\mathrm{t,inf}} L_{\mathrm{x}} L_{\mathrm{y}}}, \tag{3.45}$$

$$= \tau_{12,\mathrm{inf}}(\theta) \cdot \frac{2 \cos\theta P_{\mathrm{t,fin}}(k_{\mathrm{tr}}, \alpha)}{Z_{\mathrm{c}} L_{\mathrm{x}} L_{\mathrm{y}} |v_0|^2}, \tag{3.46}$$

$$= \tau_{12,\mathrm{inf}}(\theta) \sigma(k_{\mathrm{tr}}, \alpha) \cos\theta. \tag{3.47}$$

Mind that $\sigma(k_{\mathrm{tr}}, \alpha)$, computed using Eq. (3.42), is only dependent on the size of the test sample and not on the material properties of the structure. The computation therefore only needs to be performed once for a given transmission opening.

Finally, the sound transmission for a panel with finite-size correction for diffuse field excitation is found by integrating the oblique sound transmission over all possible angles of incidence:

$$\tau_{12,\mathrm{fin}} = \frac{\int_0^{\pi/2} \int_0^{2\pi} \tau_{12,\mathrm{fin}}(\theta, \alpha) \sin\theta \cos\theta \mathrm{d}\theta \mathrm{d}\alpha}{\int_0^{\pi/2} \int_0^{2\pi} \sin\theta \cos\theta \mathrm{d}\theta \mathrm{d}\alpha}. \tag{3.48}$$

So, when solving for the diffuse sound transmission of a multilayered system with finite-size correction, Eqs. (3.42), (3.47) and (3.48) are combined, resulting in

a quadruple integral. Since this evaluation requires a significant computational cost, multiple revised formulations for the calculation of the radiation efficiency have been suggested. Rhazi and Atalla proposed an analytical simplification of Eq. (3.42) in [89]. The formulation revised by Bonfiglio et al. in [12] reduces the quadruple integral into a double integral by assuming square test samples. Vigran presented a one-dimensional simplification of Eq. (3.42) for isotropic materials with comparable lateral dimensions, which is not applicable for orthotropic panels. The latter was used in the present work and referred to as a TMM with a simplified finite-size correction (fTMM).

The concept of the suggested one-dimensional simplification is that the two planar dimensions of test samples measured in laboratory environments are comparable. Therefore, a typical dimension $L = (L_\mathrm{x} \cdot L_\mathrm{y})^{1/2}$ is used to characterize the window.

For the one-dimensional case, the velocity field in the wavenumber domain of Eq. (3.36) becomes:

$$\tilde{v}_\mathrm{z}(k, k_\mathrm{tr}) = v_0 \int_{-L/2}^{L/2} \mathrm{e}^{-\mathrm{i}k_\mathrm{tr}x} \mathrm{e}^{\mathrm{i}kx} \mathrm{d}x \tag{3.49}$$

$$= v_0 L \frac{\sin((k - k_\mathrm{tr})L/2)}{((k - k_\mathrm{tr})L/2)}, \tag{3.50}$$

so that Eq. (3.40) is simplified to:

$$P(k_\mathrm{tr}) = \frac{k_\mathrm{a} Z_\mathrm{c}}{4\pi} \int_0^{k_\mathrm{a}} \frac{|\tilde{v}(k_\mathrm{r}, k_\mathrm{tr})|^2}{\sqrt{k_\mathrm{a}^2 - k_\mathrm{r}^2}} \mathrm{d}k_\mathrm{r}. \tag{3.51}$$

Substituting Eq. (3.51) and Eq. (3.49) in Eq. (3.41), gives the following expression for the radiation efficiency:

$$\sigma(k_\mathrm{tr}) = \frac{L k_\mathrm{a}}{2\pi} \int_0^{k_\mathrm{a}} \frac{\sin^2((k_\mathrm{r} - k_\mathrm{tr})L/2)}{((k_\mathrm{r} - k_\mathrm{tr})L/2)^2 \cdot \sqrt{k_\mathrm{a}^2 - k_\mathrm{r}^2}} \mathrm{d}k_\mathrm{r}. \tag{3.52}$$

Note that the radiation efficiency is not dependent on the direction α. For the computation of the diffuse sound transmission, Eq. (3.48) reduces again to a single integral over θ as in Eq. (3.35).

3.3.2 Approximating modal behaviour

Note that in case of spatial windowing, finite dimensions are considered by restricting propagation of waves to a diaphragm. Structural waves are

propagating within the structure, classifying the fTMM as a wave approach. In reality, the structure is bounded, causing the travelling waves to be reflected at the boundaries. The waves and their reflections add up to standing waves. This modal behaviour can be important for sound transmission in the low- and mid-frequency range, where the structure is modally sparse. It is therefore investigated in this section how modal behaviour can be approximated in the TMM for a simply supported structure [36, 90].

It was explained in §2.5.1 that the displacements of a structure can be decomposed into a finite set of basis functions, describing the modal behaviour of the structure. The exact mode shapes and natural frequencies for a structure of finite lateral dimensions cannot be obtained using the two-dimensional TMM for infinitely-sized structures. Hence, the normal displacements at the room-wall interface are approximated using a Ritz approach, i.e. by means of a finite set of basis functions that satisfy the boundary conditions. In case of simply supported boundary conditions, a natural choice for the basis functions are then sinusoidal basis functions, which allow rotations at the boundaries, while restraining the normal displacements at the boundaries [36, 90]. For a structure with dimensions $L_\mathrm{x} \times L_\mathrm{y}$, the sinusoidal basis functions $\boldsymbol{\psi}_{\mathrm{sin},l}$ are:

$$\psi_{\mathrm{sin},l}(x,y) = \sin\left(\frac{l_\mathrm{x}\pi x}{L_\mathrm{x}}\right)\sin\left(\frac{l_\mathrm{y}\pi y}{L_\mathrm{y}}\right), \tag{3.53}$$

where l_x and l_y denote the integer number of half wavelengths in the x and y directions, respectively, of mode l. The corresponding structural wavenumbers in x- and y direction are:

$$k_{\mathrm{sin},l\mathrm{x}} = \frac{l_\mathrm{x}\pi}{L_\mathrm{x}}, \qquad k_{\mathrm{sin},l\mathrm{y}} = \frac{l_\mathrm{y}\pi}{L_\mathrm{y}}, \tag{3.54}$$

so that the wavenumber for a basis function $\boldsymbol{\psi}_{\mathrm{sin},l}$ is:

$$k_{\mathrm{sin},l} = \sqrt{k_{\mathrm{sin},l\mathrm{x}}^2 + k_{\mathrm{sin},l\mathrm{y}}^2}. \tag{3.55}$$

To predict the behaviour of the multilayered system for an imposed, sinusoidal displacement field $\boldsymbol{\psi}_{\mathrm{sin},l}$ using the two-dimensional transfer matrix method, the trace wavenumber k_tr is taken to be the wavenumber of the corresponding sinusoidal basis function $k_{\mathrm{sin},l}$. In the remainder of this section, it is demonstrated how this decomposition can be used in the transfer matrix method to predict the sound transmission loss, while approximately accounting for modal behaviour. The method is referred to as the approximate modal TMM (mTMM).

In case of oblique sound transmission, an incident pressure field is created by an incoming wave with unit amplitude, incidence angle θ and direction α (cfr. Fig. 3.8):

$$p_\mathrm{inc} = \mathrm{e}^{-\mathrm{i}k_{\mathrm{inc,x}}x}\mathrm{e}^{-\mathrm{i}k_{\mathrm{inc,y}}y}, \tag{3.56}$$

where

$$k_{\mathrm{inc,x}} = k_{\mathrm{a}} \sin\theta \cos\alpha \quad \text{and} \quad k_{\mathrm{inc,y}} = k_{\mathrm{a}} \sin\theta \sin\alpha. \tag{3.57}$$

Rewriting the incident pressure field p_{inc} into a summation of sinusoidal basis functions $\boldsymbol{\psi}_{\mathrm{sin},l}$ and their corresponding generalized coordinates $p_{\mathrm{inc},l}$, gives:

$$p_{\mathrm{inc}}(\omega, x, y) = \sum_l p_{\mathrm{inc},l}(\omega)\psi_{\mathrm{sin},l}(x, y), \tag{3.58}$$

$$\text{with} \quad p_{\mathrm{inc},l}(\omega) = \int_0^{L_{\mathrm{x}}} \int_0^{L_{\mathrm{y}}} p_{\mathrm{inc}}(\omega, x, y)\psi_{\mathrm{sin},l}(x, y)\mathrm{d}x\mathrm{d}y. \tag{3.59}$$

Similarly, the velocities and pressures at both sides of the wall are decomposed as follows:

$$\begin{bmatrix} v^{\mathrm{f}}_{\mathrm{zA}}(\omega, \mathbf{x}) \\ v^{\mathrm{f}}_{\mathrm{zB}}(\omega, \mathbf{x}) \end{bmatrix} = \sum_l \begin{bmatrix} v^{\mathrm{f}}_{\mathrm{zA},l}(\omega) \\ v^{\mathrm{f}}_{\mathrm{zB},l}(\omega) \end{bmatrix} \psi_{\mathrm{sin},l}(\mathbf{x}); \quad \begin{bmatrix} p_{\mathrm{A}}(\omega, \mathbf{x}) \\ p_{\mathrm{B}}(\omega, \mathbf{x}) \end{bmatrix} = \sum_l \begin{bmatrix} p_{\mathrm{A},l}(\omega) \\ p_{\mathrm{B},l}(\omega) \end{bmatrix} \psi_{\mathrm{sin},l}(\mathbf{x}). \tag{3.60}$$

The total pressure on the emitting side consists of the incident and reflected wave: $p_{\mathrm{A}} = (1 + R_{\mathrm{A}})p_{\mathrm{inc}}$. Assuming a hard surface in A ($R_{\mathrm{A}} \approx 1$) while substituting Eq. (3.60) into Eq. (3.22) results in:

$$\begin{cases} \sum_l (Z_{11,l} v^{\mathrm{f}}_{\mathrm{zA},l} + Z_{12,l} v^{\mathrm{f}}_{\mathrm{zB},l})\psi_{\mathrm{sin},l}(x, y) = 2\ p_{\mathrm{inc}}(\omega, x, y), \\ \sum_l (Z_{21,l} v^{\mathrm{f}}_{\mathrm{zA},l} + Z_{22,l} v^{\mathrm{f}}_{\mathrm{zB},l})\psi_{\mathrm{sin},l}(x, y) = \sum_l p_{\mathrm{B},l}\psi_{\mathrm{sin},l}(x, y). \end{cases} \tag{3.61}$$

The mechanical impedance matrix in terms of the generalized coordinates is obtained by using the wavenumber $k_{\mathrm{sin},l}$ as trace wavenumber, such that $\mathbf{Z}_l(\omega) = \mathbf{Z}(\omega, k_{\mathrm{sin},l})$. A weighted residual formulation is then constructed with weight function $\psi_{\mathrm{sin},m}(x, y)$:

$$\begin{cases} \int_0^{L_{\mathrm{x}}} \int_0^{L_{\mathrm{y}}} \left[\sum_l (Z_{11,l} v^{\mathrm{f}}_{\mathrm{zA},l} + Z_{12,l} v^{\mathrm{f}}_{\mathrm{zB},l})\psi_{\mathrm{sin},l}(x, y) \right] \psi_{\mathrm{sin},m}(x, y)\mathrm{d}x\mathrm{d}y \\ \qquad = 2 \int_0^{L_{\mathrm{x}}} \int_0^{L_{\mathrm{y}}} p_{\mathrm{inc}}\psi_{\mathrm{sin},m}(x, y)\mathrm{d}x\mathrm{d}y \\ \int_0^{L_{\mathrm{x}}} \int_0^{L_{\mathrm{y}}} \Big[\sum_l (Z_{21,l} v^{\mathrm{f}}_{\mathrm{zA},l} + Z_{22,l} v^{\mathrm{f}}_{\mathrm{zB},l})\psi_{\mathrm{sin},l}(x, y) \\ \qquad - \sum_l p_{\mathrm{B},l}\psi_{\mathrm{sin},l}(x, y) \Big] \psi_{\mathrm{sin},m}(x, y)\mathrm{d}x\mathrm{d}y = 0. \end{cases} \tag{3.62}$$

Since

$$\int_0^{L_{\mathrm{x}}} \int_0^{L_{\mathrm{y}}} \psi_{\mathrm{sin},l}(x, y)\psi_{\mathrm{sin},m}(x, y)\mathrm{d}x\mathrm{d}y = \delta_{ml} \frac{L_{\mathrm{x}} L_{\mathrm{y}}}{4}, \tag{3.63}$$

the system of Eqs. (3.62) and (3.63) becomes:

$$\begin{bmatrix} Z_{11,l} & Z_{12,l} \\ Z_{21,l} & Z_{22,l} \end{bmatrix} \begin{bmatrix} v^{\mathrm{f}}_{\mathrm{zA},l} \\ v^{\mathrm{f}}_{\mathrm{zB},l} \end{bmatrix} = \begin{bmatrix} \frac{8}{L_{\mathrm{x}} L_{\mathrm{y}}} p_{\mathrm{inc},l} \\ p_{\mathrm{B},l} \end{bmatrix}. \tag{3.64}$$

The acoustic radiation impedance $Z_{\mathrm{rad},l}$ of a finite-sized, baffled panel with a sinusoidal displacement field $\boldsymbol{\psi}_{\mathrm{sin},l}$ is defined as the ratio of the pressure amplitude $p_{\mathrm{B},l}$ to the velocity amplitude $v^{\mathrm{f}}_{\mathrm{zB},l}$ in B:

$$Z_{\mathrm{rad},l} = \frac{p_{\mathrm{B},l}}{v^{\mathrm{f}}_{\mathrm{zB},l}}. \tag{3.65}$$

Multiple methods can be used to obtain the radiation impedance [29, 59, 65], which will be discussed in the next section. Combining Eqs. (3.59), (3.64) and (3.65) allows to compute the incident pressure amplitude $p_{\mathrm{inc},l}$ and the pressure and velocity amplitudes in A and B: $p_{\mathrm{A},l}$, $p_{\mathrm{B},l}$, $v^{\mathrm{f}}_{\mathrm{zA},l}$ and $v^{\mathrm{f}}_{\mathrm{zB},l}$.

Next, the oblique sound transmission $\tau_{12}(\theta,\alpha)$ is found as the ratio of the transmitted sound power $P_{\mathrm{t}}(\theta,\alpha)$ to the incident power $P_{\mathrm{inc}}(\theta,\alpha)$ as in Eq. (3.43). The incident power is defined as:

$$P_{\mathrm{inc}}(\theta,\alpha) = \frac{1}{2}\mathrm{Re}\left[\int_0^{L_{\mathrm{x}}}\int_0^{L_{\mathrm{y}}} p_{\mathrm{inc}}(\theta,\alpha) v^{\mathrm{f},*}_{\mathrm{z,inc}}(\theta,\alpha)\mathrm{d}x\mathrm{d}y\right] \tag{3.66}$$

For a plane wave, the velocity of the incident wave is related to the incident pressure: $v^{\mathrm{f}}_{\mathrm{z,inc}} = p_{\mathrm{inc}}\cos\theta/Z_{\mathrm{c}}$ (cfr. Eq. (3.27)). Substituting this relation and Eqs. (3.58) and (3.63) into Eq. (3.66) results in:

$$P_{\mathrm{inc}}(\theta,\alpha) = \frac{L_{\mathrm{x}}L_{\mathrm{y}}\cos\theta}{8Z_{\mathrm{c}}}\sum_l |p_{\mathrm{inc},l}(\theta,\alpha)|^2. \tag{3.67}$$

The transmitted power $P_{\mathrm{t}}(\theta,\alpha)$ is derived similarly, so that:

$$P_{\mathrm{t}}(\theta,\alpha) = \frac{L_{\mathrm{x}}L_{\mathrm{y}}}{8}\mathrm{Re}\left[\sum_l p_{\mathrm{B},l}(\theta,\alpha) v^{\mathrm{f},*}_{\mathrm{zB},l}(\theta,\alpha)\right]. \tag{3.68}$$

Finally, the diffuse sound transmission is obtained via an integration of the oblique sound transmission over all possible angles of incidence as in Eq. (3.48).

3.4 Hybridization of the Transfer Matrix Method and Statistical Energy Analysis

The approximate modal transfer matrix method, introduced in §3.3.2, is incorporated in the hybrid framework in this section. This results in a novel method, which is referred to as the mTM-SEA approach.

Concepts regarding the hybrid framework were discussed in chapter 2. Airborne and structure-borne sound prediction using the hybrid framework is discussed

in section 2.4. To solve for the sound transmission and the radiated sound power, the direct field response and deterministic dynamic stiffness matrix in generalized coordinates need to be determined. General expressions for these matrices were already given in section 2.5.

This section discusses the choice of the generalized coordinates, the computation of the deterministic and direct field response in terms of these generalized coordinates are elaborated respectively in §3.4.1, §3.4.2 and §3.4.3.

3.4.1 Defining the generalized coordinates

The out-of-plane displacement u_z of the partition wall is approximated using a finite set of N_fun global basis functions $\boldsymbol{\psi}$ (e.g. the in-vacuo modes) and corresponding generalized coordinates $\mathbf{q}$. When the wall is thin, the transverse displacement of the wall at position (x, y) and at frequency ω is independent of the z-coordinate:

$$u_\mathrm{z}(x, y, \omega) \approx \sum_{j=1}^{N_\mathrm{fun}} \psi_j(x, y) q_j(\omega). \tag{3.69}$$

For a layered or thick wall, the decomposition is performed for each of both outer surfaces A and B:

$$u_\mathrm{zA}(x, y, \omega) \approx \sum_{j=1}^{N_\mathrm{fun}} \psi_j(x, y) q_{j\mathrm{A}}(\omega) \quad \text{and} \quad u_\mathrm{zB}(x, y, \omega) \approx \sum_{p=1}^{N_\mathrm{fun}} \psi_j(x, y) q_{j\mathrm{B}}(\omega). \tag{3.70}$$

All generalized response degrees of freedom (DOFs) are collected in a vector $\mathbf{q}(\omega) \in \mathbb{C}^{N_\mathrm{dof} \times 1}$, so that the time-domain response is given by $\mathrm{Re}(\mathbf{q}\mathrm{e}^{\mathrm{i}\omega t})$. Similarly, the corresponding generalized harmonic loads are collected in the load vector $\mathbf{f}(\omega) \in \mathbb{C}^{N_\mathrm{dof} \times 1}$. Note that, when the wall is modelled as thin, $N_\mathrm{dof} = N_\mathrm{fun}$, but when it is thick, $N_\mathrm{dof} = 2N_\mathrm{fun}$.

Similar as in §3.3.2, the chosen basis functions are the sinusoidal basis functions $\boldsymbol{\psi}_\mathrm{sin}$ in Eq. (3.53) in order to approximate the modal behaviour of simply supported, layered building elements in the transfer matrix method. The trace wave number k_tr is taken to be the wavenumber $k_{\mathrm{sin},l}$ (as in Eq. (3.55)), corresponding to the sinusoidal basis function $\boldsymbol{\psi}_{\mathrm{sin},l}$.

The deterministic stiffness matrix $\mathbf{D}_\mathrm{d} \in \mathbb{C}^{N_\mathrm{dof} \times N_\mathrm{dof}}$ and direct field dynamic stiffness matrix $\mathbf{D}_\mathrm{dir}^{(1,2)} \in \mathbb{C}^{N_\mathrm{dof} \times N_\mathrm{dof}}$ are defined in terms of the generalized coordinates $\mathbf{q}$. For a thin plate, the direct field dynamic stiffness matrices in the source and receiver room are equal: $\mathbf{D}^{(1,2)} = \mathbf{D}_\mathrm{dir}$. For a thick wall, the generalized coordinates $\mathbf{q}$ are decoupled into $\mathbf{q}_\mathrm{A}$ and $\mathbf{q}_\mathrm{B}$ so that the direct field

dynamic stiffness matrices for the source and receiver room are found as:

$$\mathbf{D}_{\mathrm{dir}}^{(1)} = \begin{bmatrix} \mathbf{D}_{\mathrm{dir}} & \mathbf{0} \\ \mathbf{0} & \mathbf{0} \end{bmatrix}, \quad \mathbf{D}_{\mathrm{dir}}^{(2)} = \begin{bmatrix} \mathbf{0} & \mathbf{0} \\ \mathbf{0} & \mathbf{D}_{\mathrm{dir}} \end{bmatrix}. \tag{3.71}$$

The elaboration of the deterministic dynamic stiffness matrix $\mathbf{D}_{\mathrm{d}}$ and the direct dynamic stiffness matrix $\mathbf{D}_{\mathrm{dir}}$ are discussed respectively in sections 3.4.2 and 3.4.3.

3.4.2 The deterministic dynamic stiffness matrix

The mechanical impedance matrix $\mathbf{Z}$ is expressed in terms of the generalized coordinates. This is done by substituting Eq. (3.60) into Eq. (3.22):

$$\begin{cases} \sum_l (Z_{11,l} v_{\mathrm{zA},l} + Z_{12,l} v_{\mathrm{zB},l}) \psi_{\mathrm{sin},l}(x,y) = \sum_l p_{\mathrm{A},l} \psi_{\mathrm{sin},l}(x,y), \\ \sum_l (Z_{21,l} v_{\mathrm{zA},l} + Z_{22,l} v_{\mathrm{zB},l}) \psi_{\mathrm{sin},l}(x,y) = \sum_l p_{\mathrm{B},l} \psi_{\mathrm{sin},l}(x,y), \end{cases} \tag{3.72}$$

in which $\mathbf{Z}_l(\omega) = \mathbf{Z}(\omega, k_{\mathrm{sin},l})$. Then, a weighted residual formulation is constructed with weight function $\psi_{\mathrm{sin},m}(x,y)$, so that:

$$\begin{cases} \int_0^{L_{\mathrm{x}}} \int_0^{L_{\mathrm{y}}} \Big[\sum_l (Z_{11,l} v_{\mathrm{zA},l} + Z_{12,l} v_{\mathrm{zB},l}) \psi_{\mathrm{sin},l}(x,y) \\ \qquad - \sum_l p_{\mathrm{A},l} \psi_{\mathrm{sin},l}(x,y) \Big] \psi_{\mathrm{sin},m}(x,y) \mathrm{d}x\mathrm{d}y = 0, \\ \int_0^{L_{\mathrm{x}}} \int_0^{L_{\mathrm{y}}} \Big[\sum_l (Z_{21,l} v_{\mathrm{zA},l} + Z_{22,l} v_{\mathrm{zB},l}) \psi_{\mathrm{sin},l}(x,y) \\ \qquad - \sum_l p_{\mathrm{B},l} \psi_{\mathrm{sin},l}(x,y) \Big] \psi_{\mathrm{sin},m}(x,y) \mathrm{d}x\mathrm{d}y = 0. \end{cases} \tag{3.73}$$

Using the orthogonality property of the sinusoidal basis functions, one has the following relationship for a multilayered system:

$$\begin{bmatrix} Z_{11}(\omega, k_{\mathrm{sin},l}) & Z_{12}(\omega, k_{\mathrm{sin},l}) \\ Z_{21}(\omega, k_{\mathrm{sin},l}) & Z_{22}(\omega, k_{\mathrm{sin},l}) \end{bmatrix} \begin{bmatrix} v_{\mathrm{zA},l}^{\mathrm{f}}(\omega) \\ v_{\mathrm{zB},l}^{\mathrm{f}}(\omega) \end{bmatrix} = \begin{bmatrix} p_{\mathrm{A},l}(\omega) \\ p_{\mathrm{B},l}(\omega) \end{bmatrix}. \tag{3.74}$$

In order to relate the mechanical impedance matrix to the dynamic stiffness matrix of the structure in generalized coordinates, the transformation from the generalized velocities $v_{\mathrm{z},l}$ to the generalized displacements q_l and the transformation from generalized pressures p_l to generalized forces f_l are elaborated:

$$v_{\mathrm{z},l} = \frac{\mathrm{d}q_l}{\mathrm{d}t} = \mathrm{i}\omega q_l, \tag{3.75}$$

$$f_l = \int_0^{L_\mathrm{x}} \int_0^{L_\mathrm{y}} p_l |\psi_{\mathrm{sin},l}(x,y)|^2 \mathrm{d}x\mathrm{d}y = p_l \frac{L_\mathrm{x} L_\mathrm{y}}{4}. \tag{3.76}$$

Inserting equations (3.75) and (3.76) into equation (3.74), returns a formulation for the deterministic dynamic stiffness matrix:

$$\mathbf{D}_{\mathrm{d},l}(\omega) = \frac{\mathrm{i}\omega L_\mathrm{x} L_\mathrm{y}}{4} \begin{bmatrix} Z_{11}(\omega, k_{\mathrm{sin},l}) & Z_{12}(\omega, k_{\mathrm{sin},l}) \\ -Z_{21}(\omega, k_{\mathrm{sin},l}) & -Z_{22}(\omega, k_{\mathrm{sin},l}) \end{bmatrix}. \tag{3.77}$$

Note that a different convention for the pressures in the transfer matrix method and the forces in the hybrid framework, results in a minus sign in the formulation of the impedance matrix as $p_{\mathrm{A},l} = f_{\mathrm{A},l}$ and $p_{\mathrm{B},l} = -f_{\mathrm{B},l}$.

In case of a thin plate, the displacements at both sides of the wall are equal, so that:

$$\frac{\mathrm{i}\omega L_\mathrm{x} L_\mathrm{y}}{4} \begin{bmatrix} Z_{11}(\omega, k_{\mathrm{sin},l}) + Z_{12}(\omega, k_{\mathrm{sin},l}) \\ -Z_{21}(\omega, k_{\mathrm{sin},l}) - Z_{22}(\omega, k_{\mathrm{sin},l}) \end{bmatrix} \begin{bmatrix} \mathbf{q} \end{bmatrix} = \begin{bmatrix} \mathbf{f}_\mathrm{A} \\ \mathbf{f}_\mathrm{B} \end{bmatrix}. \tag{3.78}$$

Using $\mathbf{f} = \mathbf{f}_\mathrm{A} + \mathbf{f}_\mathrm{B}$, the condensed deterministic dynamic stiffness matrix $\mathbf{D}_\mathrm{d}$ for a thin plate is found:

$$D_{\mathrm{d},l} = \frac{\mathrm{i}\omega L_\mathrm{x} L_\mathrm{y}}{4} \left[Z_{11}(\omega, k_{\mathrm{sin},l}) + Z_{12}(\omega, k_{\mathrm{sin},l}) - Z_{21}(\omega, k_{\mathrm{sin},l}) - Z_{22}(\omega, k_{\mathrm{sin},l}) \right]. \tag{3.79}$$

Eqs. (3.77) and (3.79) are exact for a simply supported thin plate, as the mode shapes of such a plate are the imposed sinusoidal basis functions. The computed deterministic dynamic stiffness matrix $\mathbf{D}_\mathrm{d}$ is then equivalent to the analytical expression for the deterministic dynamic stiffness matrix:

$$D_{\mathrm{d},l}(\omega) = \frac{\rho t L_\mathrm{x} L_\mathrm{y}}{4} \left(-\omega^2 + \omega_l^2 (1 + \mathrm{i}\eta) \right), \tag{3.80}$$

with

$$\omega_l = \sqrt{\frac{D}{\rho t}} k_{\mathrm{sin},l}^2, \qquad D := \frac{E t^3}{12(1-\nu^2)}, \tag{3.81}$$

and with ρ, η, t and D respectively the density, the damping loss factor, the thickness and the bending stiffness of the thin plate.

3.4.3 The direct field dynamic stiffness matrix

The acoustic dynamic stiffness matrix $\mathbf{D}_\mathrm{dir}$ should still be determined for a baffled interface that radiates into an acoustic halfspace. The wavelet approach that has been discussed in section 2.5.4, is a general approach to compute the direct field response for an arbitrary displacement field. Because

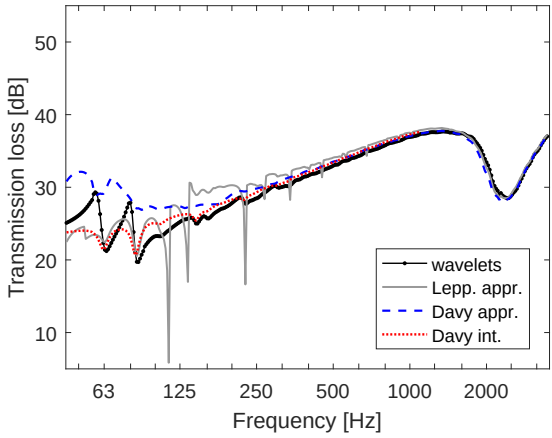

Figure 3.9: The sound transmission loss of a PMMA panel, calculated with the mTM-SEA approach, in which $\mathbf{D}_{\mathrm{dir}}$ is derived from the wavelet approach of Langley, from the approximate asymptotic formulae of Leppington, from the integral formulation of Davy or from the approximate formulae of Davy.

of the imposed sinusoidal basis functions, a faster calculation of the direct field dynamic stiffness matrix is possible, yet at the expense of accuracy. Different approaches for computing the radiation impedance z_l, normalized to the characteristic impedance of the fluid medium Z_{c}, have been presented previously. Leppington et al. [65] simplified the exact quadruple integral, which results from the combination of Eqs. (2.56) and (2.57), to a reduced integral formulation for the radiation efficiency in polar coordinates. The real part of the normalized radiation impedance is then approximated with asymptotic estimates. Automated numerical integration of the Leppington formula with adaptive integration routines faces numerical difficulties however. This problem has been solved by Davy et al. [29], who reformulated the Leppington expression, and extended it to include the imaginary part of the radiation impedance. Besides the numerical evaluation of the exact integral expressions, they have also elaborated approximate formulae for both the real and imaginary part of the radiation impedance. Because these approximations do not require numerical integration, the radiation impedance can be calculated at very low computational cost. The diagonal terms $D_{\mathrm{dir},l}$ are then derived from z_l in the following way:

$$D_{\mathrm{dir},l} = \frac{\mathrm{i}\omega L_{\mathrm{x}} L_{\mathrm{y}}}{4} Z_{\mathrm{c}} z_l. \tag{3.82}$$

In order to investigate the differences between these various approaches to obtain $\mathbf{D}_{\mathrm{dir}}$, the sound transmission loss of a polymethyl methacrylate (PMMA) panel

Time [s]	wavelets	Lepp. appr.	Davy int.	Davy appr.
PMMA panel	230.7	22.2	10752.9	4.7

Table 3.1: Computation time for $\mathbf{D}_{\text{dir}}$ using the wavelet approach of Langley, the approximate asymptotic formulae of Leppington, the integral formulation of Davy and the approximate formulae of Davy.

has been computed using the wavelet approach of Langley [59], the asymptotic estimates of Leppington et al. [65] and the integral formulation and approximate formulae, proposed by Davy et al. [29], embedded within the framework of the mTM-SEA approach. Note that the wavelet approach is normally used in the hybrid FE-SEA method, while the other approaches are normally used in mTMM. The geometric and material properties of the PMMA panel will be detailed in section 3.5.1. Figure 3.9 and table 3.1 show respectively the results in 1/48 octave bands and the computation costs corresponding to the different methods for evaluating $\mathbf{D}_{\text{dir}}$. Only the wavelet approach takes cross-modal coupling, i.e. the interaction between the modes, into account, so the results obtained with this approach are the most accurate ones. There are clear differences with the other approaches until about 500 Hz, which indicates that cross-modal coupling influences the transmission loss up to 500 Hz in the present case. In particular, it can be seen that the approximations of Leppington et al. [59] and Davy et al. [29] and the exact numerical integration of Davy et al. [29] do not capture the anti-resonances at 59.2 Hz and 79.9 Hz. Note that the conventional mTMM cannot take cross-modal coupling into account [90], while this becomes possible within the hybrid mTM-SEA framework presented here. The exact numerical integration approach of Davy et al. [29] agrees best with the wavelet approach. Larger differences are noted for the approximate integration of Davy et al. [29] and for the asymptotic estimates of Leppington [65]. Such differences are indeed expected mainly below coincidence [29]. However, the increase in computational efficiency is very substantial, so application of the approximate expressions of Davy et al. [29] or Leppington et al. [65] render the mTM-SEA approach much more efficient. They are especially useful when frequency band averaging of the STL is considered as the effect of cross-modal coupling will be smoothed out.

In the next section, the predicted, narrow band sound transmission loss is verified in comparison with other prediction tools and validated against experimental data. For the sake of accuracy, the wavelet approach is adopted in the validation examples.

3.5 Validation examples

The proposed mTM-SEA approach is validated for the prediction of the sound transmission loss and the sound power level in respectively section 3.5.1 and section 3.5.2.

3.5.1 Sound transmission loss

In this section, the proposed mTM-SEA approach is validated on wall systems of increasing complexity. The predicted sound transmission loss values are compared against experimental results and alternative prediction results. All calculations were performed on a computer with a 2.70 GHz Intel Core i7 processor and 16 GB RAM.

In all but one example (the double-leaf wall), the experimental results have been obtained at the KU Leuven Laboratory of Acoustics [35]. The rooms in the transmission suite of the KU Leuven Laboratory of Acoustics have a volume of $87\,\mathrm{m}^3$. Wall systems are either tested in a large transmission opening ($3.25\,\mathrm{m} \times 2.95\,\mathrm{m}$) or a small transmission opening ($1.25\,\mathrm{m} \times 1.5\,\mathrm{m}$). The measurements have been performed in accordance with the ISO 10140 standard [50], except that the sound pressure levels were integrated over 1/48-octave bands instead of 1/3-octave bands in order to have a higher frequency resolution. With the exception of the sandwich panel, the damping loss factors of the walls were determined experimentally in 1/3 octave bands from structural reverberation time tests when the test sample was mounted in the vertical transmission opening, in accordance with ISO 10848-1 [49]. The resulting values are listed in Table 3.2. The mentioned total loss factors η include losses by internal damping, sound radiation and vibration absorption at the boundary of the wall. Note that damping by sound radiation is already accounted for in the hybrid framework, meaning that the adopted, measured loss factors are possibly an overestimation. In all simulations, the air density ρ_a and the sound speed c_a in the rooms are taken to be $1.2\,\frac{\mathrm{kg}}{\mathrm{m}^3}$ and $343\,\frac{\mathrm{m}}{\mathrm{s}}$, respectively. To minimize the effect of room damping, ISO-140-3 [48] specifies that the reverberation time should be between 1 and 2 seconds. The reverberation time T is taken to be 1.5 s in all simulations. Mind that if the reverberation times of the rooms stay within the specified range, the influence on simulation results remain limited to 1 dB [35]. Note that in the simulations, the walls are assumed to have simply supported boundary conditions; the accuracy of this assumption was confirmed for a plexiglass panel mounted in the small transmission opening according to the specifications of ISO 10140 [87, 50]. More details concerning the Laboratory can be found in [35].

f [Hz]	50	63	80	100	125	160	200	250
η_{steel} [%]	5.5	5.1	4.4	4.1	3.2	3.1	2.8	2.7
η_{PMMA} [%]	10.4	8.6	6.2	8.8	6.6	6.4	6.0	5.9
η_{brick} [%]	3.8	6.7	7.0	4.6	4.3	3.9	5.3	3.5
$\eta_{\text{glass,6mm}}$ [%]	3.1	2.3	2.6	2.1	1.9	1.7	1.8	2.2
$\eta_{\text{glass,8mm}}$ [%]	3.4	3.5	3.0	2.7	2.7	2.4	2.2	2.3
f [Hz]	315	400	500	630	800	1000	1250	1600
η_{steel} [%]	2.8	3.0	3.2	3.2	3.1	3.2	3.1	3.1
η_{PMMA} [%]	5.8	6.0	5.7	5.7	6.1	6.2	6.5	5.6
η_{brick} [%]	1.7	2.4	2.2	3.2	2.1	1.5	2.3	1.4
$\eta_{\text{glass,6mm}}$ [%]	2.2	2.6	2.8	2.7	2.0	1.6	1.7	1.6
$\eta_{\text{glass,8mm}}$ [%]	2.3	3.0	2.9	2.6	2.0	1.9	1.6	1.7
f [Hz]	2000	2500	3150	4000	5000			
η_{steel} [%]	2.6	2.2	1.9	1.6	1.4			
η_{PMMA} [%]	4.9	5.9	6.0	5.4	4.7			
η_{brick} [%]	1.2	1.4	0.7	0.9	0.8			
$\eta_{\text{glass,6mm}}$ [%]	1.7	1.1	3.4	2.7	2.2			
$\eta_{\text{glass,8mm}}$ [%]	2.0	4.0	4.3	3.4	2.3			

Table 3.2: Measured damping loss factors η for the partition walls tested in the KU Leuven Laboratory of Acoustics.

The hybrid mTM-SEA predictions are also compared to the results of other numerical methods, such as the wave based method (WBM) [35] and the hybrid wave-based transfer matrix method (WB-TMM) [37]. These methods take both the room and wall modes into account. A comparison is made with the hybrid FE-SEA method, which has been discussed earlier in [86, 87]. Numerical results of the conventional TMM and the TMM using a simplified spatial windowing technique (fTMM) [118] as finite size correction are also shown. Comparisons with alternative mTMM approaches (i.e. other than hybrid mTM-SEA) are not performed as these will be influenced mainly by the choice of the method for computing the modal radiation impedance. It was already shown in section 3.4.3 that the wavelet approach for computing the modal radiation impedance, which is employed the conventional hybrid method [86], is the most accurate one.

Steel plate

As a first application, the sound transmission loss of a steel plate is computed with the hybrid mTM-SEA approach outlined above. The steel plate with dimensions $1.25\,\text{m} \times 1.50\,\text{m} \times 0.002\,\text{m}$ has a density $\rho = 7750\,\frac{\text{kg}}{\text{m}^3}$. The Young's

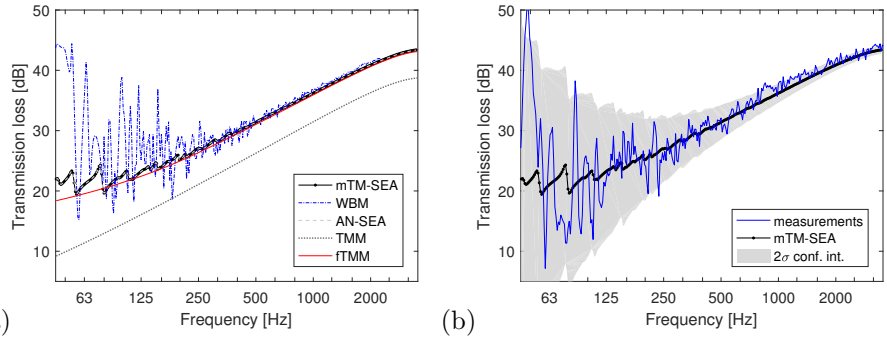

Figure 3.10: The sound transmission loss of a steel plate (a) as predicted with the hybrid mTM-SEA approach, the WBM, the hybrid analytical-SEA approach, the TMM, the fTMM and (b) as measured in the laboratory. The 2σ confidence interval, computed with the hybrid mTM-SEA, is shown in the right figure.

modulus and Poisson's ratio are respectively assumed to be $E = 200\,\text{GPa}$ and $\nu = 0.28$. The experimentally determined damping loss factor of the mounted plate can be found in table 3.2. In the entire frequency range of interest, the steel plate can be considered as thin since the bending wavelength is larger than 6 times the thickness of the plate. Consequently, the analytic dynamic stiffness matrix of a thin plate (Eqs. (3.80)-(3.81)) can also be used in the hybrid deterministic-SEA approach; the resulting model is termed the hybrid analytic-SEA model (AN-SEA).

Fig. 3.10 compares the AN-SEA and mTM-SEA predictions with each other. There is an excellent agreement over the whole frequency range, which confirms that both approaches are equivalent for thin, simply supported plates. The hybrid mTM-SEA results are also compared with the narrow-band (1/48 octave) transmission loss measurements that have been performed at the KU Leuven Acoustics Laboratory and with the results of a WBM model [35]. Below the Schroeder frequency [99] of the rooms, which is around 263 Hz, there is a strong oscillation in the measured sound transmission loss and the results of the WBM, since individual room modes influence these results. Above the Schroeder frequency, the measured transmission loss values are close to the mean mTM-SEA predictions. The 95% confidence interval of the mTM-SEA predictions is also plotted. As explained earlier, the related uncertainty is due to the assumption of a diffuse field in the rooms. This uncertainty is well captured by the mTM-SEA predictions: at low frequencies, where the modal overlap of the rooms is low and their modal behaviour has a large influence on the transmission loss, the mTM-SEA predictions have a large uncertainty, while

they have a small uncertainty at high frequencies, where the modal overlap of the rooms is large.

PMMA panel

The polymethyl methacrylate (PMMA) panel, considered in this second application, has a density $\rho = 1275\ \frac{\text{kg}}{\text{m}^3}$ and dimensions $1.25\,\text{m} \times 1.50\,\text{m} \times 0.015\,\text{m}$. The Young's modulus and Poisson's ratio are respectively taken to be $E =$

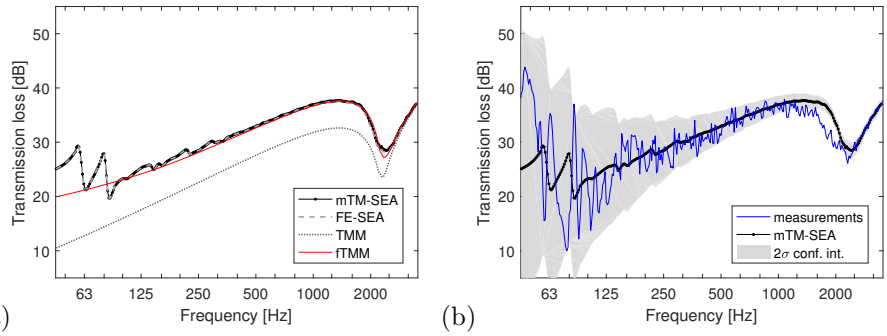

Figure 3.11: The sound transmission loss of a PMMA panel (a) as predicted with the hybrid mTM-SEA approach, the hybrid FE-SEA approach, the conventional TMM, the fTMM, and (b) as measured in the laboratory. The 2σ confidence interval, computed with the hybrid mTM-SEA, is shown in the right figure.

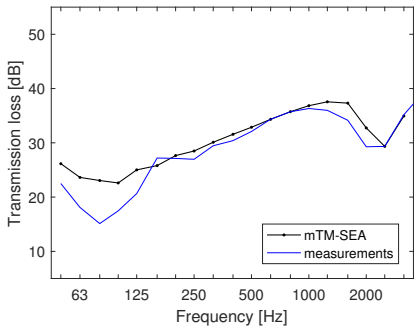

Figure 3.12: The sound transmission loss of a PMMA panel as predicted with the hybrid mTM-SEA approach ($R_\text{w}(C, C_\text{tr}) = 34$(-1,-2) dB) and as measured in the laboratory ($R_\text{w}(C, C_\text{tr}) = 33$(-2,-3) dB) in 1/3 octave bands.

Time [s]	mTM-SEA	FE-SEA	fTMM
PMMA panel	310.1	812.9	59.7
Brick wall	71.5	5651.5	42.9

Table 3.3: Computation time of the mean sound transmission loss for the hybrid mTM-SEA method, the FE-SEA method and the fTMM.

4.5 GPa and $\nu = 0.35$. The experimentally determined damping loss factor of the mounted panel can be found in table 3.2.

Fig. 3.11 compares the hybrid mTM-SEA method with the results of a hybrid FE-SEA model. In the hybrid FE-SEA model, the panel is modelled with 40×40 4-node shell linear elastic finite elements (of the SHELL181 element type in ANSYS), which can be used for analysing thin to moderately thick shell structures. Thickness effects cannot be neglected in this example due to the shear deformation and rotational inertia that occur near the coincidence dip, which is situated around 2500 Hz. The in-plane and out-plane displacements at the boundary are restrained to simulate simply supported boundary conditions. It can be concluded from the results that both hybrid methods agree well. The hybrid mTM-SEA results are also compared against narrow-band (1/48 octave) transmission loss measurements [86, 35]. The predictions of the mTMM-SEA generally agree well with the experimental data, yet the transmission loss below the coincidence dip is slightly overestimated. As argued in [35], this is probably due to the niche which is present in the experiment but not accounted for in the prediction model. The mTM-SEA results and measured STL in 1/3 octave bands are depicted in Fig. 3.12. The single number ratings R_{w} of the mTM-SEA results and the experimental data are respectively 34(-1,-2) dB and 33(-2,-3) dB. The hybrid mTM-SEA predictions are also compared against conventional TMM predictions, which do not account for the finite dimensions nor the modal behaviour of the plate. A conventional TMM model clearly underestimates the sound transmission loss of the plate below coincidence. Above coincidence, the conventional TMM predictions coincide with the hybrid mTMM-SEA predictions, which indicates that at high frequencies, neither the finite dimensions nor the modal behaviour of the plate influence the sound transmission loss. On the other hand, the fTMM agrees well with the mTM-SEA predictions, except at lower frequencies where the modal behaviour of the plate is important.

The computation times for the PMMA panel using different methods are mentioned in table 3.3. The fastest method to calculate the mean sound transmission loss is the fTMM which uses a simplified spatial windowing technique. The hybrid methods are more time consuming, but are at the

same time also capable of computing the variance and the modal behaviour of the plate. As expected, the mTM-SEA method is more efficient than the FE-SEA method.

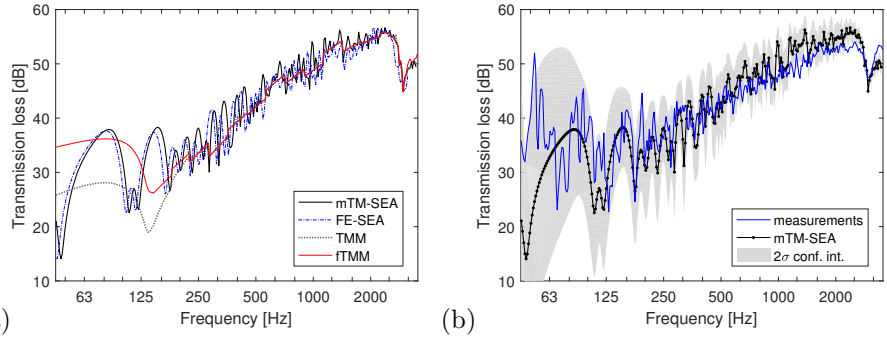

(a) (b)

Figure 3.13: The sound transmission loss of a perforated brick wall (a) as predicted with the hybrid mTM-SEA approach, the hybrid FE-SEA approach, the conventional TMM, the fTMM, and (b) as measured in the laboratory. The 2σ confidence interval, computed with the hybrid mTM-SEA, is shown in the right figure.

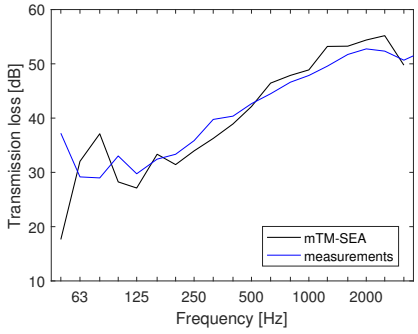

Figure 3.14: The sound transmission loss of a perforated brick wall as predicted with the hybrid mTM-SEA approach ($R_{\mathrm{w}}(C, C_{\mathrm{tr}})$ = 46(-2,-7) dB) and as measured in the laboratory ($R_{\mathrm{w}}(C, C_{\mathrm{tr}})$ = 46(-1,-5) dB) in 1/3 octave bands.

Hollow brick wall

In the third application, a perforated brick wall with dimensions 3.25 m×2.95 m× 0.19 m is considered. The wall is plastered at both sides. The acoustic behaviour of perforated brick walls is complex, given the inhomogeneities at three different scales: the fire clay material, the brick where small cavities are present in the fire clay because of the perforations, and the entire wall where the bricks are held together by mortar layers. When the inhomogeneities are small compared to the wavelength, and when the stiffness is not too different in different directions, the wall can be modelled as homogeneous and isotropic. The thickness effects, however, can not be neglected: not only is shear deformation important, thickness resonances (i.e., Lamb modes) are often observed in the audio frequency range [53]. Following [37], the material properties are based on the surface mass of the wall, the measured coincidence frequency and the measured thickness resonance frequency. The equivalent Young's modulus, Poisson's ratio, density and thickness are then $E = 1825$ MPa, $\nu = 0.2$, $\rho = 613.5\ \frac{\text{kg}}{\text{m}^3}$ and $t = 0.2934$ m, respectively [37]. The experimentally determined damping loss factor of the wall in the transmission opening can be found in table 3.2.

Fig. 3.13 shows the predictions of the hybrid mTM-SEA method, of the conventional TMM, of the fTMM and of a hybrid FE-SEA model. In the hybrid FE-SEA model, the wall is modelled using $100 \times 100 \times 5$ 8-node solid linear elastic finite elements (of the SOLID45 element type in ANSYS). The in-plane and out-plane displacements are only restrained in the middle plane at the boundaries of the wall. The hybrid mTM-SEA and FE-SEA predictions agree well but they are not exactly the same, which is expected since the boundary conditions are slightly different and since the decomposition of the wall displacements using a finite set of sinusoidal basis functions results in an approximation of the true wall behaviour for thick walls. The comparison with the conventional TMM and the fTMM predictions illustrates that the modal behaviour of the wall plays an important role up to about 500 Hz. The low modal density of the wall makes that the coincidence dip, which can be observed in the conventional TMM and the fTMM predictions between 125 Hz and 160 Hz, cannot develop. This is confirmed by the comparison of the hybrid mTM-SEA results with measured values [86, 35]. Again a good agreement is observed between the measurements and the mTM-SEA predictions. Fig. 3.14 shows the STL predictions of the mTM-SEA approach and the measured sound transmission loss in 1/3 octave bands. It can be noticed that the single number ratings are closely related.

The computation times are reported in Table 3.3. The computation cost of the mTM-SEA model is much lower than for the FE-SEA model in this case, because (1) the finite element model of the wall is a 3D solid model, and (2)

the modal density of the wall is low. The fTMM results in only half of the computation time of the mTM-SEA approach, but shows deviations at lower frequencies.

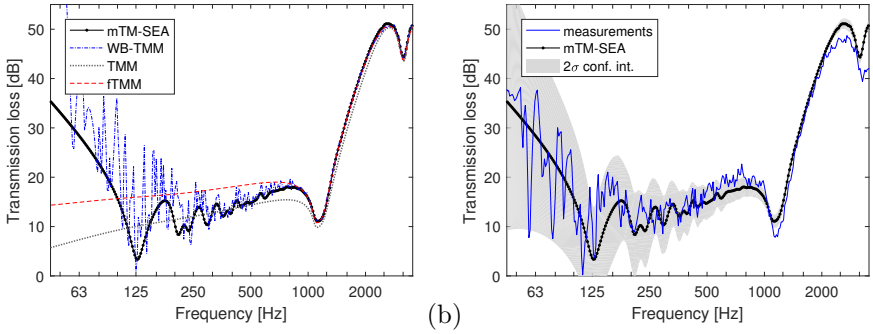

Figure 3.15: The sound transmission loss of a sandwich panel (a) as predicted with the hybrid mTM-SEA approach, the hybrid WB-TMM approach, the conventional TMM, the fTMM and (b) as measured in the laboratory. The 2σ confidence interval, computed with the hybrid mTM-SEA, is shown in the right figure.

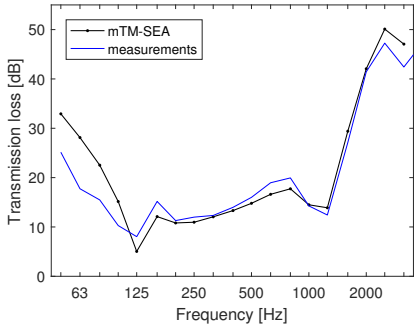

Figure 3.16: The sound transmission loss of a sandwich panel as predicted with the hybrid mTM-SEA approach ($R_{\mathrm{w}}(C, C_{\mathrm{tr}}) = 18$(-1,-3) dB) and as measured in the laboratory ($R_{\mathrm{w}}(C, C_{\mathrm{tr}}) = 19$(-2,-4) dB) in 1/3 octave bands.

Sandwich panel

The fourth system concerns a sandwich panel of dimensions $1.25\,\mathrm{m} \times 1.50\,\mathrm{m} \times 0.150\,\mathrm{m}$. The panel consists of a core of expanded polystyrene (EPS) to which

a 4 mm thick fibreboard panel is glued at each side. In the simulations, the fibreboard has a density $\rho = 765\,\frac{\mathrm{kg}}{\mathrm{m}^3}$. The Young's modulus, Poisson's ratio and loss factor of the fibreboard are taken to be respectively $E = 3.5\,\mathrm{GPa}$, $\nu = 0.46$ and $\eta = 0.01$. The EPS core, which is modelled as a solid layer, has a density $\rho = 20\,\frac{\mathrm{kg}}{\mathrm{m}^3}$ and the Young's modulus, Poisson's ratio and loss factor are assumed to be $E = 12\,\mathrm{MPa}$, $\nu = 0.10$ and $\eta = 0.05$.

Fig. 3.15 compares the hybrid mTM-SEA predictions with conventional TMM and fTMM predictions and predictions using a hybrid WB-TMM model.The hybrid mTM-SEA results are also compared with measured values [35]. All models correctly predict the resonances around 1200 Hz and around 3300 Hz, which are dilatation and thickness resonance dips, respectively [37]. Below the dilatation resonance frequency, the hybrid WB-TMM and mTM-SEA models generally yield slightly higher transmission loss predictions than the conventional TMM model, while the fTMM overestimates the sound transmission loss in comparison to the other models, indicating that not only diffraction effects are important but also resonant sound transmission. Above the dilation resonance frequency, each model predicts the same transmission loss, which indicates that neither the finite size of the wall, nor individual wall resonances, nor individual room resonances influence the transmission loss at these high frequencies.

The dip caused by the fundamental panel resonance, which is at around 125 Hz, and the transition from stiffness to mass behaviour at this point are clearly visible in the hybrid mTM-SEA predictions. Because of the high stiffness to mass ratio, the sound transmission loss of the sandwich panel increases strongly with decreasing frequency below the fundamental mode [41]. The conventional TMM and fTMM do not capture this stiffness effect which explains the large difference. The hybrid predictions also agree well with the measurements, although they slightly underestimate the transmission loss below the dilation resonance. The mTM-SEA results are also compared with the measured STL in 1/3 octave bands in Fig. 3.16.

Double-leaf wall

In this section a double-leaf wall, consisting of a steel plate, a mineral wool core with a flow resistivity of $34\mathrm{kNs/m}^4$ and a laminate plate, is considered and has dimensions 1.3 m × 1.3 m. The different layers are glued onto each other. This validation example was adopted from the literature, as it is known to be a challenging example for modelling poro-elastic layers. The material properties and experimental results in 1/3 octave bands can be found in [119].

The mineral wool is a poro-elastic material. It may be modelled as an equivalent fluid, e.g., using the empirical model of Delany and Bazley [33]. In this model,

the complex characteristic impedance Z_c and the propagation coefficient $\Gamma = \mathrm{i}k$ are derived from the flow resistivity. These complex parameters are then implemented in the transfer matrix of a fluid as explained in [117] and as shown in section 3.2. The advantage is that only the flow resistivity σ and thickness of the porous layer have to be known as input parameters. When using an equivalent fluid model, it is assumed that the frame is motionless and that only a compressional wave will travel through the layer. However, in case of a poro-elastic material with a flexible frame, a more elaborate model may be needed such as the Biot model [10, 11], which has been expanded into the Biot-Allard model [3]. While the Biot-Allard model is physically more accurate, it requires also more input parameters than the Delany-Bazley equivalent fluid model.

The Biot-Allard model and the equivalent fluid model are implemented in the TMM framework, allowing to examine possible differences. Numerical predictions of the TMM, fTMM and mTM-SEA approach using a Biot-Allard model and results of the mTM-SEA approach using an equivalent fluid model are displayed in Fig. 3.17. The band-averaged results of the mTM-SEA approach using both models for the poro-elastic material, are also compared to experimental data. Note that the empirical formulae of Delany and Bazley [33] are only valid in the range $0.01 \leqslant \rho_a f/\sigma \leqslant 1$, which implies that the equivalent fluid model is valid from 315 Hz onwards [117]. This is indicated by the vertical dashed line. A comparison with the experimental results shows that the equivalent model overestimates clearly the sound transmission loss

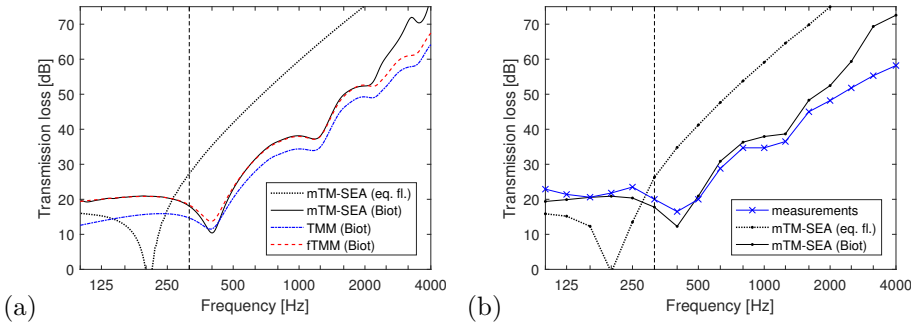

Figure 3.17: The sound transmission loss of a double-leaf wall with poro-elastic material in the cavity (a) as predicted with the hybrid mTM-SEA approach using an equivalent fluid model or a Biot-Allard model, the conventional TMM, the fTMM and (b) as measured in [119]. The results in the right figure are band-averaged to 1/3 octave bands.

in this example, unlike the Biot-Allard model, which is able to capture the behaviour of the mineral wool accurately. There is no visible difference between the mTM-SEA and fTMM results at lower frequencies indicating that for this particular case the modal behaviour does not influence the STL predictions in the considered frequency range. Although the connection between the layers and the poro-elastic layer is modelled similarly, the mTM-SEA results deviate from the fTMM predictions at higher frequencies.

Double glazing

The final structure is a double glazing with dimensions $1.25\,\mathrm{m} \times 1.50\,\mathrm{m} \times 0.026\,\mathrm{m}$ which consists of two glass panels with a thickness of 6 mm and 8 mm, separated by an air cavity of 12 mm. For the simulations, the following material properties for the glass panels are taken: density $\rho = 2500\,\frac{\mathrm{kg}}{\mathrm{m}^3}$, Young's modulus $E = 62\,\mathrm{GPa}$ and Poisson's ratio $\nu = 0.24$. The experimentally determined damping loss factor of both glass panes in mounted condition can be found in table 3.2. The air cavity is taken to be undamped.

In case of double glazing, assuming infinite air layers as in the TMM is not recommended [35, 113]. The air layer stiffness and therefore the mass-spring-mass frequency of the double wall is strongly dependent on the angle of incidence [41]. The lowest mass-air-mass-resonance occurs at normal incidence. An increase of angle of incidence results in an increasing air stiffness, causing the mass-spring-mass resonance dip to be smeared out. This phenomenon does not occur in real finite-sized structures for which the amount of cavity modes is limited. Therefore, the mTM-SEA approach cannot be used for estimating the sound insulation of layered walls containing both solid layers and undamped air layers. However, it is possible to model the glazing using a Rayleigh-Ritz approach, in which the air layer is modelled analytically, as a hard-walled cavity, while the glass panels are modelled as elastic thin plates using the mTMM. The resulting double glazing model is then again coupled to SEA models, describing the neighbouring rooms.

Consider a double glazing which consists of two glass panels with dimensions $L_\mathrm{x} \times L_\mathrm{y}$ and a cavity with dimensions $L_{\mathrm{cav,x}} \times L_{\mathrm{cav,y}} \times L_{\mathrm{cav,z}}$. The different elements of the deterministic dynamic stiffness matrix are deduced by examining the individual components and their interaction. First, the dynamic stiffness matrix of the cavity is discussed in more detail. Because the cavity is an acoustic component, pressure is used as the physical variable instead of displacements which is used for structural components. The pressure in the acoustic cavity can be approximated using a finite set of N_cav basis functions $\boldsymbol{\chi}_\mathrm{cav}$ and corresponding

generalized coordinates b_{cav}:

$$p(x,y,z,\omega) \approx \sum_{n=1}^{N_{\mathrm{cav}}} \chi_{\mathrm{cav},n}(x,y,z) b_{\mathrm{cav},n}(\omega). \tag{3.83}$$

The basis functions $\boldsymbol{\chi}_{\mathrm{cav}}$ are chosen to be the mode shapes of a hard-walled rectangular cavity, normalized to unit acoustic mass:

$$\chi_{\mathrm{cav},n}(x,y,z) = c_{\mathrm{a}} \sqrt{\frac{\epsilon_{\mathrm{x}}\epsilon_{\mathrm{y}}\epsilon_{\mathrm{z}}}{L_{\mathrm{cav,x}}L_{\mathrm{cav,y}}L_{\mathrm{cav,z}}}} \cos\left(\frac{n_{\mathrm{x}}\pi x}{L_{\mathrm{cav,x}}}\right) \cos\left(\frac{n_{\mathrm{y}}\pi y}{L_{\mathrm{cav,y}}}\right) \cos\left(\frac{n_{\mathrm{z}}\pi z}{L_{\mathrm{cav,z}}}\right), \tag{3.84}$$

where n_{x}, n_{y}, n_{z} are the integer number of half wavelengths in the x-, y- and z-directions of mode n. ϵ_{x}, ϵ_{y} and ϵ_{z} are integers equal to one when n_{x}, n_{y} and n_{z} equal zero and equal to two otherwise. The corresponding natural frequencies are:

$$\omega_{\mathrm{cav},n} = c_{\mathrm{a}} \sqrt{\left(\frac{n_{\mathrm{x}}\pi}{L_{\mathrm{cav,x}}}\right)^2 + \left(\frac{n_{\mathrm{y}}\pi}{L_{\mathrm{cav,y}}}\right)^2 + \left(\frac{n_{\mathrm{z}}\pi}{L_{\mathrm{cav,z}}}\right)^2}. \tag{3.85}$$

The mass and stiffness matrices are then easily computed for a hard-walled rectangular room as the generalized coordinates are the modal coordinates of the cavity. Combining the mass and stiffness matrix results in the dynamic stiffness matrix of the cavity:

$$D_{\mathrm{cav},n} = \big(-\omega^2 + \omega_{\mathrm{cav},n}^2 (1 + \mathrm{i}\eta_{\mathrm{cav}}) \big). \tag{3.86}$$

Because the damping in the air cavity is not considered in this example, the damping coefficient η_{cav} is equal to zero. Next, the interaction of the glass panels with the cavity is elaborated. Inserting equations (3.83) and (3.86) into Lagrange's equations of motion yields the following result as the cavity is excited by the movements of two glass panels:

$$\mathbf{D}_{\mathrm{cav}}\mathbf{b}_{\mathrm{cav}} = \mathbf{Q}_{\mathrm{cav},1}\mathbf{q}_{\mathrm{glass1}} + \mathbf{Q}_{\mathrm{cav},2}\mathbf{q}_{\mathrm{glass2}}, \tag{3.87}$$

with

$$\mathbf{Q}_{\mathrm{cav},i,n}\mathbf{q}_{\mathrm{glass}i} = -\int_S \rho_{\mathrm{a}} \ddot{\mathbf{u}}^{\mathrm{T}} \mathbf{n}_S \boldsymbol{\chi}_{\mathrm{cav},n} \mathrm{d}S. \tag{3.88}$$

$\mathbf{b}_{\mathrm{cav}}$ includes the modal degrees of freedom of the hard-walled cavity, while $\mathbf{q}_{\mathrm{glass1}}$ and $\mathbf{q}_{\mathrm{glass2}}$ collect the generalized degrees of freedom of the glass panels. $\mathbf{Q}_{\mathrm{cav},i}$ determines the structure-fluid interaction with n representing the nth row of matrix $\mathbf{Q}_{\mathrm{cav},i}$, $\mathbf{u}$ the surface displacement of the structure and $\mathbf{n}_S$ the normal on the surface pointing towards the acoustic fluid. This expression can be further expanded by substituting equations (3.53) and (3.69) into the displacements $\mathbf{u}$. Consequently, the structure-fluid interaction $\mathbf{Q}_{\mathrm{cav},i}$ can be

constructed by applying the following formula for each mode $n = (n_\mathrm{x}, n_\mathrm{y}, n_\mathrm{z})$ of the cavity with each mode $l = (l_\mathrm{x}, l_\mathrm{y})$ of the imposed basis function on the glass panel i:

$$Q_{\mathrm{cav},i,nl} = \omega^2 c_\mathrm{a} L_{\mathrm{cav,x}}^2 L_{\mathrm{cav,y}}^2 L_\mathrm{x} L_\mathrm{y} l_\mathrm{x} l_\mathrm{y} \sqrt{\frac{\epsilon_\mathrm{x}\epsilon_\mathrm{y}\epsilon_\mathrm{z}}{L_{\mathrm{cav,x}} L_{\mathrm{cav,y}} L_{\mathrm{cav,z}}}} \times \rho_\mathrm{a} \frac{\left(1-(-1)^{l_\mathrm{x}} \cos\left(\frac{n_\mathrm{x}\pi L_\mathrm{x}}{L_{\mathrm{cav,x}}}\right)\right)\left(1-(-1)^{l_\mathrm{y}} \cos\left(\frac{n_\mathrm{y}\pi L_\mathrm{y}}{L_{\mathrm{cav,y}}}\right)\right)}{\pi^2 (L_{\mathrm{cav,x}}^2 l_\mathrm{x}^2 - L_\mathrm{x}^2 n_\mathrm{x}^2)(L_{\mathrm{cav,y}}^2 l_\mathrm{y}^2 - L_\mathrm{y}^2 n_\mathrm{y}^2)}. \quad (3.89)$$

In a similar way, the dynamic stiffness matrix of the glass panels which are treated as thin mTMM layers in this model, and their interaction with the acoustic cavity is shortly summarized. The dynamic stiffness matrix $\mathbf{D}_\mathrm{glass}$ of the glass panels is determined by the mTMM as seen in section 3.4.2. The forces acting on the two glass panels have to be in equilibrium:

$$\mathbf{D}_\mathrm{glass1}\mathbf{q}_\mathrm{glass1} = \mathbf{Q}_{1,\mathrm{cav}}\mathbf{b}_\mathrm{cav} + \mathbf{f}_\mathrm{glass1}, \quad (3.90)$$

$$\mathbf{D}_\mathrm{glass2}\mathbf{q}_\mathrm{glass2} = \mathbf{Q}_{2,\mathrm{cav}}\mathbf{b}_\mathrm{cav} + \mathbf{f}_\mathrm{glass2}. \quad (3.91)$$

The fluid-structure interaction $\mathbf{Q}_{i,\mathrm{cav}}$ can be derived of the structure-fluid interaction $\mathbf{Q}_{\mathrm{cav},i}$.

$$\mathbf{Q}_{i,\mathrm{cav}} = -\frac{\mathbf{Q}_{\mathrm{cav},i}^\mathrm{T}}{\rho_\mathrm{a}}, \quad (3.92)$$

Equation (3.87) can be solved for $\mathbf{b}_\mathrm{cav}$. The obtained expression can then be used in equations (3.90) and (3.91). In this way the equations of motion of the double glazing can be written as $\mathbf{D}_\mathrm{d}\mathbf{q} = \mathbf{f}$, where:

$$\mathbf{D}_\mathrm{d} = \begin{bmatrix} \mathbf{D}_\mathrm{glass1} - \mathbf{Q}_{1,\mathrm{cav}}\mathbf{D}_\mathrm{cav}^{-1}\mathbf{Q}_{\mathrm{cav},1} & -\mathbf{Q}_{1,\mathrm{cav}}\mathbf{D}_\mathrm{cav}^{-1}\mathbf{Q}_{\mathrm{cav},2} \\ -\mathbf{Q}_{2,\mathrm{cav}}\mathbf{D}_\mathrm{cav}^{-1}\mathbf{Q}_{\mathrm{cav},1} & \mathbf{D}_\mathrm{glass2} - \mathbf{Q}_{2,\mathrm{cav}}\mathbf{D}_\mathrm{cav}^{-1}\mathbf{Q}_{\mathrm{cav},2} \end{bmatrix}, \quad (3.93)$$

and

$$\mathbf{q} = \begin{bmatrix} \mathbf{q}_\mathrm{glass1} \\ \mathbf{q}_\mathrm{glass2} \end{bmatrix}, \qquad \mathbf{f} = \begin{bmatrix} \mathbf{f}_\mathrm{glass1} \\ \mathbf{f}_\mathrm{glass2} \end{bmatrix}. \quad (3.94)$$

The obtained deterministic stiffness matrix can now be used within the mTM-SEA approach.

Fig. 3.18 displays the predictions of this modified mTM-SEA method in comparison with results of the conventional TMM and of a WBM model. The results are also compared with measured values [35]. All models agree well, except for the conventional TMM and the fTMM which largely underestimate the sound transmission loss in between the mass-spring-mass resonance (around

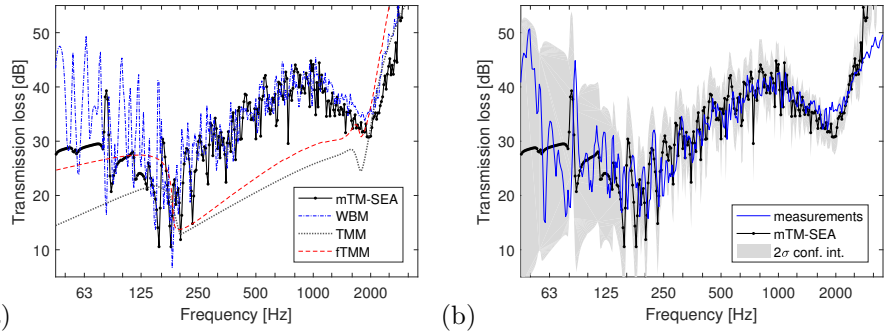

Figure 3.18: The sound transmission loss of a double glazing (a) as predicted with the hybrid mTM-SEA approach, the WBM, the conventional TMM, the fTMM and (b) as measured in the laboratory. The 2σ confidence interval, computed with the hybrid mTM-SEA, is shown in the right figure.

$160 - 200\,\mathrm{Hz}$) and the coincidence dip (around $1600 - 2000\,\mathrm{Hz}$), as the empty cavity was modelled using an infinite fluid layer in these approaches. Note that the WBM accounts for the modal behaviour of the rooms, and it is therefore computationally much more expensive than the hybrid mTM-SEA. Above $2500\,\mathrm{Hz}$ the predictions overestimate the sound transmission loss in comparison with the measurements; this is probably due to the structural coupling between the edges of the glass panels at in the measurement setup, which is not accounted for in the prediction models.

3.5.2 Radiated sound from a mechanically excited plate

In this section, the prediction of impact noise is investigated. As airborne sound is the main focus of this work, only simple numerical examples are considered. First, the structural loading by a harmonic point force is discussed. This impact model is used afterwards to predict the SWL radiated by a glass panel. The resulting displacements are compared to an analytical model. The same impact model is also used to predict the radiated SWL of a concrete floor with floating screed, for which the amplitude of the applied force is taken to be the impact amplitude of a tapping machine. Finally, it is shown how this model could be used to predict the radiated sound power, due to rain noise.

Point force

A harmonic point force $F(t,x,y) = \mathrm{Re}\big[F(x,y)\mathrm{e}^{\mathrm{i}\omega t}\big]$ with amplitude F_0 is applied at location $(x_\mathrm{P}, y_\mathrm{P})$ in A. The force is then $F(x,y) = F_0\delta(x-x_\mathrm{P})\delta(y-y_\mathrm{P})$, so that the generalized force $\mathbf{f}_\mathrm{A}$ becomes:

$$f_{\mathrm{A},l} = \int_0^{L_\mathrm{y}}\int_0^{L_\mathrm{x}} F_0\delta(x-x_\mathrm{P})\delta(y-y_\mathrm{P})\psi_{\mathrm{sin},l}(x,y)\mathrm{d}x\mathrm{d}y, \tag{3.95}$$

$$= F_0\psi_{\mathrm{sin},l}(x_\mathrm{P}, y_\mathrm{P}). \tag{3.96}$$

The generalized forces are found as $\mathbf{f} = [\mathbf{f}_\mathrm{A}^\mathrm{T}\ \mathbf{0}^\mathrm{T}]^\mathrm{T}$.

Impact noise has already been discussed in section 2.4.2. Using the generalized forces, the generalized displacement field can be derived from the deterministic dynamic stiffness matrix, obtained in Eq. (3.77). The radiated sound power follows from (2.44) using the found displacement field and the direct field response of the receiver room. Note that all equations are fully deterministic, as only the direct field response of the receiving room needs to be computed. Because the receiver room is not modelled stochastically, the adopted methodology is referred to as the mTMM approach. In comparison with the method, discussed in section 3.3.2, the adopted mTMM approach that is verified here, accounts for cross-modal coupling and allows for the computation of the variance of the radiated SWL [88].

Glass panel Consider a simply supported glass panel with thickness $t = 0.006$ m and with dimensions $L_\mathrm{x} = 1.25$ m $\times$ $L_\mathrm{y} = 1.50$ m. The Young's modulus E, density ρ, shear modulus G and damping loss factor η are respectively chosen to be 63 GPa, 2500 kg/m^3, 2.5 GPa and 5%. The harmonic point force with unit amplitude $F_0 = 1$ N is located at (0.5m,1m).

The predicted out-of-plane displacement u_z in a selected point $(x_\mathrm{S}, y_\mathrm{S})$ can be computed analytically, as follows [41]:

$$u_\mathrm{z}(x_\mathrm{S}, y_\mathrm{S}) = \sum_{l=1}^{N_\mathrm{fun}} \frac{4F_0}{L_\mathrm{x}L_\mathrm{y}\rho t}\cdot\frac{\psi_{\mathrm{sin},l}(x_\mathrm{P}, y_\mathrm{P})\psi_{\mathrm{sin},l}(x_\mathrm{S}, y_\mathrm{S})}{(\omega_l^2-\omega^2)}. \tag{3.97}$$

Figures 3.19(a) and 3.19(b) show respectively the absolute value of the out-of-plane displacement at $(x_\mathrm{S}, y_\mathrm{S}) = (0.25\mathrm{m}, 0.25\mathrm{m})$ and the radiated SWL, caused by the harmonic point force. As the glass panel is considered to be a thin plate, the results of the analytical and mTMM approach are exactly the same. The first panel resonance of the glass panel, which appears at 15.3 Hz is clearly

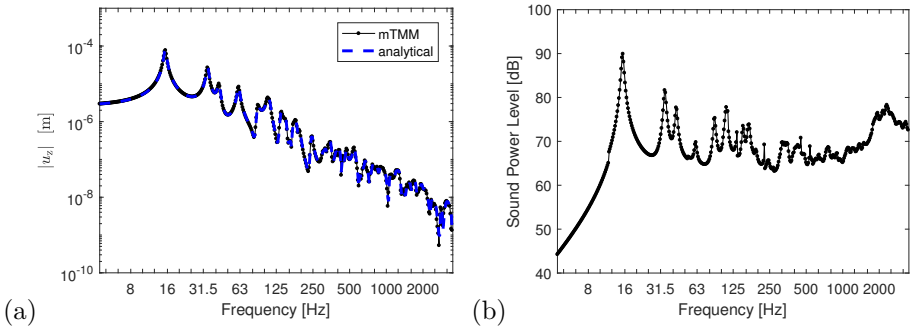

Figure 3.19: (a) The absolute value of the out-of-plane displacement $|u_z|$ in a point (0.25m,0.25m) of a glass panel due to a harmonic point force with unit amplitude at location (0.5m,1m), predicted by the mTMM approach and an analytical method. The corresponding SWL, predicted by the mTMM approach is plotted in (b).

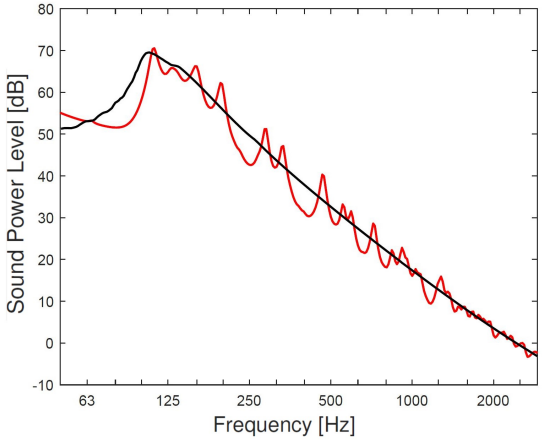

Figure 3.20: The radiated SWL of a concrete floor with floating screed due to a tapping machine, predicted by the TMM (black) and the mTMM (red) [114].

visible in Figs. 3.19(a) and 3.19(b). Coincidence causes a rise in the SWL results at approximately 2020 Hz.

Concrete floor with floating screed This floor element is a layered system, consisting of a concrete floor with a thickness of 0.20 m, a 0.005 m thick

polyethylene foam as a resilient interlayer and a lightweight concrete finishing with a thickness of 0.05 m on top. The material parameters of the concrete floor, the polyethylene interlayer and the screed can be found in [114]. The floor system has dimensions 4.15 m × 5.10 m. F_0 is taken to be constant and continuous over the considered frequency range. The force amplitude is 8.86Ñ which corresponds to the impact amplitude of a tapping machine [115, 114]. For a more elaborate impact force model the reader is referred to [124].

The SWL predicted using the mTMM approach and the TMM is shown in Fig. 3.20. The peak in the SWL predictions at approximately 120 Hz corresponds to the mass-spring-mass resonance of the concrete floor with floating screed. Above this frequency, the screed is decoupled by the resilient interlayer from the concrete floor, resulting in a decrease of the radiated sound power. At higher frequencies, the results of the TMM align with the results of the mTMM, when the modal overlap of the floor system is high enough.

It is emphasized that the screed is decoupled along the boundaries from surrounding building elements in building practice. Therefore, the model of simply supported floor system is not entirely accurate. In reality, the concrete floor will be simply supported, while the screed should be considered as unbaffled [47]. The current implementation of the mTMM is however limited to layered simply supported systems and is not applicable for building elements, from which the boundary conditions can differ through the thickness of the system.

Rain noise

A simplified model of the mTMM approach developed in this thesis was used in research in collaboration with the University of Auckland [96]. This paper presents the development of state-of-the-art theoretical models for rain noise prediction. Several impact models to compute the force due to a water droplet impacting on an inclined flat surface, are compared and the best impact force models are then used to obtain the sound intensity level L_{I}. The sound intensity L_{I} is obtained from the SWL as follows:

$$L_{\mathrm{I}} = L_{\mathrm{P}} - 10 \log \left(\frac{S_{\mathrm{e}}}{S_{\mathrm{ref}}} \right), \tag{3.98}$$

where S_{e} is the excitation area of the test sample and $S_{\mathrm{ref}} = 1\ \mathrm{m}^2$. To obtain the SWL, three methods were introduced and referred to as 'Radiation model 1', 'Radiation model 2' and 'Radiation model 3'. The first model is based on [29], and does not include modal effects. The second and third method do incorporate modal behaviour. However, 'Radiation model 2' is limited to thin plates, while 'Radiation model 3' can easily be expanded to the mTMM

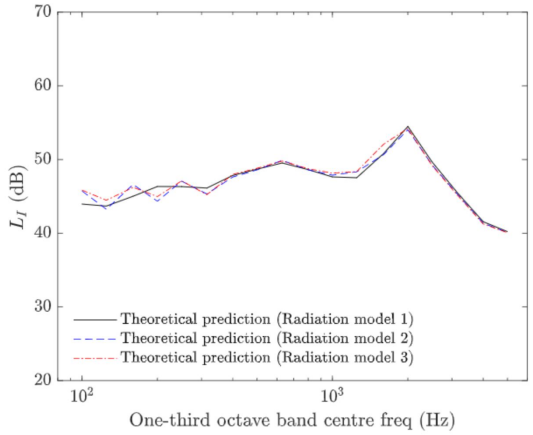

Figure 3.21: The sound intensity level L_{I}, due to rain noise on a glass panel inclined at 30°, predicted by Radiation model 1, Radiation model 2 and Radiation model 3 in 1/3-octave bands [96].

approach, by replacing the analytical model of the deterministic dynamic stiffness matrix by the deterministic dynamic stiffness matrix as defined in Eq. (3.77) or Eq. (3.79).

The impact force in 'Radiation model 3' is modelled deterministically. As droplets are generated in rain tests by holes in a tray lifted above the test sample, it is assumed that for each hole in the tray a sequence of identical droplets impact on the test sample in one particular point and with a constant period T_1 between impacts. The impact force at angular frequency $\omega_n = 2\pi n/T_1$ due to a train of droplets at one location is then $F^n(\omega)\mathrm{e}^{\mathrm{i}\omega_n t+\mathrm{i}\beta}$, with $F^n = 2\pi F_1(\omega_n)/T_1$ and with $F_1(\omega_n)$ defined in [96, Eq. (11)]. The computed forces are then applied as harmonic point forces at N randomly selected positions with random phase β to ensure that the forces are uncorrelated. The influence of the randomly chosen positions and phases is examined using the Monte Carlo method. This involved calculating the radiated sound power for fifty different realisations with different force locations and phases. These results were used to compute the mean sound power of the realisations.

The sound intensity level, due to rain noise on a glass panel inclined at 30° is now considered. The glass panel with dimensions 1.25 m × 1.50 m has a thickness of 0.006 m. The Young's modulus E, Poisson coefficient ν and density ρ are taken to be 70 GPa, 0.24 and 2500 kg/m^3. The measured loss factor η is found in [96, Fig. 13].

Fig. 3.21 shows the sound intensity levels in 1/3-octave bands, predicted by the three Radiation models. It is noticed that Radiation models 2 and 3 oscillate more at lower frequencies than Radiation model 1, as modal behaviour is only accounted for in models 2 and 3. Coincidence is clearly visible at approximately 2000 Hz, causing a peak in the predicted sound intensity levels. A good agreement between the predictions of all three models in 1/3-octave bands can be observed.

3.6 Conclusions

In this chapter, the theory of the transfer matrix method has been summarized first. Layered systems can be modelled efficiently by describing the sound propagation through a layer and between layers analytically with transfer and interface matrices in function of frequency and trace wavenumber. Combining the transfer and interface matrices results in the global transfer matrix and eventually the mechanical impedance matrix, which relates pressures and velocities at both sides of the layered system. The layers are assumed to be flat, of infinite lateral extent and homogeneous. It is shown how the sound transmission loss can be obtained using this conventional transfer matrix method.

In the frequency range of interest, finite size effects are however important. Two finite size corrections were discussed, so that finite size can be approximately accounted for: (1) a spatial windowing technique can be applied to account for diffraction effects. In summary, it means that only the velocity field of the structure within a screen with the same dimensions as that of the finite system is accounted for in the sound radiation computation. The applied transfer matrix method with finite size correction is still a wave approach. (2) due to the boundaries of the building element, standing waves at discrete frequencies arise in the building element. These resonances cause oscillations in the sound transmission loss prediction. Modal behaviour is approximately accounted for within the approximate modal transfer matrix method. The displacements at the surfaces of the test sample are decomposed using a set of sinusoidal basis functions, which satisfy the simply supported boundary conditions. The corresponding mechanical impedance matrices are obtained by imposing the sinusoidal wave numbers as trace wavenumbers.

Then, the hybridization between the approximate modal based transfer matrix method and statistical energy analysis is elaborated. The displacements are decoupled at both sides of the layered system and converted into generalized coordinates corresponding to a set of sinusoidal basis functions. The deterministic dynamic stiffness matrix of the wall or floor system in terms

of these generalized coordinates is deduced from the mechanical impedance matrix in function of frequency and the wavenumbers of these sinusoidal basis functions. Due to the sinusoidal functions, multiple methods to determine the direct field response are possible. As the combination of the wavelet approach with the hybrid framework allows to include cross-modal coupling, the wavelet approach is used further on in the validation examples.

Afterwards, the predicted sound transmission loss is verified with other prediction tools and experimental data for structures of increasing complexity: a steel plate, a PMMA panel, a hollow brick wall, a sandwich panel, a double-leaf wall and double glazing. It was shown that the novel mTM-SEA accounts for the modal behaviour of the test sample: the stiffness to mass transition and (anti-)resonance dips are clearly visible in the sound transmission loss predictions and a good correspondence between the mTM-SEA predictions and the results of a hybrid framework involving a full finite element method is obtained. The computation times illustrate that replacing the finite element model by the semi-analytical transfer matrix method results in an increase in computational efficiency in the considered validation examples. So when the building element is simple enough (i.e. flat, rectangular and with isotropic layers), using the mTM-SEA approach instead of the FE-SEA method is worth considering. At lower frequencies, the measured sound transmission loss oscillates more heavily than the sound transmission loss predicted by the mTM-SEA approach, due to the modal behaviour of the rooms which is not accounted for in the predictions. However, it is possible to obtain the variance, inherent to the diffuse field assumption in the rooms. The 95% confidence interval shows the possible range in which the sound transmission loss could oscillate when the reverberant field would not be diffuse. This uncertainty is large at lower frequencies when the modal overlap of the rooms is low and their modal behaviour has a large influence on the rooms.

Finally, the radiated sound from a mechanically excited glass panel and a concrete floor with floating screed is discussed. The impact model of a point force is also used to predict rain noise.

Chapter 4

Periodic building elements

4.1 Introduction

(a)  (b) 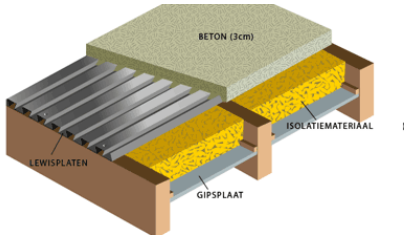

Figure 4.1: Examples of periodic building elements: (a) a gypsum board wall [1] and (b) a composite metal flooring system [121].

Most building elements, such as the ones displayed in Figs. 1.5 and 4.1, exhibit a periodic lay out. Periodic structure theory can therefore be employed to reduce the finite element model of the entire structure to the finite element of the periodic unit cell. Periodic boundary conditions are imposed onto the model of the unit cell in the form of phase lags across the unit cell in both directions. Solving the eigenvalue problem results in several travelling waves with corresponding eigenfrequencies for one particular phase lag combination [71, 72]. Only out-of-plane displacements contribute to sound transmission, so that in-plane waves do not need to be accounted for. Simulating modal behaviour

is challenging within this approach, as periodic finite element modelling is in essence a wave approach.

In this chapter, periodic structure theory is invoked to compute the deterministic and direct field dynamic stiffness matrix, while modal behaviour is inherently accounted for. Section 4.2 introduces periodic structure theory and a general approach to compute the sound transmission loss for infinite periodic panels. Sections 4.3 and 4.4 consider the integration of periodic finite element modelling into the hybrid framework with focus on modal behaviour. It is shown in section 4.3 how the modal properties of a finite-sized wall of floor can be obtained from periodic structure theory. These properties are then used in section 4.4 to determine the deterministic and direct field dynamic stiffness matrix in terms of the modal coordinates. Section 4.5 discusses practicalities of the implementation of the methodology. In section 4.6 the hybrid method is validated for two cross laminated timber panels and two rib-stiffened panels by comparing the predicted sound transmission loss with the results of a hybrid FE-SEA approach and with experimental data. Section 4.7 discusses an alternative approach in which the displacements of the periodic wall or floor are projected onto sinusoidal basis functions. Finally, the conclusions are to be found in section 4.8.

4.2 General description of periodic structure theory

4.2.1 Equations of motion of the periodic unit cell

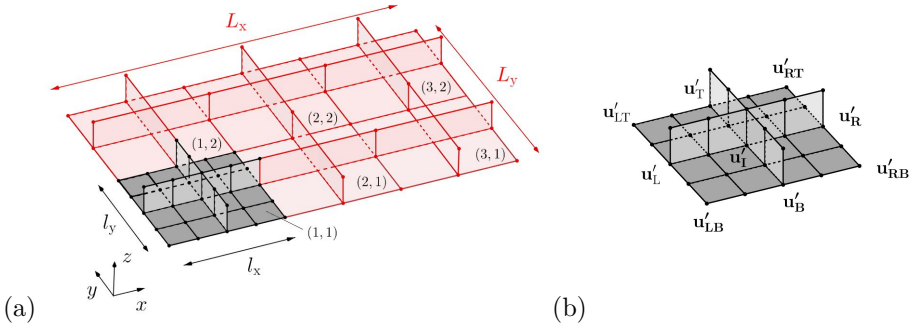

Figure 4.2: (a) A periodic structure with $N_x = 3$ and $N_y = 2$. The selected periodic unit cell is cell (1,1) in the lower left corner of the global structure. The edge and corner degrees of freedom of the periodic unit cell are indicated in (b).

A rectangular wall of size $L_\mathrm{x} \times L_\mathrm{y}$ is considered. The wall is geometrically periodic, so a unit cell of the structure is repeated N_x and N_y times in the x- and y-directions, respectively, as illustrated in Fig. 4.2(a). Consequently, the size of the unit cell is $l_\mathrm{x} \times l_\mathrm{y}$, where $l_\mathrm{x} = L_\mathrm{x}/N_\mathrm{x}$ and $l_\mathrm{y} = L_\mathrm{y}/N_\mathrm{y}$.

A numerical model for the dynamic response of the unit cell is constructed. As an example, a finite element model is considered. The related nodal displacement degrees of freedom, internal nodal forces and external nodal forces are denoted with $\mathbf{u}'$, $\mathbf{f}'$ and $\mathbf{e}'$, and the mass and stiffness matrices with $\mathbf{M}'$ and $\mathbf{K}'$. If spatially uniform damping is assumed with loss factor η, then the equations of motion of the unit cell read

$$\left(-\mathbf{M}'\omega^2 + (1+\mathrm{i}\eta)\,\mathbf{K}'\right)\mathbf{u}' = \mathbf{f}' + \mathbf{e}'. \tag{4.1}$$

When considering plane wave propagation across a single unit cell, cell-wise phase shifts $\exp(-\mathrm{i}\epsilon_\mathrm{x})$ and $\exp(-\mathrm{i}\epsilon_\mathrm{y})$ are introduced in the x- and y-directions, respectively [14, 58, 75]. This can be practically implemented by collecting the displacements $\mathbf{u}'$ associated with the left (subscript L), right (subscript R), top (subscript T) and bottom (subscript B) faces, the corner edges (subscripts LB, RB, LT and RT), and the interior (subscript I) of the cell (cfr. Fig. 4.2(b)), such that

$$\underbrace{\begin{bmatrix} \mathbf{u}'_\mathrm{I} \\ \mathbf{u}'_\mathrm{B} \\ \mathbf{u}'_\mathrm{T} \\ \mathbf{u}'_\mathrm{L} \\ \mathbf{u}'_\mathrm{R} \\ \mathbf{u}'_\mathrm{LB} \\ \mathbf{u}'_\mathrm{RB} \\ \mathbf{u}'_\mathrm{LT} \\ \mathbf{u}'_\mathrm{RT} \end{bmatrix}}_{\mathbf{u}'} = \underbrace{\begin{bmatrix} \mathbf{I} & \mathbf{0} & \mathbf{0} & \mathbf{0} \\ \mathbf{0} & \mathbf{I} & \mathbf{0} & \mathbf{0} \\ \mathbf{0} & \mathbf{I}\mathrm{e}^{-\mathrm{i}\epsilon_\mathrm{y}} & \mathbf{0} & \mathbf{0} \\ \mathbf{0} & \mathbf{0} & \mathbf{I} & \mathbf{0} \\ \mathbf{0} & \mathbf{0} & \mathbf{I}\mathrm{e}^{-\mathrm{i}\epsilon_\mathrm{x}} & \mathbf{0} \\ \mathbf{0} & \mathbf{0} & \mathbf{0} & \mathbf{I} \\ \mathbf{0} & \mathbf{0} & \mathbf{0} & \mathbf{I}\mathrm{e}^{-\mathrm{i}\epsilon_\mathrm{x}} \\ \mathbf{0} & \mathbf{0} & \mathbf{0} & \mathbf{I}\mathrm{e}^{-\mathrm{i}\epsilon_\mathrm{y}} \\ \mathbf{0} & \mathbf{0} & \mathbf{0} & \mathbf{I}\mathrm{e}^{-\mathrm{i}\epsilon_\mathrm{x}-\mathrm{i}\epsilon_\mathrm{y}} \end{bmatrix}}_{\mathbf{R}(\epsilon_\mathrm{x},\epsilon_\mathrm{y})} \underbrace{\begin{bmatrix} \mathbf{u}'_\mathrm{I} \\ \mathbf{u}'_\mathrm{B} \\ \mathbf{u}'_\mathrm{L} \\ \mathbf{u}'_\mathrm{LB} \end{bmatrix}}_{\mathbf{u}'_\mathrm{R}}. \tag{4.2}$$

The matrix $\mathbf{R}$ relates the full set of displacement degrees of freedom of the unit cell $\mathbf{u}'$ to a reduced set $\mathbf{u}'_\mathrm{R}$. The equations of motion of the periodic unit cell are rewritten into:

$$\left(-\mathbf{M}'_\mathrm{R}\omega^2 + (1+\mathrm{i}\eta)\mathbf{K}'_\mathrm{R}\right)\mathbf{u}'_\mathrm{R} = \mathbf{R}^\mathrm{H}\mathbf{f}' + \mathbf{R}^\mathrm{H}\mathbf{e}', \tag{4.3}$$

where

$$\mathbf{M}'_\mathrm{R}(\epsilon_\mathrm{x},\epsilon_\mathrm{y}) := \mathbf{R}^\mathrm{H}\mathbf{M}'\mathbf{R} \quad \text{and} \quad \mathbf{K}'_\mathrm{R}(\epsilon_\mathrm{x},\epsilon_\mathrm{y}) := \mathbf{R}^\mathrm{H}\mathbf{K}'\mathbf{R}. \tag{4.4}$$

Because force equilibrium of the internal nodal forces results in [58]:

$$\mathbf{R}^\mathrm{H}\mathbf{f}' = \mathbf{0}, \tag{4.5}$$

the equations of motion of the periodic unit cell in Eq. (4.3) can be further simplified:

$$\big(-\mathbf{M}'_{\mathrm{R}}\omega^2 + (1+\mathrm{i}\eta)\mathbf{K}'_{\mathrm{R}}\big)\mathbf{u}'_{\mathrm{R}} = \mathbf{R}^{\mathrm{H}}\mathbf{e}'. \tag{4.6}$$

4.2.2 Airborne sound prediction

A general method to compute the sound transmission through infinite panels using the dynamic stiffness matrix of the periodic unit cell is described in [129, 131] and is briefly summarized in this section.

In case of oblique sound transmission, an incident pressure field is created at the fluid-structure interface by an incoming wave with unit amplitude, incidence angle θ and direction α (cfr. Fig. 3.8):

$$p_{\mathrm{inc}}(x,y) = \mathrm{e}^{-\mathrm{i}k_{\mathrm{inc,x}}x}\mathrm{e}^{-\mathrm{i}k_{\mathrm{inc,y}}y}, \tag{4.7}$$

where

$$k_{\mathrm{inc,x}} = k_{\mathrm{a}}\sin\theta\cos\alpha \quad \text{and} \quad k_{\mathrm{inc,y}} = k_{\mathrm{a}}\sin\theta\sin\alpha. \tag{4.8}$$

The motion of the panel excited by plane wave excitation creates a reflected and transmitted wave:

$$p_{\mathrm{r}}(x,y) = P_{\mathrm{r}}\mathrm{e}^{-\mathrm{i}k_{\mathrm{inc,x}}x}\mathrm{e}^{-\mathrm{i}k_{\mathrm{inc,y}}y}, \tag{4.9}$$

$$p_{\mathrm{t}}(x,y) = P_{\mathrm{t}}\mathrm{e}^{-\mathrm{i}k_{\mathrm{inc,x}}x}\mathrm{e}^{-\mathrm{i}k_{\mathrm{inc,y}}y}, \tag{4.10}$$

with P_{r} and P_{t} the complex pressure amplitude of respectively the reflected and transmitted wave. If the displacement field on the interface at the left and right side of the panel (in A and B as illustrated in Fig. 3.3) are respectively described by $u_1(x,y) = u_1 \cdot \mathrm{e}^{-\mathrm{i}k_{\mathrm{inc,x}}x}\mathrm{e}^{-\mathrm{i}k_{\mathrm{inc,y}}y}$ and $u_2(x,y) = u_2 \cdot \mathrm{e}^{-\mathrm{i}k_{\mathrm{inc,x}}x}\mathrm{e}^{-\mathrm{i}k_{\mathrm{inc,y}}y}$, then the pressures and displacements at both sides of the structure relate for a plane wave as:

$$1 - P_{\mathrm{r}} = D_1^{\mathrm{f}}u_1, \quad D_1^{\mathrm{f}} = \frac{-\mathrm{i}\omega Z_{\mathrm{c}}}{\cos\theta}, \tag{4.11}$$

$$P_{\mathrm{t}} = D_2^{\mathrm{f}}u_2, \quad D_2^{\mathrm{f}} = \frac{\mathrm{i}\omega Z_{\mathrm{c}}}{\cos\theta}. \tag{4.12}$$

Note that Eq. (4.12) is equivalent to Eq. (3.28).

Next, the periodic unit cell is modelled using a FE discretization, as in section 4.2.1. The acoustic loading is converted into equivalent external nodal loads on the surface DOFs such that:

$$\mathbf{e}' = 2\mathbf{e}_0 - D_1^{\mathrm{f}}\mathbf{\Gamma}_1\mathbf{u}' - D_2^{\mathrm{f}}\mathbf{\Gamma}_2\mathbf{u}', \tag{4.13}$$

in which the elements of $\mathbf{e}_0$, $\mathbf{\Gamma}_1$ and $\mathbf{\Gamma}_2$ represent the equivalent nodal forces. Only elements corresponding to out-of-plane displacements at the fluid-structure interface are non-zero. The calculation of $\mathbf{e}_0$, $\mathbf{\Gamma}_1$ and $\mathbf{\Gamma}_2$ can be found in [129].

Defining the fluid loading as $\mathbf{F} = D_1^{\mathrm{f}}\mathbf{\Gamma}_1\mathbf{u}' + D_2^{\mathrm{f}}\mathbf{\Gamma}_2\mathbf{u}'$, the equations of motion of the unit cell in Eq. (4.1) are rewritten into:

$$\left(-\mathbf{M}'\omega^2 + (1+\mathrm{i}\eta)\,\mathbf{K}' + \mathbf{F}\right)\mathbf{u}' = \mathbf{f}' + 2\mathbf{e}_0. \tag{4.14}$$

Imposing the phase shifts $\epsilon_{\mathrm{x}} = k_{\mathrm{inc,x}}l_{\mathrm{x}}$ and $\epsilon_{\mathrm{y}} = k_{\mathrm{inc,y}}l_{\mathrm{y}}$ onto the unit cell, gives:

$$\left(-\mathbf{M}'_{\mathrm{R}}\omega^2 + (1+\mathrm{i}\eta)\mathbf{K}'_{\mathrm{R}} + \mathbf{F}_{\mathrm{R}}\right)\mathbf{u}'_{\mathrm{R}} = 2\mathbf{R}^{\mathrm{H}}\mathbf{e}_0, \tag{4.15}$$

where $\mathbf{F}_{\mathrm{R}} = \mathbf{R}^{\mathrm{H}}\mathbf{F}\mathbf{R}$ and $\mathbf{M}'_{\mathrm{R}}$, $\mathbf{K}'_{\mathrm{R}}$, $\mathbf{u}'_{\mathrm{R}}$ and $\mathbf{R}$ are defined in Eqs. (4.2) and (4.4). Eq. (4.15) is solved for the structural response of the structure. From this, the complex pressure amplitude of the transmitted wave is derived using Eq. (4.12).

Finally, the oblique sound transmission $\tau_{12}(\theta,\alpha)$ results from the complex pressure amplitude of the transmitted P_{t} and the complex pressure amplitude of the incident wave P_{inc}:

$$\tau_{12}(\theta,\alpha) = |T(\theta,\alpha)|^2, \quad \text{with} \quad T(\theta,\alpha) = \frac{P_{\mathrm{t}}}{P_{\mathrm{inc}}}, \tag{4.16}$$

The diffuse sound transmission is obtained using Eq. (3.48).

4.3 Predicting the modal properties of a finite wall or floor using periodic structure theory

The generalized displacement degrees of freedom $\mathbf{q}$ are taken to be the modal displacement coordinates of the periodic wall in correspondence with chapter 2. In this section, it will be investigated how the related modal properties can be computed for a periodic structure with a unit cell of arbitrary geometrical complexity. The considered unit cell in the analysis below refers to unit cell (1,1) as indicated in Fig. 4.2(a).

For a given set of phase shifts or phase constants $(\epsilon_{\mathrm{x}}, \epsilon_{\mathrm{y}}) \in [-\pi,\pi] \times [-\pi,\pi]$, free undamped wave propagation across the unit cell is obtained by taking both $\mathbf{e}'$ and η in Eq. (4.6) to be zero. This leads to the following eigenvalue problem:

$$\mathbf{K}'_{\mathrm{R}}(\epsilon_{\mathrm{x}},\epsilon_{\mathrm{y}})\mathbf{u}'_{\mathrm{R}} = \omega^2\mathbf{M}'_{\mathrm{R}}(\epsilon_{\mathrm{x}},\epsilon_{\mathrm{y}})\mathbf{u}'_{\mathrm{R}}. \tag{4.17}$$

The corresponding eigenvalues and eigenvectors represent the squared angular frequencies $\omega_j^2(\epsilon_{\mathrm{x}},\epsilon_{\mathrm{y}})$ and corresponding displacement shapes $\mathbf{u}'_j(\epsilon_{\mathrm{x}},\epsilon_{\mathrm{y}})$ of free

undamped plane wave propagation for the specified phase shifts. The function $\omega_j^2(\epsilon_\mathrm{x}, \epsilon_\mathrm{y})$ can be plotted in the phase domain. Each surface represents a phase constant surface. This is illustrated by Fig. 4.3, which shows the phase constant surfaces of the bending waves of a thin plate up to 1000 Hz for $(\epsilon_\mathrm{x}, \epsilon_\mathrm{y}) \in [0, \pi] \times [0, \pi]$.

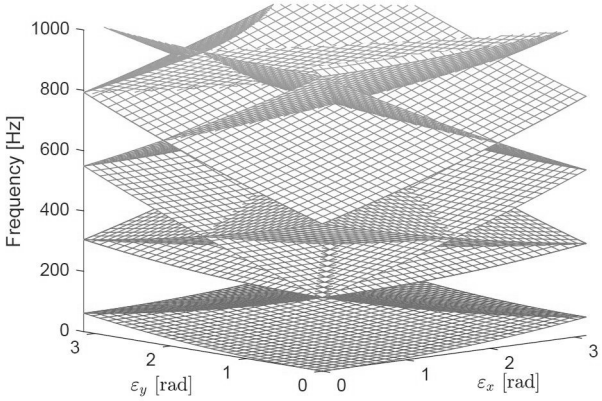

Figure 4.3: The phase constant surfaces of the bending waves of a thin plate.

As the solution to the eigenvalue problem described in Eq. (4.17) is 2π periodic, the phase domain $(\epsilon_\mathrm{x}, \epsilon_y)$ is confined to $[-\pi, \pi] \times [-\pi, \pi]$. This domain is called the Brillouin zone [14]. It follows immediately from Eqs. (4.2) - (4.4) that free waves in opposite directions appear at the same frequency yet with a complex conjugate wave displacement shape: if $\left(\omega_j(\epsilon_\mathrm{x}, \epsilon_\mathrm{y}), \mathbf{u}'_j(\epsilon_\mathrm{x}, \epsilon_\mathrm{y})\right)$ is a solution of (4.17), then so is $\left(\omega_j(-\epsilon_\mathrm{x}, -\epsilon_\mathrm{y}), \mathbf{u}_j^{'*}(\epsilon_\mathrm{x}, \epsilon_\mathrm{y})\right)$, where $*$ denotes the complex conjugate. This limits the range of $(\epsilon_\mathrm{x}, \epsilon_\mathrm{y})$ values that needs be considered in a complete free wave propagation analysis. If the unit cell exhibits symmetry, this range can be further narrowed down to the irreducible Brillouin zone. Suppose that the unit cell is oriented so that the symmetry plane is parallel to the yz plane. Because of this symmetry, free wave propagation for the phase shifts $(\epsilon_\mathrm{x}, \epsilon_\mathrm{y})$ and $(-\epsilon_\mathrm{x}, \epsilon_\mathrm{y})$ will occur at the same frequencies: $\omega_j(\epsilon_\mathrm{x}, \epsilon_\mathrm{y}) = \omega_j(-\epsilon_\mathrm{x}, \epsilon_\mathrm{y})$. The corresponding wave displacement shape can then be obtained by mirroring across the plane of symmetry. In summary, for symmetric unit cells, the analysis can be restricted to $(\epsilon_\mathrm{x}, \epsilon_\mathrm{y}) \in [0, \pi] \times [0, \pi]$.

As pointed out in [75, 100], the frequencies at which undamped free plane wave propagation with phase shifts $(\epsilon_{\mathrm{x}h}, \epsilon_{yl})$ occur, satisfy a total phase shift integer

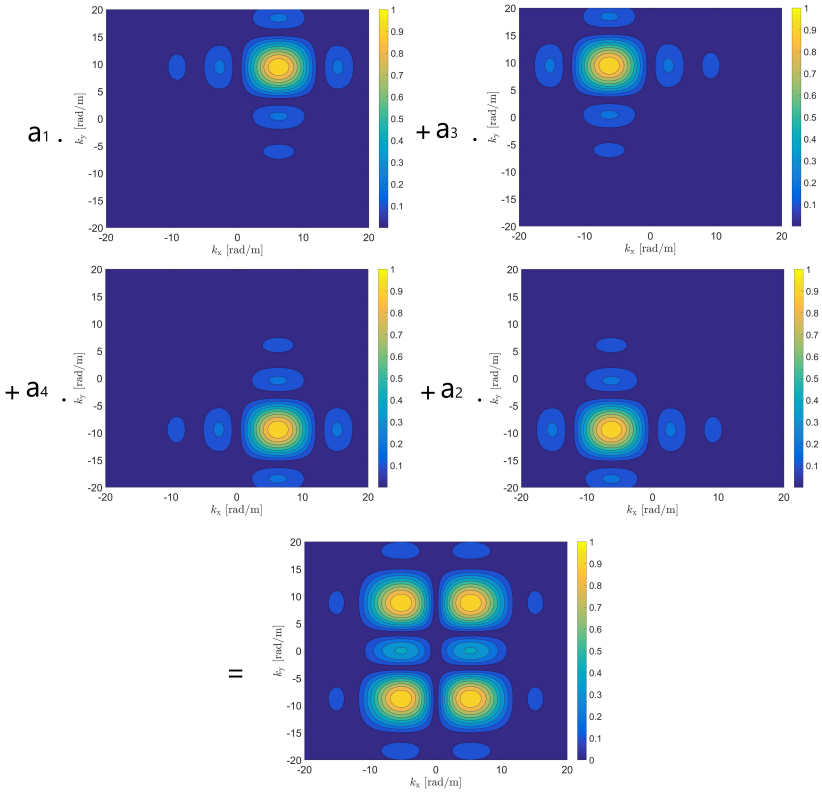

Figure 4.4: A contour plot of the absolute displacement spectrum of a travelling wave in the wavenumber domain, propagating through a finite-sized plate according to four directions with corresponding phase constant combinations $(\epsilon_{\mathrm{x}h}, \epsilon_{\mathrm{y}l})$, $(-\epsilon_{\mathrm{x}h}, \epsilon_{\mathrm{y}l})$, $(\epsilon_{\mathrm{x}h}, -\epsilon_{\mathrm{y}l})$ and $(-\epsilon_{\mathrm{x}h}, -\epsilon_{\mathrm{y}l})$. A linear combination of these plane waves results in the Fourier transform of a sinusoidal function, or in other words a mode shape of the plate.

of 2π:

$$2N_{\mathrm{x}}\epsilon_{\mathrm{x}h} + \epsilon_{\mathrm{x}0} + \epsilon_{\mathrm{x}L} = 2\pi(h-1), \quad 1 \leq h \leq N_{\mathrm{x}}, \tag{4.18}$$

$$2N_{\mathrm{y}}\epsilon_{\mathrm{y}l} + \epsilon_{\mathrm{y}0} + \epsilon_{\mathrm{y}L} = 2\pi(l-1), \quad 1 \leq l \leq N_{\mathrm{y}}, \tag{4.19}$$

where $\epsilon_{\mathrm{x}0}$ and ϵ_{xL} represent the phase shifts introduced by the plane wave boundary reflections at $x = 0$ and $x = L_{\mathrm{x}}$, respectively, and a similar notation is employed for $\epsilon_{\mathrm{y}0}$ and ϵ_{yL}. For a simply supported boundary, where the edges

are unrestrained against rotation, the phase change associated with a boundary reflection equals $-\pi$. If all boundaries are simply supported, then Eqs. (4.18) and (4.19) transform to

$$\epsilon_{\mathrm{x}h} = \frac{h\pi}{N_{\mathrm{x}}} \qquad \text{and} \qquad \epsilon_{\mathrm{y}l} = \frac{l\pi}{N_{\mathrm{y}}}. \tag{4.20}$$

Note that this equation holds for the first phase constant surface ($j = 1$), while for higher phase constant surfaces ($j \geq 2$), k or l can vary from 0 to $N - 1$ as well [100].

The corresponding mode shapes will now be analysed. Following the reasoning that led to the natural frequencies, an undamped mode shape in the entire wall, hence also in the unit cell, is a standing wave that can be obtained as a linear combination of the four related free undamped plane travelling waves (cfr. Fig. 4.4), as follows:

$$\boldsymbol{\psi}_j^{(hl)} = \sum_{r=1}^{4} a_{j,r}^{(hl)} \mathbf{u}_{j,r}^{(hl)}, \tag{4.21}$$

where

$$\begin{aligned} \mathbf{u}_{j,1}^{(hl)} &:= \mathbf{u}_j(\epsilon_{\mathrm{x}h}, \epsilon_{\mathrm{y}l}), \qquad \mathbf{u}_{j,2}^{(hl)} := \mathbf{u}_j(-\epsilon_{\mathrm{x}h}, -\epsilon_{\mathrm{y}l}) = \mathbf{u}_{j,1}^{(hl)^*}, \\ \mathbf{u}_{j,3}^{(hl)} &:= \mathbf{u}_j(-\epsilon_{\mathrm{x}h}, \epsilon_{\mathrm{y}l}), \qquad \mathbf{u}_{j,4}^{(hl)} := \mathbf{u}_j(\epsilon_{\mathrm{x}h}, -\epsilon_{\mathrm{y}l}) = \mathbf{u}_{j,3}^{(hl)^*}. \end{aligned} \tag{4.22}$$

In case of pure travelling waves, one could combine the waves into a standing wave by defining the complex wave amplitudes as: $a_{j,1}^{(hl)} = 1$, $a_{j,2}^{(hl)} = 1$, $a_{j,3}^{(hl)} = -1$ and $a_{j,4}^{(hl)} = -1$ [20, Appendix A]. Another way to compute the complex wave amplitudes is presented in this work. To satisfy simply supported boundary conditions, the complex wave amplitudes $a_{j,r}^{(hl)}$ are determined, such that the normal displacements at the left and bottom boundaries of unit cell (1,1) are zero (cfr. Fig. 4.2(a)). The degrees of freedom, indicating the out-of-plane displacements at the left and bottom boundary of the unit cell, are therefore collected into the vector $\mathbf{u}'_{\mathrm{BC}} = [\mathbf{u}_{\mathrm{z,LT}}^{',\mathrm{T}} \ \mathbf{u}_{\mathrm{z,L}}^{',\mathrm{T}} \ \mathbf{u}_{\mathrm{z,LB}}^{',\mathrm{T}} \ \mathbf{u}_{\mathrm{z,B}}^{',\mathrm{T}} \ \mathbf{u}_{\mathrm{z,RB}}^{',\mathrm{T}}]^{\mathrm{T}}$ with T the transpose. A vector $\mathbf{a}_j^{(hl)} = [a_{j,1}^{(hl)} \ a_{j,2}^{(hl)} \ a_{j,3}^{(hl)} \ a_{j,4}^{(kl)}]^{\mathrm{T}}$ is defined, so that:

$$\left[\mathbf{u}_{\mathrm{BC},j,1}^{',(hl)} \quad \mathbf{u}_{\mathrm{BC},j,2}^{',(hl)} \quad \mathbf{u}_{\mathrm{BC},j,3}^{',(hl)} \quad \mathbf{u}_{\mathrm{BC},j,4}^{',(hl)}\right] \mathbf{a}_j^{(hl)} = \mathbf{0}. \tag{4.23}$$

The vector $\mathbf{a}_j^{(hl)}$ is obtained in this work by a singular value decomposition, in which $\mathbf{a}_j^{(hl)}$ is a right-singular vector, corresponding to a singular value that is

zero. Afterwards, the mode shapes are mass-normalized over the entire wall, so the scaling condition reads

$$\boldsymbol{\psi}_j^{(hl)\mathrm{H}}\mathbf{M}\boldsymbol{\psi}_j^{(hl)} = \sum_{m=1}^{N_\mathrm{x}}\sum_{n=1}^{N_\mathrm{y}} \boldsymbol{\psi}_{mn,j}^{'(hl)\mathrm{H}}\mathbf{M}\boldsymbol{\psi}_{mn,j}^{'(hl)} = 1, \tag{4.24}$$

where (m,n) denotes the location of a specific cell when the cells are numbered from left to right with m and from bottom to top with n (cfr. Fig. 4.2(a)). As the displacement in cell (m,n) relates to the displacement field of the first cell via

$$\mathbf{u}'_{mn}(\epsilon_{\mathrm{x}h},\epsilon_{\mathrm{y}l}) = \mathbf{u}'(\epsilon_{\mathrm{x}h},\epsilon_{\mathrm{y}l})\mathrm{e}^{-\mathrm{i}((m-1)\epsilon_{\mathrm{x}h}+(n-1)\epsilon_{\mathrm{y}l})}, \tag{4.25}$$

the mode shape in cell (m,n) can be obtained from:

$$\begin{aligned}\boldsymbol{\psi}_{mn,j}^{'(hl)} = {} & a_{j,1}^{(hl)}\mathbf{u}_{j,1}^{'(hl)}\mathrm{e}^{-\mathrm{i}((m-1)\epsilon_{\mathrm{x}h}+(n-1)\epsilon_{\mathrm{y}l})} + a_{j,2}^{(hl)}\mathbf{u}_{j,2}^{'(hl)}\mathrm{e}^{\mathrm{i}((m-1)\epsilon_{\mathrm{x}h}+(n-1)\epsilon_{\mathrm{y}l})} \\ & + a_{j,3}^{(hl)}\mathbf{u}_{j,3}^{'(hl)}\mathrm{e}^{\mathrm{i}((m-1)\epsilon_{\mathrm{x}h}-(n-1)\epsilon_{\mathrm{y}l})} + a_{j,4}^{(hl)}\mathbf{u}_{j,4}^{'(hl)}\mathrm{e}^{-\mathrm{i}((m-1)\epsilon_{\mathrm{x}h}-(n-1)\epsilon_{\mathrm{y}l})}.\end{aligned} \tag{4.26}$$

The scaling condition of a mode shape $\boldsymbol{\psi}_{mn,j}^{'(hl)}$ becomes:

$$\begin{aligned}\boldsymbol{\psi}_{mn,j}^{'(hl)\mathrm{H}}\mathbf{M}\boldsymbol{\psi}_{mn,j}^{'(hl)} = {} & \sum_{r=1}^{4}|a_{j,r}^{(hl)}|^2\mathbf{u}_{j,r}^{'(hl)\mathrm{H}}\mathbf{M}\mathbf{u}_{j,r}^{'(hl)} \\ & + 2\mathrm{Re}\left\{a_{j,1}^{*}a_{j,2}\mathbf{u}_{j,1}^{'(hl)\mathrm{H}}\mathbf{M}\mathbf{u}_{j,2}^{'(hl)}\mathrm{e}^{2\mathrm{i}((m-1)\epsilon_{\mathrm{x}h}+(n-1)\epsilon_{\mathrm{y}l})}\right\} \\ & + 2\mathrm{Re}\left\{a_{j,4}^{*}a_{j,3}\mathbf{u}_{j,4}^{'(hl)\mathrm{H}}\mathbf{M}\mathbf{u}_{j,3}^{'(hl)}\mathrm{e}^{2\mathrm{i}((m-1)\epsilon_{\mathrm{x}h}-(n-1)\epsilon_{\mathrm{y}l})}\right\} \\ & + 2\mathrm{Re}\left\{a_{j,1}^{*}a_{j,3}\mathbf{u}_{j,1}^{'(hl)\mathrm{H}}\mathbf{M}\mathbf{u}_{j,3}^{'(hl)}\mathrm{e}^{2\mathrm{i}(m-1)\epsilon_{\mathrm{x}h}} + a_{j,4}^{*}a_{j,2}\mathbf{u}_{j,4}^{'(hl)\mathrm{H}}\mathbf{M}\mathbf{u}_{j,2}^{'(hl)}\mathrm{e}^{2\mathrm{i}(m-1)\epsilon_{\mathrm{x}h}}\right\} \\ & + 2\mathrm{Re}\left\{a_{j,3}^{*}a_{j,2}\mathbf{u}_{j,3}^{'(hl)\mathrm{H}}\mathbf{M}\mathbf{u}_{j,2}^{'(hl)}\mathrm{e}^{2\mathrm{i}(n-1)\epsilon_{\mathrm{y}l}} + a_{j,1}^{*}a_{j,4}\mathbf{u}_{j,1}^{'(hl)\mathrm{H}}\mathbf{M}\mathbf{u}_{j,4}^{'(hl)}\mathrm{e}^{2\mathrm{i}(n-1)\epsilon_{\mathrm{y}l}}\right\}.\end{aligned} \tag{4.27}$$

The scaling of the mode shapes over the entire wall is then found by substituting Eq. (4.27) into Eq. (4.24). Using the Kronecker delta δ_{ij}, the scaling condition

is rewritten as:

$$\boldsymbol{\psi}_j^{(hl)\mathrm{H}}\mathbf{M}\boldsymbol{\psi}_j^{(hl)} = N_\mathrm{x}N_\mathrm{y}\sum_{r=1}^{4}|a_{j,r}^{(hl)}|^2\mathbf{u}_{j,r}^{'(hl)\mathrm{H}}\mathbf{M}\mathbf{u}_{j,r}^{'(hl)}$$
$$+ 2\delta_{h,N_\mathrm{x}}\delta_{l,N_\mathrm{y}}N_\mathrm{x}N_\mathrm{y}\mathrm{Re}\left\{a_{j,1}^{*}a_{j,2}\mathbf{u}_{j,1}^{'(hl)\mathrm{H}}\mathbf{M}\mathbf{u}_{j,2}^{'(hl)} + a_{j,4}^{*}a_{j,3}\mathbf{u}_{j,4}^{'(hl)\mathrm{H}}\mathbf{M}\mathbf{u}_{j,3}^{'(hl)}\right\}$$
$$+ 2\delta_{h,N_\mathrm{x}}N_\mathrm{x}\mathrm{Re}\left\{a_{j,1}^{*}a_{j,3}\mathbf{u}_{j,1}^{'(hl)\mathrm{H}}\mathbf{M}\mathbf{u}_{j,3}^{'(hl)} + a_{j,4}^{*}a_{j,2}\mathbf{u}_{j,4}^{'(hl)\mathrm{H}}\mathbf{M}\mathbf{u}_{j,2}^{'(hl)}\right\}$$
$$+ 2\delta_{l,N_\mathrm{y}}N_\mathrm{y}\mathrm{Re}\left\{a_{j,3}^{*}a_{j,2}\mathbf{u}_{j,3}^{'(hl)\mathrm{H}}\mathbf{M}\mathbf{u}_{j,2}^{'(hl)} + a_{j,1}^{*}a_{j,4}\mathbf{u}_{j,1}^{'(hl)\mathrm{H}}\mathbf{M}\mathbf{u}_{j,4}^{'(hl)}\right\}. \quad (4.28)$$

In summary, the natural frequencies and mode shapes of the periodic wall are obtained from periodic structure theory. The natural frequency ω_j of a standing wave results from the eigenvalue problem of the periodic unit cell in Eqs. (4.2) and (4.17) for an imposed phase-shift combination $(\epsilon_{\mathrm{x}h}, \epsilon_{\mathrm{y}l})$. Using the symmetry of the periodic unit cell, the plane travelling waves $\mathbf{u}_{j,2}^{'(hl)}$, $\mathbf{u}_{j,3}^{'(hl)}$ and $\mathbf{u}_{j,4}^{'(hl)}$, corresponding to the imposed phase shift combinations $(-\epsilon_{\mathrm{x}h}, -\epsilon_{\mathrm{y}l})$, $(-\epsilon_{\mathrm{x}h}, \epsilon_{\mathrm{y}l})$, $(\epsilon_{\mathrm{x}h}, -\epsilon_{\mathrm{y}l})$, are derived from the plane travelling wave $\mathbf{u}_{j,1}^{'(hl)}(\epsilon_{\mathrm{x}h}, \epsilon_{\mathrm{y}l})$. The mode shape $\psi_j^{(hl)}$ with corresponding natural frequency ω_j, is found via a linear combination of these four travelling waves in Eq. (4.21). The coefficients $a_{j,r}^{(hl)}$ of the four travelling waves are obtained by restraining the out-of-plane displacements at the left and bottom edge of the unit cell to satisfy the simply supported boundary conditions, and by mass-normalization of the mode shapes over the entire wall. In the next section, the natural frequencies and mode shapes will be used to determine the dynamic stiffness matrices, needed for the STL prediction.

4.4 Deterministic and direct field dynamic stiffness matrices

The unit modal mass scaling in Eq. (4.24) leads to the following expression for the dynamic stiffness matrix of the wall $D_{\mathrm{d},(jhl,jhl)} = \left[\boldsymbol{\psi}_j^{(hl)\mathrm{H}}\left(\mathbf{M}+(1+\mathrm{i}\eta)\mathbf{K}\right)\boldsymbol{\psi}_j^{(hl)}\right]$

in terms of its modal coordinates:

$$\mathbf{D}_{\mathrm{d}} = -\omega^2\mathbf{I}+(1+\mathrm{i}\eta)\mathbf{\Omega} \qquad \text{with} \qquad \mathbf{\Omega} := \begin{bmatrix} \mathbf{\Omega}_{11} & \mathbf{0} & \dots & \mathbf{0} \\ \mathbf{0} & \mathbf{\Omega}_{21} & \dots & \mathbf{0} \\ \vdots & \vdots & \dots & \vdots \\ \mathbf{0} & \mathbf{0} & \dots & \mathbf{\Omega}_{N_{\mathrm{x}},N_{\mathrm{y}}} \end{bmatrix}, \quad (4.29)$$

where $\mathbf{\Omega}_{hl}$ is the diagonal matrix containing the squared eigenfrequencies as obtained from Eq. (4.17) for $(\epsilon_{\mathrm{x}h}, \epsilon_{\mathrm{y}l})$.

Next, the direct field dynamic stiffness matrix $\mathbf{D}_{\mathrm{dir}}$ of the adjacent acoustic halfspaces is derived in terms of the wall modal coordinates. As for any finite-sized structure, this could be achieved by directly computing the near field radiation impedance for the mode shapes of the entire wall $\boldsymbol{\psi}_j^{(hl)}$ [59, 86]. In the present work, the direct field response is determined via the wavenumber domain as in Eq. (2.62). The modal displacement field in the wavenumber domain of the entire structure $\tilde{\psi}_{\mathrm{z},j}^{(hl)}(k_{\mathrm{x}}, k_{\mathrm{y}})$, needed to obtain the direct field response, contains only out-of-plane motion at the room-wall interface and is obtained via a Fourier transform of Eq. (4.21):

$$\tilde{\psi}_{\mathrm{z},j}^{(hl)}(k_{\mathrm{x}}, k_{\mathrm{y}}) = \sum_{r=1}^{4} a_{j,r}^{(hl)} \underbrace{\iint_S u_{\mathrm{z},j,r}^{(hl)}(x,y)\mathrm{e}^{\mathrm{i}(k_{\mathrm{x}}x+k_{\mathrm{y}}y)}\mathrm{d}x\mathrm{d}y}_{:=\tilde{u}_{\mathrm{z},j,r}^{(hl)}(k_{\mathrm{x}},k_{\mathrm{y}})}, \quad (4.30)$$

where S represents the room-wall interface surface. Since the wall displacement $u_{\mathrm{z},j,r}^{(hl)}(x,y)$ depends entirely on the displacement of the unit cell, $u_{\mathrm{z},j,r}^{'(hl)}(x,y)$, one has that [20]:

$$\begin{aligned} \tilde{u}_{\mathrm{z},j,r}^{(hl)}(k_{\mathrm{x}}, k_{\mathrm{y}}) &= \int\int_S u_{\mathrm{z},j,r}^{(hl)}(x,y)\mathrm{e}^{\mathrm{i}(k_{\mathrm{x}}x+k_{\mathrm{y}}y)}\mathrm{d}x\mathrm{d}y \\ &= \sum_{m=1}^{N_{\mathrm{x}}}\sum_{n=1}^{N_{\mathrm{y}}}\Bigg[\int\int_{S_{\mathrm{cell}}} \underbrace{u_{\mathrm{z},j,r}^{'(hl)}(x,y)\mathrm{e}^{-\mathrm{i}((m-1)\epsilon_{\mathrm{x}h}+(n-1)\epsilon_{\mathrm{y}l})}}_{=u_{\mathrm{z},j,r,mn}^{'(hl)}(x,y)} \\ &\qquad \times \mathrm{e}^{\mathrm{i}(k_{\mathrm{x}}(x+(m-1)l_{\mathrm{x}})+k_{\mathrm{y}}(y+(n-1)l_{\mathrm{y}}))}\mathrm{d}x\mathrm{d}y\Bigg] \end{aligned} \quad (4.31)$$

$$\tilde{u}^{(hl)}_{\mathrm{z},j,r}(k_\mathrm{x},k_\mathrm{y}) = \underbrace{\left[\int\int_{S_\mathrm{cell}} u^{'(hl)}_{\mathrm{z},j,r}(x,y)\mathrm{e}^{\mathrm{i}(k_\mathrm{x}x+k_\mathrm{y}y)}\mathrm{d}x\mathrm{d}y\right]}_{=\tilde{u}^{'(hl)}_{\mathrm{z},j,r}(k_\mathrm{x},k_\mathrm{y})} \times \sum_{m=1}^{N_\mathrm{x}}\sum_{n=1}^{N_y}\mathrm{e}^{-\mathrm{i}((m-1)(\epsilon_{\mathrm{x}h}-k_\mathrm{x}l_\mathrm{x})+(n-1)(\epsilon_{yl}-k_\mathrm{y}l_\mathrm{y}))}, \tag{4.32}$$

where S_cell denotes the surface area of the periodic unit cell. Eq. (4.32) can be rewritten in closed format so that:

$$\tilde{u}^{(hl)}_{\mathrm{z},j,r}(k_\mathrm{x},k_\mathrm{y}) = \tilde{u}^{'(hl)}_{\mathrm{z},j,r}(k_\mathrm{x},k_\mathrm{y})C_{hlr}(k_\mathrm{x},k_\mathrm{y}), \tag{4.33}$$

with

$$C_{hlr}(k_\mathrm{x},k_\mathrm{y}) = \left(\frac{1-\mathrm{e}^{-\mathrm{i}N_\mathrm{x}(\epsilon_{\mathrm{x}h,r}-k_\mathrm{x}l_\mathrm{x})}}{1-\mathrm{e}^{-\mathrm{i}(\epsilon_{\mathrm{x}h,r}-k_\mathrm{x}l_\mathrm{x})}}\right)\cdot\left(\frac{1-\mathrm{e}^{-\mathrm{i}N_\mathrm{y}(\epsilon_{yl,r}-k_\mathrm{y}l_\mathrm{y})}}{1-\mathrm{e}^{-\mathrm{i}(\epsilon_{yl,r}-k_\mathrm{y}l_\mathrm{y})}}\right). \tag{4.34}$$

In summary, the natural frequencies are used to determine the deterministic dynamic stiffness matrix in Eq. (4.29). To obtain the direct field response in modal coordinates, the plane travelling waves $\mathbf{u}^{'(hl)}_{\mathrm{j,r}}$ are first transformed into the wavenumber domain. Secondly, Eqs. (4.33) and (4.34) allow to efficiently convert the displacement field of the travelling waves from the unit cell to the entire structure. The coefficients $a^{(hl)}_{j,r}$ are then used in Eq. (4.30) to combine the waves correctly into mass-normalized standing waves. Finally, the direct field dynamic stiffness matrix is obtained via Eq. (2.62) from the mode shapes and the piece-wise constant Green's function in Eq. (2.77). The resulting direct field dynamic stiffness matrix is a fully populated matrix, which accounts for interaction between the modes (i.e. cross-modal coupling). The sound transmission is then found via Eqs. (2.31) and (2.32).

The main contribution of this modal PFE-SEA approach described in sections 4.3 and 4.4 is that modal behaviour is accounted for in the STL prediction. Ideas in this direction were already mentioned in [20]. Whereas the authors in [20, Appendix A] focus mainly on Born-von Kármán boundary conditions, the wall or floor in the present work is assumed to have simply supported boundary conditions. The proposed PFE-SEA approach inherently accounts for modal behaviour, while including cross-modal coupling. It is noticed that a modal decomposition not only allows to include modal behaviour, but also avoids a double integration over the phase domain resulting from a wave approach to compute the sound transmission loss as in [20, Eq. (37)]. For a hybrid PFE-SEA with a spatial windowing technique, the reader is referred to [20].

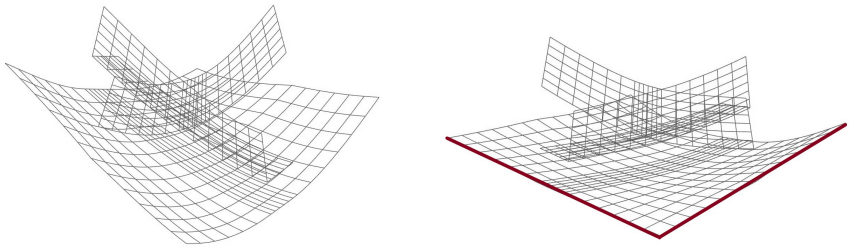

(a) (b)

Figure 4.5: (a) The displacement field of the travelling wave and (b) the corresponding mode shape of the full structure. The out-of-plane displacements on the red lines are zero. The spatial domain is limited to unit cell (1,1).

4.5 Practicalities of the implementation

This section summarizes practicalities of the implementation of the modal PFE-SEA approach such as the truncation of mode shapes and the discretization of the wavenumber domain. Typical errors are illustrated by STL predictions of a two-dimensional periodic rib-stiffened panel. The geometric and material properties of the panel with dimensions 1.1 m × 0.5 m are detailed in section 4.6.2. The unit cell ($l_\mathrm{x} = 100$ mm, $l_\mathrm{y} = 100$ mm) is shown in Fig. 4.23.

The free wave propagation analysis of the periodic unit cell for all possible phase constants $(\varepsilon_{\mathrm{x}h}, \varepsilon_{\mathrm{y}l})$, results in travelling waves with eigenfrequencies $\omega_j(\varepsilon_{\mathrm{x}h}, \varepsilon_{\mathrm{y}l})$ and displacement field $\mathbf{u}'_j(\varepsilon_{\mathrm{x}h}, \varepsilon_{\mathrm{y}l})$. Fig. 4.5(a) shows such a travelling wave of the periodic unit cell. It was shown in section 4.3 how these properties could be converted into the modal characteristics $(\omega_j(\varepsilon_{\mathrm{x}h}, \varepsilon_{\mathrm{y}l}), \boldsymbol{\psi}_j(\varepsilon_{\mathrm{x}h}, \varepsilon_{\mathrm{y}l}))$ of the structure. As an example, the mode shape of the full structure obtained from the travelling wave depicted in 4.5(a), is displayed in Fig. 4.5(b). The out-of-plane displacements at the bottom and left corner of unit cell (1,1) are zero.

The deterministic dynamic stiffness matrix is directly computed using the obtained natural frequencies $\omega_j(\varepsilon_{\mathrm{x}h}, \varepsilon_{\mathrm{y}l})$.

To obtain the direct field response, the travelling waves need to be transformed into the wavenumber domain. First, the displacement field of the travelling wave resulting from the PFE model is projected onto a new spatial grid for the unit cell, which is subdivided d_x and d_y times in respectively the x- and y-direction. The choice of the FE mesh is then independent from the choice of the spatial mesh, used for the computation of the direct field response. Fig. 4.6

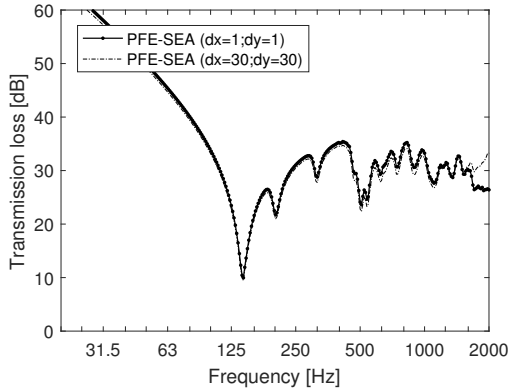

Figure 4.6: The sound transmission loss prediction of a panel as predicted by the hybrid modal PFE-SEA approach in case of a spatial mesh for which $d_{\mathrm{x}} = 1$ and $d_{\mathrm{y}} = 1$, and as predicted by the hybrid modal PFE-SEA approach in case of a spatial mesh for which $d_{\mathrm{x}} = 30$ and $d_{\mathrm{y}} = 30$.

illustrates the case, for which the newly defined spatial mesh for the direct field response computation is too coarse. Discrepancies are visible from 500 Hz onwards. The wavelengths of the contributing modes become shorter than 500 mm. There are no longer 6 elements per wavelength from that 500 Hz onwards when d_{x} and d_{y} are both chosen to be one.

Next, the Fourier transform of the travelling wave in the unit cell was approximated using a trapezoidal numerical integration. Two parameters were defined to automatically generate the mesh in the wavenumber domain, which needed to be fine enough to capture the mode shapes sufficiently accurate: (1) a parameter d_{k} to control the grid spacing in the wavenumber domain and (2) a parameter k_{tol} to truncate the grid in the wavenumber domain.

A travelling wave is characterized by the wavelengths in both directions or, equivalently, the wavenumber combination $(k_{\mathrm{x}hj},k_{\mathrm{y}lj})$, which are related to the phase imposed onto the periodic unit cell. The peaks characterizing the travelling waves in the wavenumber domain appear at multiplications of π/L. The parameter d_{k} is defined such that the grid spacings in the wavenumber domain in the x- and y-direction are respectively $\pi/(L_{\mathrm{x}}d_{\mathrm{k}})$ and $\pi/(L_{\mathrm{y}}d_{\mathrm{k}})$. In the computations d_{k} is chosen to be 4. This proved to be sufficient for all considered examples. For the truncation of the mesh in the wavenumber domain, the maximum wavenumbers $\max(k_{\mathrm{y}lj})$ and $\max(k_{\mathrm{x}hj})$ of the considered mode shapes are sought. Defining $k_{\mathrm{max,x}} = \max(k_{\mathrm{x}hj}) + k_{\mathrm{tol}}$ and $k_{\mathrm{max,y}} = \max(k_{\mathrm{y}lj}) + k_{\mathrm{tol}}$, the wavenumber mesh is limited so that: $(k_{\mathrm{x}}, k_{\mathrm{y}}) = [-k_{\mathrm{max,x}}, k_{\mathrm{max,x}}] \times$

$[-k_{\mathrm{max,y}}, k_{\mathrm{max,y}}]$. The second parameter k_{tol} is chosen to be 10 in all validation examples.

The travelling waves are transformed onto the generated wavenumber domain mesh and converted to travelling waves defined over the full structure. When doing this for the travelling wave in Fig. 4.5(a), the resulting absolute displacement field is displayed in Fig. 4.7(a). Using the complex wave amplitudes, the mode shape in the wavenumber domain is found and shown in Fig. 4.7(b).

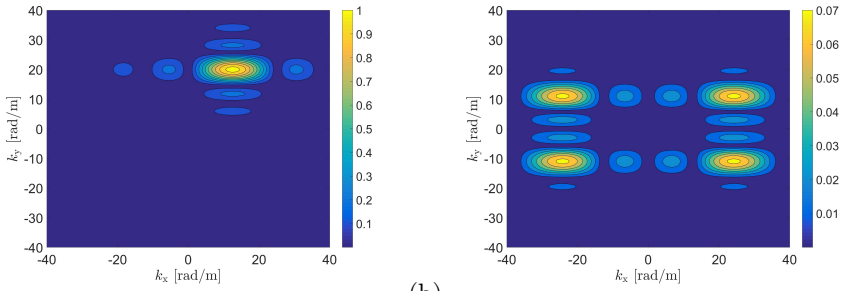

(a) (b)

Figure 4.7: (a) The absolute displacement field of the travelling wave and (b) the absolute displacement field of the corresponding mode shape of the full structure in the wavenumber domain.

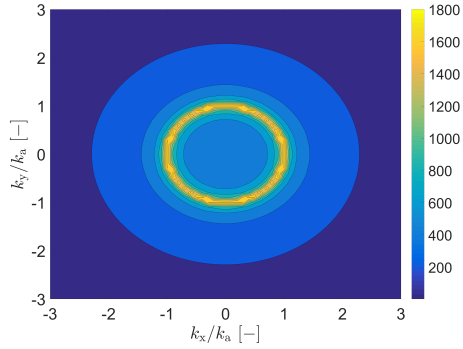

Figure 4.8: The absolute value of the piece-wise constant Green's function in terms of dimensionless wavenumbers $(k_{\mathrm{x}}/k_{\mathrm{a}}, k_{\mathrm{y}}/k_{\mathrm{a}})$.

The response of an acoustic halfspace to a particular mode shape is determined by the Green's function. The radially symmetrical function is shown in Fig. 4.8.

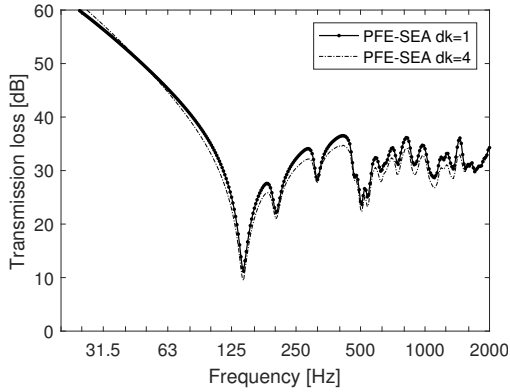

Figure 4.9: The sound transmission loss prediction of a panel as predicted by the hybrid modal PFE-SEA approach in case of a mesh in the wavenumber domain for which $d_{\mathrm{k}} = 1$, and as predicted by the hybrid modal PFE-SEA approach in case of a mesh in the wavenumber domain for which $d_{\mathrm{k}} = 4$.

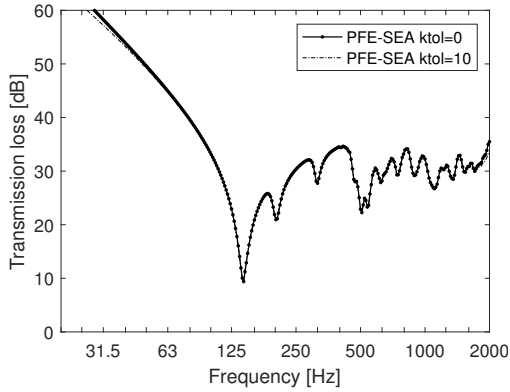

Figure 4.10: The sound transmission loss prediction of a panel as predicted by the hybrid modal PFE-SEA approach in case of a mesh in the wavenumber domain for which $k_{\mathrm{tol}} = 0$, and as predicted by the hybrid modal PFE-SEA approach in case of a mesh in the wavenumber domain for which $k_{\mathrm{tol}} = 10$.

Coincidence happens when the wavenumber of the travelling wave corresponds to the wavenumber in air, resulting in the peak value at $||\mathbf{k}|| = k_{\mathrm{a}}$. Below coincidence ($||\mathbf{k}|| > k_{\mathrm{a}}$), the Green's function is real. Above coincidence ($||\mathbf{k}|| < k_{\mathrm{a}}$), the Green's function is imaginary. For the computation of the direct field

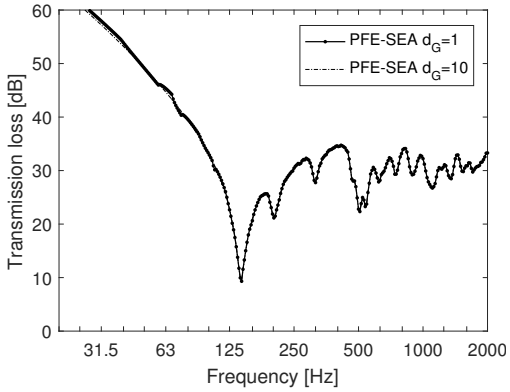

Figure 4.11: The sound transmission loss prediction of a panel as predicted by the hybrid modal PFE-SEA approach in case of a mesh in the wavenumber domain for which $d_{\mathrm{G}} = 1$, and as predicted by the hybrid modal PFE-SEA approach in case of a mesh in the wavenumber domain for which $d_{\mathrm{G}} = 10$.

response, the peak of the Green's function needs to be accurately described. A second mesh in the wavenumber domain is defined for the Green's function. The refinement of the grid is described by the parameter d_{G}, which determines the gridspacing to be $1/d_{\mathrm{G}}$ in the dimensionless wavenumber domain ($k_{\mathrm{x}}/k_{\mathrm{a}}$, $k_{\mathrm{y}}/k_{\mathrm{a}}$). In the current work, $d_{\mathrm{G}} = 10$. As k_{a} is frequency dependent, the grid spacing of the second mesh differs per frequency.

For each frequency, the grid defined for the mode shapes and the grid defined for the Green's function are compared. The most refined grid is chosen. At lower frequencies, the grid spacing of the Green's function is smaller. The already computed mode shapes are interpolated to the mesh of the Green's function via cubic convolution. At higher frequencies, the grid of the Green's function becomes coarser and the grid spacing of the mesh of the mode shapes becomes important. The Green's function is computed for the new grid, as interpolation of the Green's function results in errors. Note that the computation time of the modal hybrid PFE-SEA approach is highly dependent on the grid definition in the wavenumber domain.

The practicalities for the computation of the direct field response have now been discussed. The influence of the parameters on the STL prediction is investigated for a panel. Figure 4.9 illustrates the errors introduced by a coarser ($d_{\mathrm{k}} = 1$) mesh for the mode shapes, which resulted in a discrepancy over the whole frequency range of interest. Reducing the size of the wavenumber domain causes smaller discrepancies, as shown in Fig. 4.10. Mind that k_{tol}

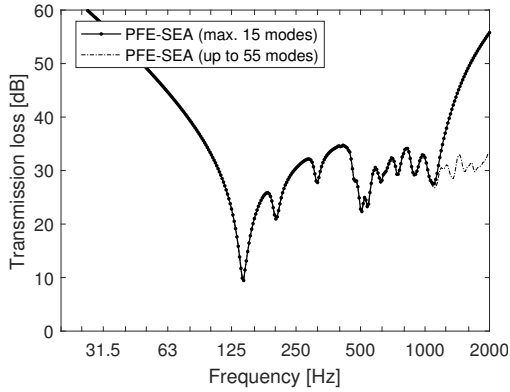

Figure 4.12: The sound transmission loss prediction of a panel as predicted by the hybrid modal PFE-SEA approach in case of a truncation of the number of modes to maximum 15 modes, and as predicted by the hybrid modal PFE-SEA approach using the truncation criteria.

becomes more important above the critical frequency, where the resonant transmission dominates the response. The critical frequency is around 1000 Hz for this particular panel. Figure 4.11 illustrates that deviations occur at lower frequencies when increasing the grid spacing for the Green's function ($d_{\mathrm{G}} = 1$).

The deterministic dynamic stiffness matrix and the direct field dynamic stiffness matrices are frequency dependent. The number of modes per frequency ω is limited using a truncation factor $a_{\mathrm{tr}} = 1.5$, so that only modes for which $\omega_j(\varepsilon_{\mathrm{x}h}, \varepsilon_{\mathrm{y}l}) \leq a_{\mathrm{tr}}\omega$, are accounted for. For the panel, 55 modes are accounted for at the maximum frequency. If the maximum number of modes is fixed to 15 modes, a sudden rise in the STL prediction can be noticed (cfr. Fig. 4.12).

Time [s]	**3-ply CLT**	**5-ply CLT**	**1D periodic**	**2D periodic**
PFE-SEA				
PFE model	1050	1419	265	231
Wave amplitudes	8	8	4	2
Mode shapes	1059	939	121	44
STL computation	8201	4272	265	329
Total time	**10318**	**6638**	**655**	**604**
FE-SEA:				
Total time:	**4326**	**9423**	**5409**	**429**

Table 4.1: Computation time of the mean sound transmission loss for the hybrid PFE-SEA method and the hybrid FE-SEA method.

4.6 Validation examples

The modal PFE-SEA approach that has been introduced in this work, is verified in this section for the following examples: two cross laminated timber panels and two rib-stiffened panels. The STL predictions, obtained from the modal PFE-SEA approach, are compared with those obtained from the hybrid FE-SEA method, in which a full finite element model of the test sample is constructed [86]. A comparison is also made with experimental results, found in literature.

The computation times for the hybrid PFE-SEA approach and hybrid FE-SEA approach for the examples are mentioned in Table 4.1. In addition, the computation time of the hybrid PFE-SEA approach is subdivided further into the free wave propagation analysis of the FE model of the periodic unit cell, the computation of the complex wave amplitudes, the computation of the mode shapes in the wavenumber domain and the computation of the mean and variance of the sound transmission loss, which contains the computation of the deterministic dynamic stiffness matrix and the direct field dynamic stiffness matrices as well. All calculations were performed on a computer with a 2.70 GHz Intel Core i7 processor and 16 GB RAM. In case of the 2D periodic panel, a component mode synthesis was included in the PFE-SEA approach. More details about this reduction technique can be found in section 4.6.2.

It is emphasized that the implementation of both the hybrid FE-SEA approach and the hybrid PFE-SEA approach determines strongly the resulting computation times. Possibly more efficient implementations of both methods could lead to faster computation times. In general, the computation time of the FE-SEA approach is related to the mesh of the FE model and the number of modes that needs to be accounted for, while the computation time of the PFE-SEA approach depends on the number of modes and the discretization in the wavenumber domain. Note that the refinement of the spatial mesh in the PFE-SEA approach and the FE-SEA method differs for the multiple validation examples.

For the validation examples, only the first phase constant surface is accounted for, determining the maximum number of modes that will contribute to the STL predictions. As discussed in section 4.5, an artificial increase in the STL prediction will be noticed when not all modes contributing to the response at that frequency are accounted for. The maximum frequency is therefore dependent on this limitation.

4.6.1 CLT panels

Cross Laminated Timber (CLT) is a wooden construction technique, which is used to construct multi-story wooden buildings. A CLT panel is assembled out of multiple layers of spruce wood or sometimes birch wood, for which the direction of the orthotropic properties of the wooden beams is alternated in each layer. By gluing the layers of a CLT panel together, a solid wooden construction element is obtained. Most CLT panels consist of an odd number of layers, resulting in a highly orthotropic panel. When predicting the sound transmission loss of a CLT panel, two main approaches have been investigated. First, an equivalent orthotropic wall with homogenized material properties can be considered. Such a homogenisation approach was investigated in [109, 110], in which the frequency dependent material properties were found by matching a number of the natural frequencies of beams, cut along the two fibre directions, of a simplified model to an exact model of the CLT panel. In [95] the frequency dependent equivalent bending stiffness for a thin CLT panel has been derived from the experimentally determined flexural wavenumbers, which compensates neglecting the rotational inertia, shear effects and the layered structure of the CLT panel. The obtained material properties were then used to predict the sound transmission loss and sound radiation, assuming the CLT panel to be a thin, baffled, orthotropic plate [93, 94]. Secondly, a full finite element model of the CLT panel could be constructed as was done in [56]. Each layer is modelled separately within this model.

Below, two CLT panels are discussed: a 0.078 m thick three-ply CLT panel with an area density of 42 kg/m^2 and a 0.175 m thick five-ply CLT panel with an area density of 92 kg/m^2. Both panels have lateral dimensions of 3.6 m $\times$ 2.4 m. A damping loss factor of 4 % is assumed in the computations. In the present work, each layer will be separately modelled in the hybrid PFE-SEA approach and the hybrid FE-SEA method instead of using a homogenisation approach. The surface area of the layers are connected to each other to represent the glue in between the layers. The material properties of the spruce boards are taken from literature [78] and are mentioned in Table 4.2. Note that because of the heterogeneous characteristics of the wood, the properties are given according to three main directions: the longitudinal (L) direction parallel to the fibre direction, the tangential (T) direction which is normal to the fibre direction but parallel with the annular rings, and the radial (R) direction, which is both normal to the fibre direction and the annular rings. Practically, the tangential and radial direction are both referred to as perpendicular to the fibre direction, while the longitudinal direction is considered as parallel to the fibre direction. For the simulations, it is assumed that these directions correspond to the axes in a Cartesian coordinate system. As mentioned earlier, the longitudinal direction or ‘strong’ direction is aligned alternately in succeeding layers with the x- or

Name	Parameter	Value
Elasticity modulus in the L direction	E_{L}	10^{10} N/m^2
Elasticity modulus in the T direction	E_{T}	$4.5 \cdot 10^8$ N/m^2
Elasticity modulus in the R direction	E_{R}	$4.5 \cdot 10^8$ N/m^2
Shear modulus in the LT-plane	G_{LT}	$6.5 \cdot 10^8$ N/m^2
Shear modulus in the LR-plane	G_{LR}	$6.5 \cdot 10^8$ N/m^2
Shear modulus in the TR-plane	G_{TR}	$4 \cdot 10^7$ N/m^2
Poisson ratio in the LT-plane	ν_{LT}	0.014 [-]
Poisson ratio in the LR-plane	ν_{LR}	0.014 [-]
Poisson ratio in the TR-plane	ν_{TR}	0.27 [-]

Table 4.2: The material properties of spruce joists, according to the longitudinal (L), tangential (T) and radial (R) direction [78].

y-axis. When the longitudinal direction in a layer is oriented along the x- or y-axis, the layer will be annotated with X or Y respectively, so that the directions of the spruce joists in a 3-ply CLT panel can either be indicated by X-Y-X or by Y-X-Y.

Laboratory room 1 and laboratory room 2 of the transmission suite have a volume of respectively 140 m^3 and 250 m^3 [97, 92, 98]. Similarly as in the experiments, the computations were repeated in the two possible directions of the transmission suite (room 1 to room 2; room 2 to room 1) and averaged out. The reverberation time T, the air density ρ_{a} and the sound speed c_{a} are taken to be 1.5 s, 1.2 kg/m^3 and 343 m/s, respectively. Note that the CLT panels are assumed to be simply supported. In the periodic model, the complex wave amplitudes are computed in Eq. (4.23), so that the out-of plane displacements at the left and lower boundary are zero in the mid-plane of the CLT panel. For the full finite element model, the out-of-plane displacements at the boundaries are restrained in the mid-plane. To ensure that the cross section remains flat after deformation (Bernoulli's hypothesis), extra constraint equations were defined on the boundaries of the finite element model of the entire CLT panel. Without these constraint equations, it was clear that decoupling effects appeared in the mode shapes of the CLT panel, resulting from the different stiffnesses, imposed in the x- and y-direction (cfr. Fig. 4.13).

To define the constraint equations, two nodes are chosen at (x, y, z_1) and (x, y, z_2) for which (x, y) is a location on the boundary. For these examples, the nodes are chosen to be the node on the mid-plane of the structure and the one just above the first one. The nodes are referred to as respectively node 1 and node 2. The height difference between node 1 and 2 is denoted as $\triangle_{12} = z_2 - z_1$. For a node 3 at (x, y, z_3), $\triangle_{13}$ is defined as $z_3 - z_1$. The following constraint

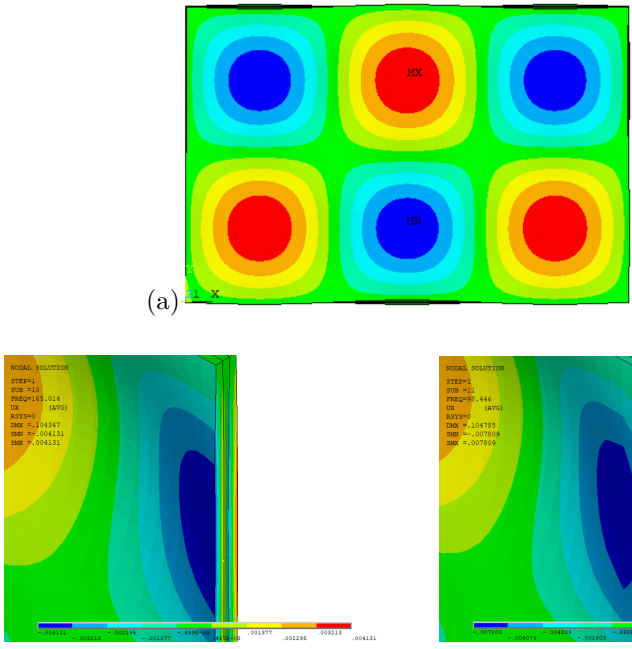

Figure 4.13: (a) The normal displacement field of mode (3,2) of the 3-ply X-Y-X CLT panel with (b) a detailed view on the upper right corner of the panel showing the displacements according to the x-axis through the thickness of the panel and (c) showing the displacements according to the x-axis through the thickness of the panel when constraint equations are applied.

equations are imposed:

$$\left(1-\frac{\triangle_{13}}{\triangle_{12}}\right)u_{\mathrm{x}1}(x,y)+\frac{\triangle_{13}}{\triangle_{12}}u_{\mathrm{x}2}(x,y)-u_{\mathrm{x}3}(x,y)=0, \tag{4.35}$$

$$\left(1-\frac{\triangle_{13}}{\triangle_{12}}\right)u_{\mathrm{y}1}(x,y)+\frac{\triangle_{13}}{\triangle_{12}}u_{\mathrm{y}2}(x,y)-u_{\mathrm{y}3}(x,y)=0, \tag{4.36}$$

$$u_{\mathrm{z},3}(x,y)=u_{\mathrm{z},1}(x,y). \tag{4.37}$$

The experimental data for the 3-ply and 5-ply CLT panel are taken from [98] and [92] respectively. It was specified in [92] that the test sample in the transmission opening was constructed from two separate CLT panels (1.83 m $\times$ 2.44 m). A plywood strip was nailed along the junction to connect the two CLT panels. Note that in the simulations, the connection is not accounted for and the

test sample is simplified to one continuous CLT panel. As the layouts of the CLT panels were not specified in [92] and [98], all options will be taken into consideration. For the 3-ply CLT panel, this means that the STL is predicted for both X-Y-X and Y-X-Y. In case of the 5-ply CLT panel, the STL is determined for X-Y-X-Y-X and Y-X-Y-X-Y.

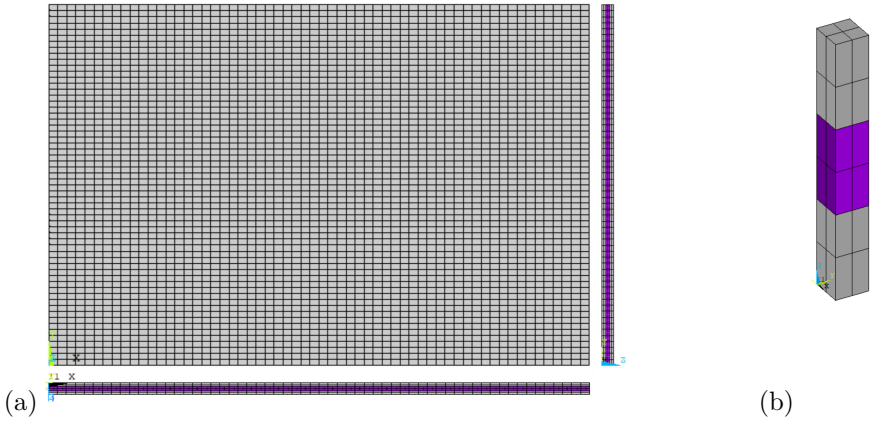

(a) (b)

Figure 4.14: Finite element mesh of (a) the global structure (front, side and top view) and (b) the unit cell for the 3-ply X-Y-X CLT panel. The local coordinate system of the purple elements is rotated 90 degrees to the local coordinate system of the grey elements.

3-ply CLT

For the hybrid PFE-SEA approach, a periodic unit cell of 1 cm by 1 cm is defined ($N_x = 360$; $N_y = 240$) and modelled using 8-node solid elements (of the SOLID185 type in ANSYS). The unit cell is subdivided into 2×2 elements in-plane, and two elements over the thickness for each layer, as shown in Fig. 4.14(b). For the hybrid FE-SEA approach, the panel is modelled using a higher order 20-node solid element (of the SOLID186 type in ANSYS). Two elements over the thickness for each layer are used. In-plane the panel is subdivided into 60×60 elements (cfr. Fig. 4.14(a)).

The results for the 3-ply CLT X-Y-X and 3-ply CLT Y-X-Y are shown respectively in figures 4.15(a) and 4.16(a). A good agreement is found between the STL predictions of the PFE-SEA approach and the results of the hybrid FE-SEA approach. The simply supported boundary conditions are therefore well represented in this modal version of the PFE-SEA approach. Note that a small discrepancy can be noticed in the STL prediction of the first panel resonance at

approximately 25 Hz and the anti-resonance peak at approximately 40 Hz in Fig. 4.16(a). This could be due to small differences in the displacement fields of the mode shapes that are processed in both the hybrid FE-SEA approach and PFE-SEA approach. Moreover, a different discretization is used in the FE and PFE model and the direct field response is computed in different ways.

The orthotropic behaviour of the CLT panel is clearly observed in the STL predictions. First, a plateau can be distinguished in the STL results. As the

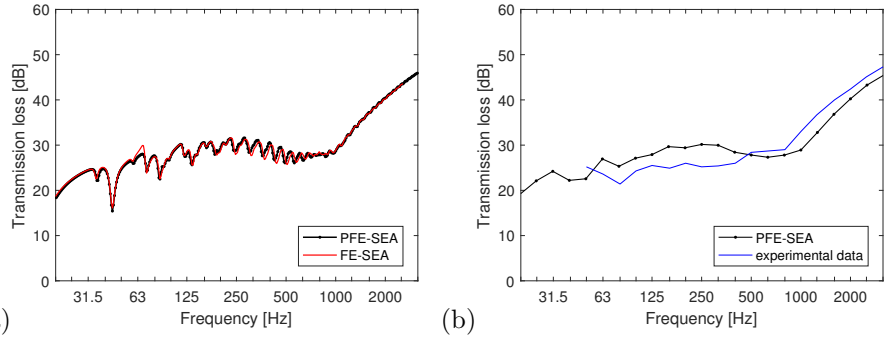

Figure 4.15: Harmonic sound transmission loss of a 3-ply CLT panel (a) as predicted with the hybrid modal PFE-SEA approach (black continuous line) and the hybrid FE-SEA approach (red dashed line) for the lay out X-Y-X; and (b) as measured (blue continuous line) in 1/3 octave bands [98].

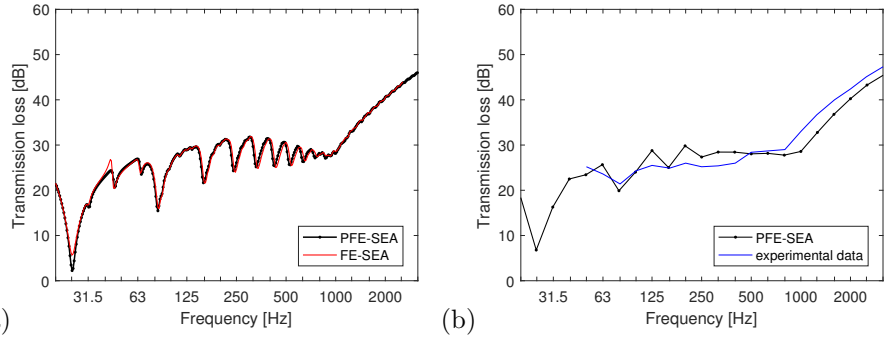

Figure 4.16: The sound transmission loss of a 3-ply CLT panel (a) as predicted with the hybrid modal PFE-SEA approach (black continuous line) and the hybrid FE-SEA approach (red dashed line) for the lay out Y-X-Y; and (b) as measured (blue continuous line) in 1/3 octave bands [98].

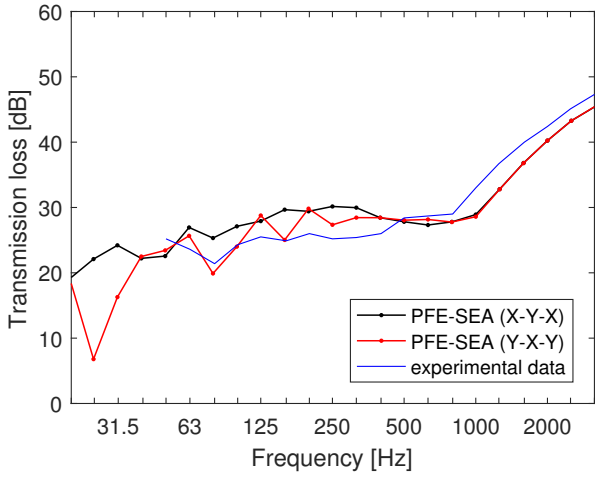

Figure 4.17: The sound transmission loss of a 3-ply CLT panel as predicted by the modal PFE-SEA approach for the lay outs X-Y-X (black continuous line) and Y-X-Y (red continuous line) and as measured (blue continuous line) in 1/3 octave bands [98].

wavelength of a propagating bending wave depends strongly on the direction of propagation, the critical frequency varies according to the direction within the orthotropic panel and the coincidence phenomenon is smeared out in the STL predictions between 250 Hz and 1000 Hz [44]. Secondly, narrow band inspection of the STL results shows strong oscillations in the mid-frequency range. In [87], similar behaviour was observed for an orthotropic panel and it was shown that the dips appear at particular eigenfrequencies, where coincidence or semi-coincidence occurs. Semi-coincidence is the phenomenon for which the natural frequencies of the acoustic waves and the panel mode are approximately equal, but the corresponding wavelengths are only equal along one of the sides of the panel [54]. The oscillations become stronger in case of well-separated eigenfrequencies or well-separated clusters of eigenfrequencies [87].

A comparison between the PFE-SEA predictions and experimental data is displayed in figures 4.15(b) and 4.16(b). The narrow band STL predictions are averaged to obtain the predictions in one-third octave bands. It is emphasized that the material parameters have not been updated to fit the results to the experimental data, but were taken from literature [78]. Differences can therefore be expected. The inclination of the measured STL starts for instance at a lower frequency, indicating a larger flexural bending stiffness in the weak direction for the global CLT panel than the one resulting from the simulations. Nonetheless,

the same tendencies are noticed in both graphs.

When comparing the results of the 3-ply CLT X-Y-X with the predictions of the 3-ply CLT Y-X-Y (cfr. Fig. 4.17), the predicted STL of the 3-ply CLT X-Y-X is remarkably higher in the low- and mid-frequency range. Aligning the stiffest direction of the CLT panel with the longest span, can therefore already be beneficial for the acoustic performance of such a system.

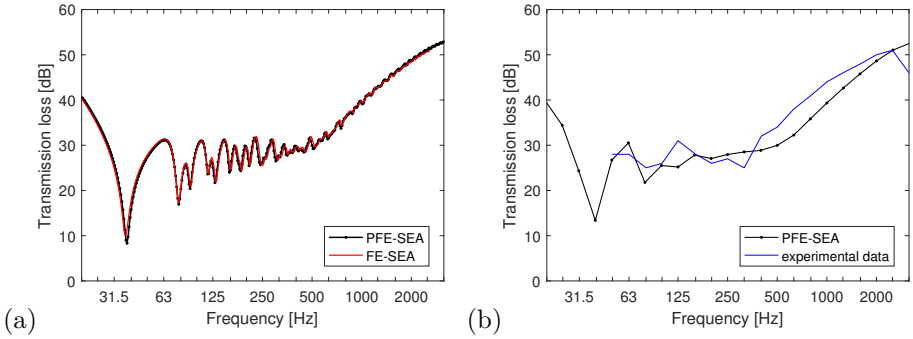

Figure 4.18: The sound transmission loss of a 5-ply CLT panel (a) as predicted with the hybrid modal PFE-SEA approach (black continuous line) and the hybrid FE-SEA approach (red dashed line) for the lay out X-Y-X-Y-X; and (b) as measured (blue continuous line) in 1/3 octave bands [92].

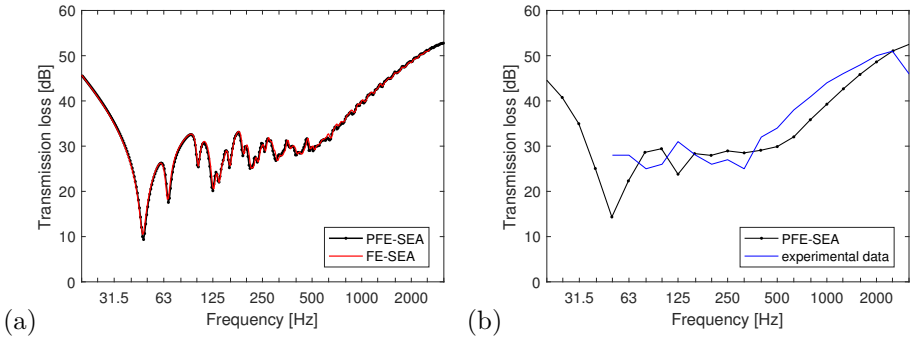

Figure 4.19: The sound transmission loss of a 5-ply CLT panel (a) as predicted with the hybrid modal PFE-SEA approach (black continuous line) and the hybrid FE-SEA approach (red dashed line) for the lay out Y-X-Y-X-Y; and (b) as measured (blue continuous line) in 1/3 octave bands [92].

5-ply CLT

For the hybrid PFE-SEA approach, a periodic unit cell of 1 cm by 1 cm is defined ($N_x = 360$; $N_y = 240$) and modelled using 8-node solid elements (of the SOLID185 type in ANSYS). The unit cell is subdivided into 2×2 elements in-plane, and two elements over the thickness for each layer. For the hybrid FE-SEA approach, the panel is modelled using a higher order 20-node solid element (of the SOLID186 type in ANSYS). For each layer, two elements over the thickness are used. In-plane the panel is subdivided into 60×60 elements.

A comparison between the STL predicted by the PFE-SEA approach and the FE-SEA approach are shown in figures 4.18(a) and 4.19(a). Excellent agreement is obtained. By adding two layers to the 3-ply CLT panel, the test sample becomes stiffer. As a result, the coincidence region shifts to lower frequencies, while the natural frequencies shifts towards higher frequencies. The first panel resonances occur now at approximately 40 Hz and 50 Hz.

Figures 4.18(b) and 4.19(b) compare the STL results of the PFE-SEA approach with experimental data. Again, the bending stiffness is underestimated in the hybrid PFE-SEA approach. Results could possibly be improved by tuning the Young's moduli of the spruce. Yet this was not attempted here. It is noticed that also in the measured STL the coincidence region shifts to lower frequencies and that the modal behaviour is more pronounced than for the 3-ply CLT experiments, confirming the occurring phenomena in the predictions.

4.6.2 Rib-stiffened panels

Rib-stiffened panel with one-dimensional periodicity

Consider the rib-stiffened panel shown in figure 4.20. It consists of a polymethyl methacrylate (PMMA) base plate, to which eleven steel ribs are glued and screwed. The base plate has dimensions $L_x = 1.235$ m and $L_y = 1.485$ m and a thickness of $t_p = 15$ mm. The steel ribs have a thickness of $t_s = 3$ mm and an outer leg length of $L_s = 30$ mm. The centre-to-centre spacing between the ribs is $d_x = 100$ mm. The vertical distance between the ribs and the outer edge of the base plate is $a_y = 52.5$ mm. The horizontal distance between the outer edge and the centre of the first rib is $a_x = 102.5$ mm. The airborne sound transmission loss was measured for this panel in the Acoustics Laboratory of KU Leuven [87]. Each laboratory room has a volume of 87 m^3. The reverberation time T, the air density ρ_a and the sound speed c_a are taken to be 1.5 s, 1.2 kg/m^3 and 343 m/s, respectively. The material properties of the rib-stiffened panel in [87] were calibrated by minimizing the differences between measured eigenfrequencies

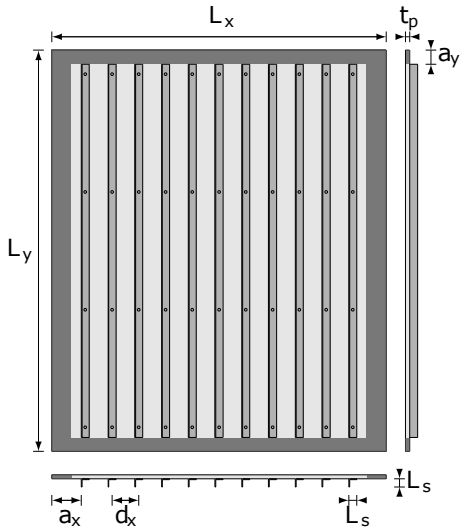

Figure 4.20: Front, side and top view of the rib-stiffened panel. Cropping the rib-stiffened panel by ignoring the dark grey zones, gives a 1D periodic structure (adapted figure from [87]).

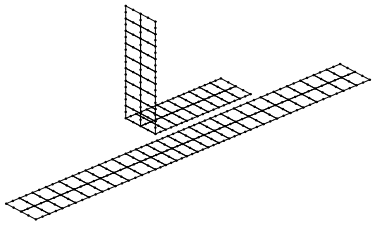

Figure 4.21: The mesh of the 1D periodic unit cell, used in the PFE-SEA approach. Shell elements were used for the ribs and base panel. Constraint equations link the ribs to the base panel.

and mode shapes, and the values obtained from the finite element model at low frequencies. These material properties are also adopted in the FE and PFE model in this work and are mentioned in Table 4.3.

The rib-stiffened panel is assumed to be periodic for the simulations. The panel is therefore cropped as displayed in figure 4.20. The periodic panel has dimensions $L_{\mathrm{x}} = 1.1$ m and $L_{\mathrm{y}} = 1.38$ m. For the FE model of the full panel, the reader is referred to the shell-shell model, described in [87]. The periodic unit cell, used in the hybrid PFE-SEA approach, has a width of $l_{\mathrm{x}} = 100$ mm and a length of $l_{\mathrm{y}} = 10$ mm ($N_{\mathrm{x}} = 11$; $N_{\mathrm{y}} = 138$) (cfr. Fig. 4.21). Both the plate and ribs are modelled using 8-node shell elements. To simulate simply supported behaviour, the out-of-plane displacements at the boundaries of the base panel are restrained. The nodes that connect the ribs to the base panel, are coupled via constraint equations that account for the offset between the ribs and base panel. A node of the base panel in the unit cell is referred to as bp, the node of the rib at the same horizontal location (x, y) is denoted as r and the distance between the two nodes is referred to as $\triangle$. The constraint

equations, which link the connection areas of the ribs and base panel, are then:

$$u_{\mathrm{x,r}}(x,y) = u_{\mathrm{x,bp}}(x,y) + \triangle\theta_{\mathrm{y,bp}}(x,y), \quad u_{\mathrm{y,r}}(x,y) = u_{\mathrm{y,bp}}(x,y) - \triangle\theta_{\mathrm{x,bp}}(x,y),$$
$$u_{\mathrm{z,r}}(x,y) = u_{\mathrm{z,bp}}(x,y), \quad \theta_{\mathrm{x,r}}(x,y) = \theta_{\mathrm{x,bp}}(x,y),$$
$$\theta_{\mathrm{y,r}}(x,y) = \theta_{\mathrm{y,bp}}(x,y), \quad \theta_{\mathrm{z,r}}(x,y) = \theta_{\mathrm{z,bp}}(x,y). \tag{4.38}$$

In the constraint equations, u_{x}, u_{y} and u_{z} denote the translations according to the axes in the Cartesian coordinate system, while θ_{x}, θ_{y} and θ_{z} indicate the rotations around the x-, y- and z-axis.

(a)

Name	Parameter	Value
Density	ρ_{p}	1170 kg/m^3
Elasticity modulus	E_{p}	$4.23 \cdot 10^9$ N/m^2
Poisson ratio	ν_{p}	0.35 [-]

(b)

Name	Parameter	Value
Density	ρ_{s}	7850 kg/m^3
Elasticity modulus	E_{s}	$210 \cdot 10^9$ N/m^2
Poisson ratio	ν_{s}	0.3 [-]

(c)

f [Hz]	100	125	160	200	250	315	400	500
η	0.049	0.049	0.056	0.065	0.046	0.056	0.062	0.040
f [Hz]	630	800	1000	1250	1600	2000	2500	3150
η	0.060	0.055	0.059	0.054	0.044	0.038	0.035	0.027

Table 4.3: The material properties of (a) the base panel and (b) the steel ribs. The damping loss factor of the rib-stiffened panel in 1/3 octave bands is given in (c) [87].

The STL predictions of the hybrid PFE-SEA approach and the FE-SEA approach for the 1D periodic rib-stiffened panel are shown in figure 4.22(a). The predictions are on top of each other with only a small discrepancy at the first anti-resonance. The heavy oscillatory behaviour due to (semi-)coincidence has been investigated in detail for this structure in [87]. A comparison with experimental data is shown in 4.22(b). It is emphasized that in the experiments the non-periodic rib-stiffened panel was used, while in the simulations the panel is assumed to be perfectly periodic. A good agreement is found. The small shift of the STL dips between the measurements and the predictions of the hybrid PFE-SEA approach is due to the difference in size. The 95% confidence interval,

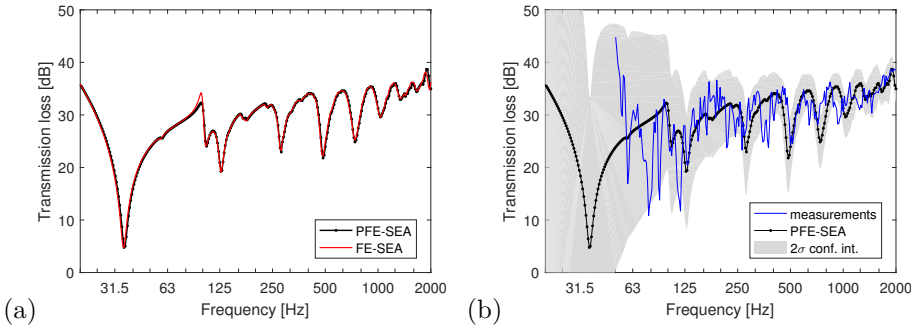

Figure 4.22: The sound transmission loss of a 1D periodic rib-stiffened panel (a) as predicted with the hybrid modal PFE-SEA approach (black continuous line) and the hybrid FE-SEA approach (red dashed line); and (b) as measured in the Acoustic Laboratory of KU Leuven (blue continuous line). The 2σ confidence interval, computed with the hybrid PFE-SEA approach, is shown in the right figure.

related to the diffuse field assumption in the source room, is also plotted. This uncertainty is well captured by the PFE-SEA predictions: at low frequencies, where the modal overlap of the rooms is low and their modal behaviour has a large influence on the transmission loss, the PFE-SEA predictions have a large uncertainty, while they have a small uncertainty at high frequencies, where the modal overlap of the rooms is large.

Rib-stiffened panel with two-dimensional periodicity

The example of the 1D periodic rib-stiffened panel is expanded towards a two-dimensional (2D) periodic structure with lateral dimensions $L_x = 1.1$ m and $L_y = 0.5$ m. The rib-stiffened panel exists of a PMMA base panel with thickness $t_p = 15$ mm, stiffened by eleven steel L-ribs, aligned with the y-axis and with a thickness of $t_s = 3$ mm and outer leg length $L_s = 15$ mm. The centre-to-centre distance between the L-ribs is 100 mm. The horizontal distance between the L-ribs and the outer edge of the base plate is $a_x = 43.3$ mm. The base panel is further stiffened by vertical ribs with a height of 15 mm, aligned with the x-axis. The centre-to-centre distance of the vertical ribs is 100 mm and the vertical distance of the vertical ribs to the outer edge of the base panel is $a_y = 50$ mm. The material properties of the PMMA panel and the steel ribs are the same as before, see Table 4.3.

The periodic unit cell, used in the hybrid PFE-SEA approach, has a width of $l_x = 100$ mm and a length of $l_y = 100$ mm ($N_x = 11$; $N_y = 5$). The finite

element mesh of the periodic unit cell is shown in Fig. 4.23. The plate, the L-ribs and the vertical ribs are modelled using 8-node shell elements. The nodes that connect the ribs to the base panel, are coupled via constraint equations that account for the offset between the ribs and base panel. To simulate simply supported behaviour, the out-of-plane displacements at the boundaries of the base panel are restrained. Following [20], the stiffness and mass matrices of the periodic unit cell are reduced using Component Mode Synthesis (CMS), which is basically a Rayleigh Ritz analysis involving the degrees of freedom of the internal nodes. Conveniently, the degrees of freedom of the periodic unit cell are already organised such that $\mathbf{u}' = [\mathbf{u}_\mathrm{I}^{',\mathrm{T}}\ \mathbf{u}_\mathrm{b}^{',\mathrm{T}}]^\mathrm{T}$ with $\mathbf{u}'_\mathrm{b}$ the degrees of freedom at the boundary (b) of the unit cell. The interior DOFs $\mathbf{u}'_\mathrm{I}$ are approximated by a set of generalized internal DOFs $\mathbf{q}_\Phi$ as follows:

$$\mathbf{u}' = \begin{bmatrix}\mathbf{u}'_\mathrm{I}\\ \mathbf{u}'_\mathrm{b}\end{bmatrix} \approx \mathbf{C}\begin{bmatrix}\mathbf{q}_\Phi\\ \mathbf{u}'_\mathrm{b}\end{bmatrix}, \qquad \mathbf{C} = \begin{bmatrix}\boldsymbol{\varphi}_{11} & \boldsymbol{\varphi}_{12}\\ \boldsymbol{\varphi}_{21} & \boldsymbol{\varphi}_{22}\end{bmatrix}. \tag{4.39}$$

The first set of Ritz vectors are chosen to be the mode shapes of the periodic unit cell with clamped boundaries:

$$\begin{bmatrix}\boldsymbol{\varphi}_{11}\\ \boldsymbol{\varphi}_{21}\end{bmatrix} = \begin{bmatrix}\boldsymbol{\phi}_{11}\\ \mathbf{0}\end{bmatrix}, \tag{4.40}$$

where $\boldsymbol{\phi}_{11}$ is obtained from the following eigenvalue problem:

$$\left(\begin{bmatrix}\mathbf{K}'_{11} & \mathbf{K}'_{12}\\ \mathbf{K}'_{21} & \mathbf{K}'_{22}\end{bmatrix} - \boldsymbol{\Lambda}_{11}\begin{bmatrix}\mathbf{M}'_{11} & \mathbf{M}'_{12}\\ \mathbf{M}'_{21} & \mathbf{M}'_{22}\end{bmatrix}\right)\begin{bmatrix}\boldsymbol{\phi}_{11}\\ \mathbf{0}\end{bmatrix} = \mathbf{0}, \tag{4.41}$$

which can be simplified as:

$$\mathbf{K}'_{11}\boldsymbol{\phi}_{11} = \mathbf{M}'_{11}\boldsymbol{\phi}_{11}\boldsymbol{\Lambda}_{11}, \tag{4.42}$$

where $\boldsymbol{\Lambda}_{11}$ represents a diagonal matrix, containing the corresponding eigenvalues and $\boldsymbol{\phi}_{11}$ the corresponding eigenvectors.

Additionally, a second set of Ritz vectors is defined as the static response of a structure, on which a unit displacement or rotation is applied at a boundary DOF while constraining the other DOFs:

$$\begin{bmatrix}\mathbf{K}'_{11} & \mathbf{K}'_{12}\\ \mathbf{K}'_{21} & \mathbf{K}'_{22}\end{bmatrix}\begin{bmatrix}\boldsymbol{\phi}_{12}\\ \mathbf{I}\end{bmatrix} = \begin{bmatrix}\mathbf{0}\\ \mathbf{f}_\mathrm{b}\end{bmatrix}, \quad \begin{bmatrix}\boldsymbol{\varphi}_{12}\\ \boldsymbol{\varphi}_{22}\end{bmatrix} = \begin{bmatrix}-{\mathbf{K}'_{11}}^{-1}\mathbf{K}'_{12}\\ \mathbf{I}\end{bmatrix}. \tag{4.43}$$

The transformed mass and stiffness matrices are found as:

$$\mathbf{M}'_\mathrm{C} = \mathbf{C}^\mathrm{H}\mathbf{M}'\mathbf{C}, \qquad \mathbf{K}'_\mathrm{C} = \mathbf{C}^\mathrm{H}\mathbf{K}'\mathbf{C}, \tag{4.44}$$

with

$$\mathbf{C} = \begin{bmatrix} \boldsymbol{\phi}_{11} & -\mathbf{K}'^{-1}_{11}\mathbf{K}'_{12} \\ \mathbf{0} & \mathbf{I} \end{bmatrix}. \tag{4.45}$$

For this particular example, the FE model of the periodic unit cell (cfr. Fig. 4.23) contains 9234 DOFs, from which 8058 are internal DOFs. In the computation, 200 clamped mode shapes are considered, so that $\mathbf{M}'_{\mathrm{C}} \in \mathbb{C}^{1376\times1376}$ and $\mathbf{K}'_{\mathrm{C}} \in \mathbb{C}^{1376\times1376}$. The reduced mass and stiffness matrices are then used in Eqs. (4.17) and (4.4), resulting in a reduction of the computational effort when solving the eigenvalue problem for the multiple, imposed phase lag combinations $(\epsilon_{\mathrm{x}k}, \epsilon_{\mathrm{y}l})$.

The finite element mesh of the unit cell was repeated in the finite element mesh of the full structure. 4-node shell elements (of the SHELL181 type in ANSYS) were used for the finite element model of the complete structure.

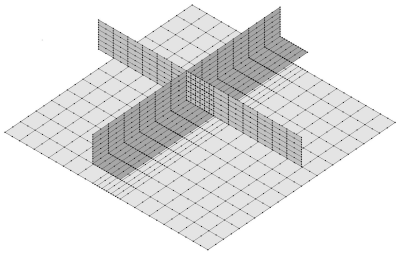

Figure 4.23: The mesh of the 2D periodic unit cell for the rib-stiffened panel in the PFE-SEA approach. Shell elements were used for the ribs and base panel. Constraint equations link the ribs to the base panel.

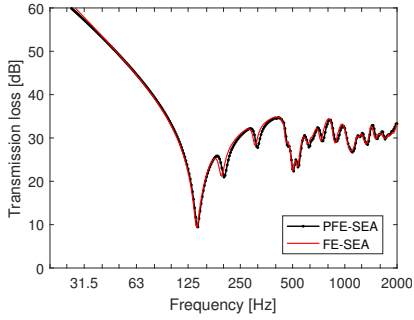

Figure 4.24: The sound transmission loss of a rib-stiffened panel with 2D periodicity as predicted with the hybrid modal PFE-SEA approach (black continuous line) and the hybrid FE-SEA approach (red dashed line).

The STL predictions of the hybrid PFE-SEA approach and the hybrid FE-SEA method for the 2D periodic rib-stiffened panel are shown in figure 4.24. The panel is now stiffened in both directions and has a smaller length, resulting in a structure with a higher stiffness than the 1D periodic rib stiffened panel, discussed previously. The first panel resonance therefore appears at 143 Hz. The results of the PFE-SEA approach follow closely the predictions of the FE-SEA method. The oscillatory behaviour due to the modal behaviour and (semi-)coincidence is well predicted using the PFE-SEA approach.

4.7 Projection on sinusoidal basis functions

In this section, an alternative approach is considered to approximately account for modal behaviour, while using periodic finite element modelling. The basic idea consists of projecting the displacement field of the panel onto a set of sinusoidal basis functions as in §3.3.2. The sinusoidal basis functions $\boldsymbol{\psi}_{\mathrm{sin}}$ were already defined in Eq. (3.53).

In order to obtain the sound transmission, the direct field dynamic stiffness matrix and the deterministic stiffness matrix in terms of the generalized coordinates need to be determined. Similar as in section 4.4, the direct field response is determined by Eq. (2.62) using an analytical expression for the displacement field of the sinusoidal basis function $\psi_{\mathrm{sin},l}$ defined for $(x, y) \in [0, L_{\mathrm{x}}] \times [0, L_{\mathrm{y}}]$, in the wavenumber domain:

$$\begin{aligned}\tilde{\psi}_{\mathrm{sin},l}(k_{\mathrm{x}}, k_{\mathrm{y}}) =& \frac{1}{2}\left(\frac{\mathrm{e}^{\mathrm{i}(k_{\mathrm{x}}-k_{\mathrm{sin},l\mathrm{x}})L_{\mathrm{x}}}-1}{k_{\mathrm{x}}-k_{\mathrm{sin},l\mathrm{x}}}+\frac{1-\mathrm{e}^{\mathrm{i}(k_{\mathrm{x}}+k_{\mathrm{sin},l\mathrm{x}})L_{\mathrm{x}}}}{k_{\mathrm{x}}+k_{\mathrm{sin},l\mathrm{x}}}\right)\\ &\times\frac{1}{2}\left(\frac{\mathrm{e}^{\mathrm{i}(k_{\mathrm{y}}-k_{\mathrm{sin},l\mathrm{y}})L_{\mathrm{y}}}-1}{k_{\mathrm{y}}-k_{\mathrm{sin},l\mathrm{y}}}+\frac{1-\mathrm{e}^{\mathrm{i}(k_{\mathrm{y}}+k_{\mathrm{sin},l\mathrm{y}})L_{\mathrm{y}}}}{k_{\mathrm{y}}+k_{\mathrm{sin},l\mathrm{y}}}\right).\end{aligned} \tag{4.46}$$

The deterministic dynamic stiffness matrix for a thin plate is obtained by projecting the sinusoidal basis functions onto the infinite plate wave dynamic stiffness matrix $\mathbf{D}^{\infty}$ [21, Eq. (A6)]. The expression is expanded towards two dimensions in this section. The lth diagonal element of the deterministic dynamic stiffness matrix becomes:

$$D_{\mathrm{d},l}(\omega) = \int\int_{S} \psi_l^*(x, y) f_l(\omega, x, y)\mathrm{d}x\mathrm{d}y. \tag{4.47}$$

Knowing that the generalized forces in the wavenumber domain are obtained using the dynamic stiffness matrix of the infinite system as follows:

$$\tilde{f}_l(\omega, k_{\mathrm{x}}, k_{\mathrm{y}}) = D^{\infty}(\omega, k_{\mathrm{x}}, k_{\mathrm{y}})\tilde{\psi}_l(k_{\mathrm{x}}, k_{\mathrm{y}}), \tag{4.48}$$

the forces $f_l(\omega, x, y)$ are computed as the inverse Fourier transform of Eq. (4.48):

$$f_l(x, y) = \frac{1}{4\pi^2}\int_{-\infty}^{\infty}\int_{-\infty}^{\infty} D^{\infty}(k_{\mathrm{x}}, k_{\mathrm{y}})\tilde{\psi}_l(k_{\mathrm{x}}, k_{\mathrm{y}})\mathrm{e}^{-\mathrm{i}(k_{\mathrm{x}}x+k_{\mathrm{y}}y)}\mathrm{d}k_{\mathrm{x}}\mathrm{d}k_{\mathrm{y}}. \tag{4.49}$$

Substituting Eq. (4.49) into Eq. (4.47) results in:

$$D_{\mathrm{d},l}(\omega) = \int\int_S \psi_l^* \left[\frac{1}{4\pi^2} \int_{-\infty}^{\infty} \int_{-\infty}^{\infty} D^{\infty} \tilde{\psi}_l \mathrm{e}^{-\mathrm{i}(k_\mathrm{x}x + k_\mathrm{y}y)} \mathrm{d}k_\mathrm{x} \mathrm{d}k_\mathrm{y} \right] \mathrm{d}x\mathrm{d}y \tag{4.50}$$

$$= \frac{1}{4\pi^2} \int_{-\infty}^{\infty} \int_{-\infty}^{\infty} \left[\int\int_S \psi_l^* \mathrm{e}^{-\mathrm{i}(k_\mathrm{x}x + k_\mathrm{y}y)} \mathrm{d}x\mathrm{d}y \right] D^{\infty} \tilde{\psi}_l \mathrm{d}k_\mathrm{x}\mathrm{d}k_\mathrm{y} \tag{4.51}$$

$$= \frac{1}{4\pi^2} \int_{-\infty}^{\infty} \int_{-\infty}^{\infty} D^{\infty}(\omega, k_\mathrm{x}, k_\mathrm{y}) |\tilde{\psi}_l(k_\mathrm{x}, k_\mathrm{y})|^2 \mathrm{d}k_\mathrm{x}\mathrm{d}k_\mathrm{y}. \tag{4.52}$$

Periodic finite element modelling can now be used to determine the infinite plate wave dynamic stiffness matrix $\mathbf{D}^{\infty}(\omega, k_\mathrm{x}, k_\mathrm{y})$. Solving the eigenvalue problem in Eq. (4.4) for an imposed phase lag combination $(\epsilon_\mathrm{x}, \epsilon_\mathrm{y})$, results in multiple propagating waves with displacement shapes $\mathbf{u}'_j(\epsilon_\mathrm{x}, \epsilon_\mathrm{y})$ and corresponding eigenfrequencies $\omega_j(\epsilon_\mathrm{x}, \epsilon_\mathrm{y})$. The wavenumber combination of a bending wave is related to the phase lag combination via: $\epsilon_\mathrm{x} = k_\mathrm{x} l_\mathrm{x} \bmod 2\pi$, $\varepsilon_\mathrm{y} = k_\mathrm{y} l_\mathrm{y} \bmod 2\pi$. Each obtained travelling wave $\mathbf{u}'(k_\mathrm{x}, k_\mathrm{y})$ therefore corresponds to a wavenumber combination $(k_\mathrm{x}, k_\mathrm{y})$. A wave decomposition is used to transform the dynamic stiffness matrix of the unit cell into the infinite plate wave dynamic stiffness matrix by imposing the obtained travelling waves on the unit cell:

$$D^{\infty}(k_\mathrm{x}, k_\mathrm{y}) = \mathbf{u}'^{\mathrm{H}}(k_\mathrm{x}, k_\mathrm{y})[-\mathbf{M}'\omega^2 + \mathbf{K}']\mathbf{u}'(k_\mathrm{x}, k_\mathrm{y}). \tag{4.53}$$

It is noted that the travelling waves $\mathbf{u}'(k_\mathrm{x}, k_\mathrm{y})$ are scaled to the area density m:

$$\mathbf{u}'^{\mathrm{H}}(k_\mathrm{x}, k_\mathrm{y})\mathbf{M}'\mathbf{u}'(k_\mathrm{x}, k_\mathrm{y}) = m. \tag{4.54}$$

For a homogeneous panel, $m = \rho t$ with ρ and t respectively the density and thickness of the plate. For more complicated structures, the mass per unit surface area is obtained by dividing the total mass of the unit cell by its surface area.

As an example, the methodology outlined in this section is used to predict the sound transmission loss of the hollow brick wall that was described in section 3.5.1. The brick wall is subdivided into 100×100 periodic unit cells, from which the finite element mesh is displayed in Fig. 4.25(a). The STL predicted by the sPFE-SEA approach, is shown in Fig. 4.25(b) and compared to the results obtained by the various hybrid methodologies that have been discussed throughout this work: the hybrid FE-SEA approach, the hybrid mTMM-SEA method and the hybrid PFE-SEA approach. The outcome of the sPFE-SEA approach is shifted a lot in comparison with the other predictions, indicating that the brick wall in the sPFE-SEA approach behaves noticeably stiffer. This is due to different boundary conditions. As the sinusoidal basis functions are

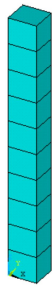

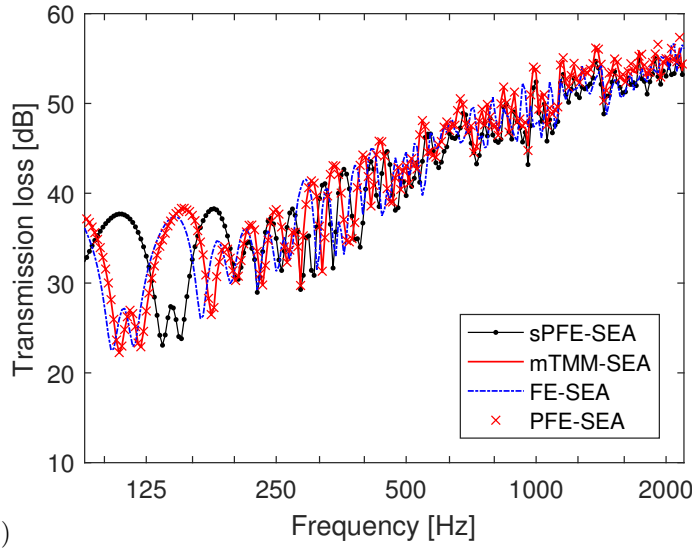

(a) (b)

Figure 4.25: The finite element mesh of the periodic unit cell of the brick wall is shown in (a). The sound transmission loss of the brick wall (b) as predicted with the hybrid sPFE-SEA approach, the hybrid FE-SEA approach, the hybrid mTMM-SEA approach and the hybrid PFE-SEA method.

imposed in the wavenumber domain (cfr. Eq. (4.52)), it is unclear how the basis functions are imposed through thickness. Expanding this theory towards thick or periodic structures is therefore difficult.

4.8 Conclusions

This chapter considers integrating periodic finite element modelling into the hybrid framework while accounting for the modal behaviour of the periodic wall or floor system. To obtain the sound transmission loss, the deterministic and direct field dynamic stiffness matrices need to be determined in terms of the modal coordinates. To do so, periodic boundary conditions are imposed onto the periodic unit cell, resulting in an eigenvalue problem in function of frequency and the phase lag across the unit cell in both directions. Imposing discrete phases that accumulate standing waves in the full structure, allows to solve the eigenvalue problem for the natural frequencies and displacement fields of propagating waves. The displacement fields of the propagating waves are then transformed to the wavenumber domain, which allows for a quick conversion to

the displacements fields of the full structure. Next, the displacement fields of the corresponding standing waves are found as a linear combination of these propagating waves, while satisfying the simply supported boundary conditions. Finally, the obtained natural frequencies and mode shapes of the standing waves are used to determine the needed dynamic stiffness matrices. Practicalities of the method such as truncation of the number of modes and the discretization of the grid in the wavenumber domain are discussed.

The introduced periodic finite element-statistical energy analysis approach allows to exploit the periodic lay out of many building elements and to incorporate more details such as orthotropic layers or rib-stiffeners. The method is verified for two cross laminated timber panels and a rib-stiffened panel by comparing the predictions with the results of a method involving a finite element model of the full structure and experimental data. The modal behaviour of the periodic test samples is well predicted. A comparison with a hybrid framework involving a full finite element model shows a good agreement. Similar as for the mTM-SEA method, the modal behaviour of the rooms is not included in the method but a variance computation is possible. The mentioned computation times indicated mixed results: the PFE-SEA approach proved to be faster than the FE-SEA method for two out of the four validation examples. It should be mentioned that the implementation determines strongly the computational efficiency of both methods and that possibly better implementation could lead to smaller computation times. It is however certain that less time is needed to model the reduced periodic unit cell, compared to a full finite element model of the structure.

Alternatively, another approach was described, which makes use of a set of sinusoidal basis functions instead of the exact modal characteristics of the periodic unit cell. Because of the difference in imposed boundary conditions, the sound transmission loss predictions of thick and periodic walls and floors are shifted, when comparing them to other approaches.

Chapter 5

Conclusions and future research

5.1 Conclusion of the PhD project

The aim of this research was to develop an acoustic design tool, which is accurate enough to avoid extensive experimental prototype testing and efficient enough to be used as a design tool. As finite size effects can be important in the considered acoustical frequency range, special attention was directed to account for the modal behaviour of the building element.

As a result, two novel methodologies were developed in this work: the mTM-SEA approach and the PFE-SEA method. The conclusions of the mTM-SEA approach for thick and layered building systems and of the PFE-SEA method for periodic building elements can be found respectively in §5.1.1 and §5.1.2.

5.1.1 The mTM-SEA approach

A hybridization between the transfer matrix method and statistical energy analysis has been developed for computing the diffuse sound transmission through finite walls and floors that consist of layers of solid, fluid and/or poro-elastic material. The modal behaviour of the wall is approximately accounted for by decomposing the displacements into a set of sinusoidal basis functions which satisfy the simply supported boundary conditions. The sound insulation predictions for several building elements with increasing complexity have been

compared with experimental data. It was noted that the method was not applicable for building elements with thin air layers [37], unless the cavity is modelled analytically. Overall, the modal behaviour was well predicted, while gaining computational efficiency by using a semi-analytical method instead of finite elements.

Comparison with alternative methods yields the following conclusions: The approach is computationally very efficient when compared to the hybrid FE-SEA approach since detailed finite element modelling of the wall is avoided, while maintaining a sufficient level of accuracy. In addition, the connection with statistical energy analysis enables to estimate the variance of the predicted sound insulation that is inherent to the statistical diffuse field models of the rooms. This uncertainty characterization is not possible when using TMM-based methods. Additionally, the wavelet approach in combination with the hybrid framework allows to incorporate cross-modal coupling in the mTM-SEA approach, which was shown to be important at low to medium frequencies, especially at anti-resonance frequencies of the wall.

The mTM-SEA approach has been expanded towards impact noise as well. This model has been used to compute the response of a concrete floor with floating screed to a tapping machine and the radiated sound power of an inclined glass panel subjected to rain.

5.1.2 The PFE-SEA approach

A hybridization between two-dimensional periodic finite element modelling and statistical energy analysis has been investigated for periodic structures with simply supported boundary conditions. When accounting for modal behaviour, the dynamic properties of the unit cell only need to be evaluated for a number of imposed phase constants. The resulting travelling waves are combined into standing waves, in a way which satisfies the simply supported boundary conditions. The obtained natural frequencies and corresponding mode shapes are then used to compute the dynamic stiffness matrices, which are needed for the prediction of the sound transmission loss. To validate the proposed method, the sound transmission loss is predicted for two cross laminated timber panels and two rib-stiffened panels. A good agreement is obtained between the predictions of the novel method with results of the hybrid finite element-statistical energy analysis approach and experimental data.

The introduced methodology has the advantage of including modal behaviour, which is not the case for most methodologies using periodic finite element modelling. In [20] the authors suggested to combine the propagating waves into standing waves, but they did not consider the different phases of the

resulting propagating waves. The novel method allows to inherently construct the standing waves, by computing the complex wave amplitudes so that the simply supported boundary conditions are met. In addition, by embedding the periodic finite element method into the hybrid framework, cross-modal coupling can be accounted for and the computation of the variance of the sound transmission loss, related to the diffuse field assumption of the rooms, is a possibility. In comparison with the hybrid FE-SEA approach, the novel approach allows to restrict the finite element model to the unit cell instead of the full structure.

5.2 Recommendations for future research

For future research, the following developments could still be explored:

- **Boundary conditions**

  In the present work, the prediction of the sound transmission through simply supported, finite-sized building elements is discussed. Future research can focus on expanding the current the PFE-SEA approach towards other boundary conditions, such as clamped boundary conditions for instance.

  For clamped boundary conditions, the phase change associated with the reflection at the boundary is $-\pi/2$ rad [41]. The phase shifts for which the eigenvalue problem of the unit cell needs to be solved for, should be re-examined first. Secondly, expressions for the mode shapes of a panel with clamped boundary conditions are given in [64]. The mode shapes are more complicated than the sinusoidal basis functions of a simply supported plate. The displacement field of the clamped plate is a linear combination of four travelling waves and four evanescent waves [41]. Therefore, also four imaginary phase shifts should be imposed. More investigation is needed to check the validity of the obtained mode shapes.

  For the expansion of the mTM-SEA method to clamped boundary conditions, a new set of basis functions should be chosen. In [128], the authors opt to use shifted cosinusoidal basis functions to approximate clamped boundary conditions. The accuracy of this approximation should be investigated.

- **Impact noise**

  The prediction of impact noise for layered systems has been discussed briefly in this PhD thesis in the case of a harmonic point force, a tapping machine and rain noise. Impact models for a tapping machine were

discussed in detail in [123]. It was shown that the assumption of a perfectly rigid contact of the impact hammer with the floor is acceptable for rigid, heavyweight floors, where the hammer rebounds without energy loss after impact. The prediction of the impact force becomes more complex for lightweight floors. An impact model which accounts for the interaction between the hammers of the tapping machine and the finite-sized floor, is proposed in [123].

For future research, the impact force model of rain noise can still be investigated in more detail. The impact model used in this work, relies on the model of a harmonic point force. For each hole in the tray used in the experiment, a train of droplets is assumed which have a random position and random phase to ensure that the several train of droplets are uncorrelated. However, assuming that the imposed random phase remains constant for each subsequent impact for the train of droplets, is quite simplistic. Although the obtained radiated sound power was in close agreement with the other models [96], more validation and research is thus needed to ensure the accuracy of the impact force model for rain noise. The uncertainty, due to the random positions of the rain droplets and random phase, could be investigated using a Monte Carlo simulation.

Using the impact models in combination with numerical prediction tools allows to compute the radiated sound power of complicated structures. In the present work, impact noise was considered for the application of layered building elements. The expansion towards periodic building elements can still be considered. The basic concept to compute the radiated sound power using the hybrid framework was introduced in chapter 2. Since the mode shapes of the periodic structure are defined in the wavenumber domain, the conversion of the forces into the modal forces should be transformed to the wavenumber domain as well. This conversion needs to be examined.

- **Optimisation**

  Recent studies [108, 111, 112] involve the optimisation of periodic structures such as gypsum board walls, perforated hollow brick walls and metamaterials. The novel methods, developed in this work, are certainly an asset for the optimisation of such structures. In [112], the broadband acoustic performance of the considered gypsum board walls, consisting of two panels separated by a metal stud with(out) absorbent material in the cavity, is captured by the single number rating. The studs are then altered via shape optimization, in order to maximize the single number rating, while also defining extra constraint equations considering the material cost for instance. Similarly, the sound transmission loss for the following structures could still be improved:

– Laminated glazing:

  Laminated glazing is a layered element, consisting of two glass panels separated by a visco-elastic interlayer, such as polyvinyl butyral (PVB). The added resilient interlayer results in a significant improvement of the sound transmission loss around coincidence. In case of double glazing, one or both panels could be a laminated glass panel, resulting in added damping around coincidence of the glass panels and a change in stiffness. The temperature dependent material properties and thickness of the visco-elastic interlayer can be optimised to maximize the acoustic performance within the given constraints.

– Hollow brick walls:

  A hollow brick wall consists of periodic perforated bricks built on top of each other. The perforated pattern of the bricks could be investigated in more detail, using a periodic finite element model.

– CLT panels:

  CLT has been discussed in this work. The dynamic behaviour of the orthotropic panel can be captured efficiently in the finite element model of the periodic unit cell. Several details have not been considered yet in the PFE model, such as the glue in between the layers, the gaps and relief grooves in between and inside the boards, ... The validity of the model should therefore be confirmed first. This model can then be used to optimise the material properties and thicknesses of the layers, so as to maximise the single number rating of the considered CLT panel.

Bibliography

[1] *Geluidsisolatie voor de muur: Isolatiematerialen & Prijs*, 2020 (accessed December 16, 2020). https://www.isolatieprijs.be/geluidsisolatie/muur/.

[2] Alimonti, L., Atalla, N., and Berry, A. A hybrid finite element-transfer matrix model for vibroacoustic systems with flat and homogeneous acoustic treatments. *Journal of the Acoustical Society of America 137*, 2 (2015), 976–988.

[3] Allard, J., and Atalla, N. *Propagation of sound in porous media*, 2nd ed. John Wiley & Sons, Chichester, UK, 2009.

[4] António, J. M. P., Tadeu, A., and Godinho, L. Analytical evaluation of the acoustic insulation provided by double infi

nite walls. *Journal of Sound and Vibration 263* (2003), 113–129.

[5] Architectura. *Post X*, 2018 (accessed December 14, 2020). https://www.architectura.be/nl/projecten/25239/post-x.

[6] Belgisch Instituut voor Normalisatie. *NBN S 01-400-1: Akoestische criteria voor woongebouwen*, 2008.

[7] Beliris. *Renovatie van de sociale woontoren Ieder Zijn Huis*, 2014 (accessed December 14, 2020). http://www.beliris.be/nl/projecten/iederzijnhuis.html.

[8] Beranek, L., and Work, G. Sound transmission through multiple structures containing flexible blankets. *Journal of the Acoustical Society of America 21*, 4 (1949), 419–428.

[9] Bernhard, R. The limits of predictability due to manufacturing and environmentally induced uncertainty. In *Proceedings of Inter-Noise 96, the 25th International Congress on Noise Control Engineering* (Liverpool, U.K., July-August 1996).

[10] Biot, M. Theory of propagation of elastic waves in a fluid-saturated porous solid. I. low-frequency range. *Journal of the Acoustical Society of America 28* (1956), 168–178.

[11] Biot, M. Theory of propagation of elastic waves in a fluid-saturated porous solid. II. high-frequency range. *Journal of the Acoustical Society of America 28* (1956), 179–191.

[12] Bonfiglio, P., Pompoli, F., and Lionti, R. A reduced-order integral formulation to account for the finite size effect of isotropic square panels using the transfer matrix method. *Journal of the Acoustical Society of America 139*, 4 (2016), 1773–1783.

[13] Brekke, A. Calculation methods for the transmission loss of single, double and triple partitions. *Applied Acoustics 14* (1981), 225–240.

[14] Brillouin, L. *Wave propagation in periodic structures*, 2nd ed. Dover Publications, New York City, NY, 1953.

[15] Brouard, B., Lafarge, D., and Allard, J. A general method of modelling sound propagation in layered media. *Journal of Sound and Vibration 183*, 1 (1995), 129–142.

[16] Brunskog, J. The influence of finite cavities on the sound insulation of double-plate structures. *Journal of the Acoustical Society of America 117* (2005), 3727–3739.

[17] Brunskog, J., and Davidsson, P. Sound transmission of structures. A finite element approach with simplified room description. *Acta Acustica united with Acustica 90*, 5 (2004), 847–857.

[18] Brunskog, J., and Hammer, P. Prediction model for the impact sound level of lightweight floors. *Acta Acustica united with Acustica 89*, 2 (2003), 309–322.

[19] Christen, J., Ichchou, M., Zine, A., and Troclet, B. Formulation of the acoustic transmission through complex infinite plates. *Acta Acustica united with Acustica 102*, 6 (2016), 984–991.

[20] Cotoni, V., Langley, R., and Shorter, P. A statistical energy analysis subsystem formulation using finite element and periodic structure theory. *Journal of Sound and Vibration 318*, 4–5 (2008), 1077–1108.

[21] Cotoni, V., Shorter, P., and Langley, R. Numerical and experimental validation of a hybrid finite element-statistical energy analysis method. *Journal of the Acoustical Society of America 122*, 1 (2007), 259–270.

[22] Craik, R. *Sound transmission through buildings using statistical energy analysis*. Gower, Aldershot, UK, 1996.

[23] Craik, R., and Wilson, R. Sound transmission through masonry cavity walls. *Journal of Sound and Vibration 179*, 1 (1995), 79–96.

[24] Craik, R. J. M., and Smith, R. S. Sound transmission through double leaf lightweight partitions part II: structure-borne sound. *Applied Acoustics 61* (2000), 247–269.

[25] Cremer, L. Theorie der Schalldämmung dünner Wände bei schrägem Einfall. *Akustische Zeitschrift 7* (1942), 81–104.

[26] Cremer, L., Heckl, M., and Petersson, B. *Structure-borne sound: Structural vibrations and sound radiation at audio frequencies*, 3rd ed. Springer, Berlin, 2005.

[27] Crocker, M., and Price, A. Sound transmission using statistical energy analysis. *Journal of Sound and Vibration 9*, 3 (1969), 469–486.

[28] Daidalos Peutz. *Balk van Beel*, 2008 (accessed December 14, 2020). `http://www.daidalospeutz.be/projecten/balk-van-beel`.

[29] Davy, J., Larner, D., Wareing, R., and Pearse, J. The acoustic radiation impedance of a rectangular panel. *Building and Environment 92* (2015), 743–755.

[30] De Geetere, L., and Ingelaere, B. A new building acoustical concept for lightweight timber frame constructions. In *Proceedings of 7th Forum Acusticum* (Kraków, Poland, September 2014). CD-ROM.

[31] Deckers, E., Jonckheere, S., Van Belle, L., Claeys, C., and Desmet, W. Prediction of transmission, reflection and absorption coefficients of periodic structures using a hybrid wave based - finite element unit cell method. *Journal of Computational Physics 356* (2018), 282–302.

[32] Decraene, C., Dijckmans, A., and Reynders, E. P. Fast mean and variance computation of the diffuse sound transmission through finite-sized thick and layered wall and floor systems. *Journal of Sound and Vibration 422* (2018), 131–145.

[33] Delany, M., and Bazley, E. Acoustical properties of fibrous materials. *Applied Acoustics 3*, 2 (1970), 105–116.

[34] Deraemaeker, A., Babuška, I., and Bouillard, P. Dispersion and pollution of the FEM solution for the helmholtz equation in one, two and three dimensions. *International Journal for Numerical Methods in Engineering 46*, 4 (1999), 471–499.

[35] Dijckmans, A. *Wave based calculation methods for sound-structure interaction: Application to sound insulation and sound radiation of composite walls and floors.* PhD thesis, KU Leuven, 2011.

[36] Dijckmans, A., and Vermeir, G. A wave based model to predict the niche effect on sound transmission loss of single and double walls. *Acta Acustica united with Acustica 98* (2012), 111–119.

[37] Dijckmans, A., and Vermeir, G. Development of a hybrid wave based - transfer matrix model for sound transmission analysis. *Journal of the Acoustical Society of America 133*, 4 (2013), 2157–2168.

[38] Dym, C. L., and Lang, M. A. Transmission of sound through sandwich panels. *Journal of the Acoustical Society of America 56*, 5 (1974), 1523–1532.

[39] Ebeling, K. J. Statistical properties of random wave fields. In *Physical acoustics Vol. XVII*, W. P. Mason and R. N. Thurston, Eds. Academic Press, Orlando, FL, 1984, pp. 233–310.

[40] ecobuild. *Woodskot*, 2019 (accessed December 14, 2020). `https://www.ecobuild.brussels/nl/project/woodskot`.

[41] Fahy, F., and Gardonio, P. *Sound and structural vibration: radiation, transmission and response*, 2nd ed. Academic Press, Oxford, UK, 2007.

[42] Folds, D., and Loggins, C. Transmission and reflection of ultrasonic waves in layered media. *Journal of the Acoustical Society of America 62*, 5 (1977), 1102–1109.

[43] Geebelen, N. *Structure-borne sound sensitivity of building structures: assessment of the acoustic performances of multilayered structures by simulation and measurement techniques.* PhD thesis, KU Leuven, 2008.

[44] Heckl, M. Untersuchungen an orthotropen Platten. *Acustica 10*, 2 (1960), 109–115.

[45] Heckl, M. The tenth Sir Richard Fairey memorial lecture: Sound transmission in buildings. *Journal of Sound and Vibration 77* (1981), 165–189.

[46] Holland, O., and Van Lancker, E. *Antwerpen krijgt eerste houten wolkenkrabber van België.* De Tijd, 2020 (accessed December 14, 2020). https://www.tijd.be/sabato/architectuur/antwerpen-krijgt-eerste-houten-wolkenkrabber-van-belgie/10222524.html.

[47] Hopkins, C. *Sound insulation.* Elsevier Ltd., Oxford, 2007.

[48] International Organization for Standardization. *ISO-140-3:1995: Acoustics - Measurement of sound insulation in buildings and of building elements - Part 3: Laboratory measurements of airborne sound insulation of building elements*, 1995.

[49] International Organization for Standardization. *ISO 10848-1:2006: Acoustics – Laboratory measurement of the flanking transmission of airborne and impact sound between adjoining rooms – Part 1: Frame document*, 2006.

[50] International Organization for Standardization. *ISO 10140: Acoustics – Laboratory measurement of sound insulation of building elements*, 2010.

[51] International Organization for Standardization. *ISO 12354-1:2017: Building Acoustics - Estimation of acoustic performance of buildings from the performance of elements - Part 1: Airborne sound insulation between rooms*, 2017.

[52] International Organization for Standardization. *ISO 12354-2:2017: Building Acoustics - Estimation of acoustic performance of buildings from the performance of elements - Part 2: Impact sound insulation between rooms*, 2017.

[53] Jacqus, G., Berger, S., Gibiat, V., Jean, P., Villot, M., and Ciukay, S. A homogenised vibratory model for predicting the acoustic properties of hollow brick walls. *Journal of Sound and Vibration 330*, 14 (2011), 3400–3409.

[54] Josse, R., and Lamure, C. Transmission du son par une paroi simple. *Acustica 14*, 5 (1964), 266–280.

[55] Kang, Y., and Bolton, J. A finite element model for sound transmission through foam-lined double-panel structures. *Journal of the Acoustical Society of America 99*, 5 (1996), 2755–2765.

[56] Kohrmann, M. *Numerical methods for the vibro-acoustic assessment of timber floor constructions.* PhD thesis, Technical University Munich, 2017.

[57] Kurtze, G., and Watters, B. G. New wall design for high transmission loss or high damping. *Journal of the Acoustical Society of America 31*, 6 (1959), 739–748.

[58] Langley, R. A note on the force boundary conditions for two-dimensional periodic structures with corner freedoms. *Journal of Sound and Vibration 167*, 2 (1993), 377–381.

[59] Langley, R. Numerical evaluation of the acoustic radiation from planar structures with general baffle conditions using wavelets. *Journal of the Acoustical Society of America 121*, 2 (2007), 766–777.

[60] Langley, R. On the diffuse field reciprocity relationship and vibrational energy variance in a random subsystem at high frequencies. *Journal of the Acoustical Society of America 121* (2007), 913–921.

[61] Langley, R., and Brown, A. The ensemble statistics of the energy of a random system subjected to harmonic excitation. *Journal of Sound and Vibration 275*, 35 (2004), 823–846.

[62] Langley, R., and Cotoni, V. Response variance prediction for uncertain vibro-acoustic systems using a hybrid deterministic-statistical method. *Journal of the Acoustical Society of America 122*, 2 (2007), 3445–3463.

[63] Lauriks, W., Mees, P., and Allard, J. The acoustic transmission through layered systems. *Journal of Sound and Vibration 155*, 1 (1992), 125–132.

[64] Leissa, A. *Vibration of plates*. NASA, Washington D.C., USA, 1969.

[65] Leppington, F., Broadbent, E., and Heron, K. The acoustic radiation efficiency of rectangular panels. *Proceedings of the Royal Society A - Mathematical, Physical and Engineering Sciences 382*, 1783 (1982), 245–271.

[66] Ljunggren, S. Airborne sound insulation of thick walls. *Journal of the Acoustical Society of America 89*, 5 (1991), 2338–2345.

[67] London, A. Transmission of reverberant sound through double walls. *Journal of the Acoustical Society of America 22*, 2 (1950), 270–279.

[68] Lyon, R. H., and DeJong., R. G. *Theory and application of statistical energy analysis*, 2nd ed. Butterworth-Heinemann, Newton, MA, 1995.

[69] Mace, B. Sound radiation from fluid loaded orthogonally stiffened plates. *Journal of Sound and Vibration 79*, 3 (1981), 439–452.

[70] Mace, B. The vibration of plates on two-dimensionally periodic point supports. *Journal of Sound and Vibration 192*, 3 (1996), 629–643.

[71] Mace, B., and Manconi, E. Modelling wave propagation in two-dimensional structures using finite element analysis. *Journal of Sound and Vibration 318*, 4-5 (2008), 884–902.

[72] Mace, B., and Manconi, E. Wave motion and dispersion phenomena: Veering, locking and strong coupling effects. *Journal of the Acoustical Society of America 131*, 3 (2012), 1015–1028.

[73] Mead, D. A general theory of harmonic wave propagation in linear periodic systems with multiple coupling. *Journal of Sound and Vibration 27*, 2 (1973), 235–260.

[74] Mead, D. Wave propagation in continuous periodic structures: Research contributions from Southampton. *Journal of Sound and Vibration 190*, 3 (1996), 495–524.

[75] Mead, D., and Parthan, S. Free wave propagation in two-dimensional periodic plates. *Journal of Sound and Vibration 64*, 3 (1979), 325–348.

[76] Mehta, M. *Random Matrices*, 3nd ed. Elsevier, San Diego, CA, 2004.

[77] Mulholland, K. A., Parbrook, H. D., and Cummings, A. The transmission loss of double panels. *Journal of Sound and Vibration 6* (1967), 324–334.

[78] Neuhaus, H. *Ingenieurholzbau: Grundlagen - Bemessung - Nachweise -Beispiele*. Vieweg + Teubner Verlag, 2009.

[79] Nilsson, A. C. Wave propagation in and sound transmission through sandwich plate. *Journal of Sound and Vibration 138*, 1 (1990), 73–94.

[80] Panneton, R., and Atalla, N. Numerical prediction of sound transmission through finite multilayer systems with poroelastic materials. *Journal of the Acoustical Society of America 100*, 1 (1996), 346–354.

[81] Parrinello, A., and Ghiringhelli, G. Transfer matrix representation for periodic planar media. *Journal of Sound and Vibration 317* (2016), 196–209.

[82] Parrinello, A., Ghiringhelli, G., and Atalla, N. Generalized transfer matrix method for periodic planar media. *Journal of Sound and Vibration 464* (2020), 114993.

[83] Price, A. J., and Crocker, M. J. Sound transmission through double panels using statistical energy analysis. *Journal of the Acoustical Society of America 47* (1970), 683–693.

[84] Putra, A., and Thompson, D. Sound radiation from rectangular baffled and unbaffled plates. *Applied Acoustics 71* (2010), 1113–1125.

[85] Rayleigh, L. *The theory of sound*, 2nd ed., vol. I. Dover publications, New York, NY, 1894.

[86] Reynders, E., Langley, R., Dijckmans, A., and Vermeir, G. A hybrid finite element - statistical energy analysis approach to robust sound transmission modelling. *Journal of Sound and Vibration 333*, 19 (2014), 4621–4636.

[87] Reynders, E., Van hoorickx, C., and Dijckmans, A. Sound transmission through finite rib-stiffened and orthotropic plates. *Acta Acustica united with Acustica 102*, 6 (2016), 999–1010.

[88] Reynders, E., Wang, P., Van hoorickx, C., and Lombaert, G. Prediction and uncertainty quantification of structure-borne sound radiation into a diffuse field. *Journal of Sound and Vibration 463* (2019), 114984.

[89] Rhazi, D., and Atalla, N. A simple method to account for size effects in the transfer matrix method. *Journal of the Acoustical Society of America, Express Letters 127*, 2 (2010), 30–36.

[90] Rhazi, D., and Atalla, N. Acoustic and vibration response of a structure with added noise control treatment under various excitations. *Journal of the Acoustical Society of America 135*, 2 (2014), 693–704.

[91] Rumerman, M. Vibration and wave propagation in ribbed plates. *Journal of the Acoustical Society of America 57*, 2 (1975), 370–373.

[92] Sabourin, I. Measurement of airborne sound insulation of 8 wall assemblies; measurement of airborne and impact sound insulation of 29 floor assemblies. Report Nordic Engineered Wood Report, 2015-07-23, National Research Council Canada, July 2015.

[93] Santoni, A., Bonfiglio, P., and Fausti, P. Predicting sound radiation efficiency and sound transmission loss of orthotropic cross-laminated timber panels. In *Proceedings of Acoustics '17 Boston* (Boston, Massachusetts, June 2017).

[94] Santoni, A., Schoenwald, S., Fausti, P., and Tröbs, H. Modelling the radiation efficiency of orthotropic cross-laminated timber plates with simply-supported boundaries. *Applied Acoustics 143* (2019), 112–124.

[95] Santoni, A., Schoenwald, S., Van Damme, B., and Fausti, P. Determination of the elastic and stiffness characteristics of cross-laminated timber plates from flexural wave velocity measurements. *Journal of Sound and Vibration 400* (2017), 387–401.

[96] Schmid, G., Kingan, M., Panton, L., Willmott, G., Yang, Y., Decraene, C., Reynders, E., and Hall, A. On the measurement and prediction of rainfall noise. *Applied Acoustics 171*, 107636 (2021), 1–17.

[97] Schoenwald, S., Zeitler, B., King, F., and Sabourin, I. Acoustics - sound insulation in mid-rise wood buildings. Report Nordic Engineered Wood Report, 2014-12-31, National Research Council Canada, December 2014.

[98] Schoenwald, S., Zeitler, B., Sabourin, I., and King, F. Sound insulation performance of cross laminated timber building systems. In *Proceedings of Internoise 2013* (Innsbruck, Austria, September 2013).

[99] Schroeder, M. Die statistischen Parameter der Frequenzkurven von grossen Räumen. *Acta Acustica united with Acustica 4* (1954), 595–600.

[100] Sen Gupta, G. Natural flexural waves and the normal modes of periodically-supported beams and plates. *Journal of Sound and Vibration 13* (1970), 89–101.

[101] Shield, B., and Hopkins, C. *Acoustic design of schools.* Building Bulletin 93, The Stationary Office, London, UK, 2003.

[102] Shorter, P., and Langley, R. On the reciprocity relationship between direct field radiation and diffuse reverberant loading. *Journal of the Acoustical Society of America 117*, 1 (2005), 85–95.

[103] Shorter, P., and Langley, R. Vibro-acoustic analysis of complex systems. *Journal of Sound and Vibration 288*, 3 (2005), 669–699.

[104] Siano, D., Viscardi, M., and Panza, M. Acoustic optimization of a high-speed train composite sandwich panel based on analytical and experimental transmission loss evaluation integrated by FE/Test correlation analysis. *Energy Procedia 81* (2015), 689–703.

[105] Squicciarini, G., Thompson, D., and Corradi, R. The effect of different combinations of boundary conditions on the average radiation efficiency of rectangular plates. *Journal of Sound and Vibration 333* (2014), 3931–3948.

[106] Tadeu, A., and António, J. M. P. Acoustic insulation of single panel walls provided by analytical expressions versus the mass law. *Journal of Sound and Vibration 257*, 3 (2002), 457–475.

[107] Van Belle, L., Claeys, C., Deckers, E., and Desmet, W. The impact of damping on the sound transmission loss of locally resonant metamaterial plates. *Journal of Sound and Vibration 461* (2019), 114909.

[108] Van Belle, L., Rocha de Melo Filho, N., Clasing Villanueva, M., Claeys, C., Deckers, E., Naets, F., , and Desmet, W. Fast metamaterial design optimization using reduced order unit cell modeling. In *Proceedings of the International Conference on Noise and Vibration Engineering ISMA2020* (Leuven, Belgium, September 2020).

[109] Van Damme, B., Schoenwald, S., Blanco, M., and Zemp, A. Limitations to the use of homogenized material parameters of cross laminated timber plates for vibration and sound transmission modelling. In *Proceedings of the 22nd International Congress of Sound and Vibration* (Florence, Italy, July 2015).

[110] Van Damme, B., Tröbs, H., and Schoenwald, S. Frequency dependent material properties to model the dynamics of cross laminated timber. In *Proceedings of the international conference on noise and vibration engineering* (Leuven, Belgium, September 2016).

[111] Van den Wyngaert, J. *Numerical prediction and optimization of the sound insulation of wall systems.* PhD thesis, KU Leuven, 2020.

[112] Van den Wyngaert, J., Schevenels, M., and Reynders, E. Broadband acoustic shape optimization of studs in double-leaf walls. *Journal of Sound and Vibration 485* (2020), 115562.

[113] Vanbelle, L. *Vibro-acoustic performance of locally resonant metamaterials with damping.* PhD thesis, KU Leuven, 2019.

[114] Vastiau, J., Decraene, C., Van hoorickx, C., and Reynders, E. Impact sound prediction of multilayered structures with the (modal) transfer matrix method. In *Proceedings of the 29th International Conference on Noise and Vibration Engineering, ISMA 2020* (Leuven, Belgium, September 2020).

[115] Ver, I. Impact noise isolation of composite floors. *The Journal of the Acoustical Society of America 50*, 4 (1971), 1043–1050.

[116] Vermeir, G. *Bouwakoestiek*, 2nd ed. Acco, Leuven, Belgium, 1999.

[117] Vigran, T. *Building Acoustics*. Taylor & Francis, Oxon, UK, 2008.

[118] Vigran, T. Predicting the sound reduction index of finite size specimen by a simplified spatial windowing technique. *Journal of Sound and Vibration 325*, 3 (2009), 507–512.

[119] Villot, M., Guigou, C., and Gagliardini, L. Predicting the acoustical radiation of finite size multi-layered structures by applying spatial windowing on infinite structures. *Journal of Sound and Vibration 245*, 3 (2001), 433–455.

[120] Villot, M., and Guigou-Carter, C. Using spatial windowing to take the finite size of plane structures into account in sound transmission. In *Proceedings of Novem 2005* (Biarritz, France, 2005).

[121] Viveen, P. *Wat voor badkamer vloer op houten vloer*. Verbouwkosten, 2020 (accessed December 19, 2020). `https://www.verbouwkosten.com/vloer/wat-voor-badkamer-vloer-op-houten-vloer/`.

[122] Wang, J., Lu, T., Woodhouse, J., Langley, R., and Evans, J. Sound transmission through lightweight double-leaf partitions: theoretical modelling. *Journal of Sound and Vibration 286* (2005), 817–847.

[123] Wang, P. *Prediction with uncertainty quantification of the impact sound radiation from complex floors*. PhD thesis, KU Leuven, 2019.

[124] Wang, P., Van hoorickx, C., Lombaert, G., and Reynders, E. Numerical prediction and experimental validation of impact sound radiation by timber joist floors. *Applied Acoustics 162*, 107182 (2020), 1–17.

[125] Weaver, R. On the ensemble variance of reverberation room transmission functions, the effect of spectral rigidity. *Journal of Sound and Vibration 130*, 3 (1989), 487–491.

[126] Williams, E., and Maynard, G. Numerical evaluation of the Rayleigh integral for planar radiators using the FFT. *The Journal of the Acoustical Society of America 72*, 6 (1982), 2020–2030.

[127] World Health Organization Regional Office for Europe. *Burden of disease from environmental noise: Quantification of healthy life years lost in Europe*. Copenhagen, Denmark, 2011.

[128] Xin, F., and Lu, T. Analytical and experimental investigation on transmission loss of clamped double panels: Implication of boundary effects. *The Journal of the Acoustical Society of America 125*, 3 (2009), 1506–1517.

[129] Yang, Y., Mace, B., and Kingan, M. Prediction of sound transmission through, and radiation from, panels using a wave and finite element method. *The Journal of the Acoustical Society of America 141*, 4 (2017), 2452–2460.

[130] Yang, Y., Mace, B., and Kingan, M. Vibroacoustic analysis of periodic structures using a wave and finite element method. *Journal of Sound and Vibration 457* (2019), 333–353.

[131] Yang, Y., Mace, B., and Kingan, M. A wave and finite element based homogenised model for predicting sound transmission through honeycomb panels. *Journal of Sound and Vibration 463* (2019), 114963.

[132] Zhou, R., and Crocker, M. Boundary element analyses for sound transmission loss of panels. *The Journal of the Acoustical Society of America 127*, 2 (2010), 829–840.

Curriculum vitae

Carolina Anne-Marie A. Decraene
° 28 June 1993, Sint-Niklaas, Belgium

Education

September 2016 - January 2021
PhD courses:

- ACOUTECT Summer School organized at the Acoustic Research Unit, the University of Liverpool (2018)
- ISAAC30 courses on Advanced Techniques in Applied and Numerical Acoustics organized at the Department of Mechanical Engineering, KU Leuven (2019)

September 2014 - June 2016
MSc in Architectural Engineering, KU Leuven
Thesis: "Efficient modelling of mid-frequency sound radiation and sound transmission for thick and layered walls."
Magna cum Laude

September 2011 - June 2014
BSc in Architectural Engineering, KU Leuven
Magna cum Laude

September 2009 - June 2011

Latijn-Wiskunde (8 uur), Heilige Familie Sint-Niklaas

Professional experience

September 2016 - January 2021
PhD in Engineering Science, Department of Civil Engineering, KU Leuven

Financing:

- 4 year PhD grant of Research Foundation-Flanders
- 4 months ERC Starting Grant under the Horizon 2020 framework program, project 714591 VirBAcous
- Grant for a long stay abroad from Research Foundation-Flanders

September 2016 - January 2021
Teaching assistant, Department of Civil Engineering, KU Leuven
for the following courses:

- Bouwakoestiek (B-KUL-H06M6A). Edwin Reynders (6 ECTS):

  During the academic years: 2016-2017, 2017-2018, 2018-2019, 2019-2020, 2020-2021
- Sterkteleer, deel 1 (B-KUL-H08Z8A). Geert Lombaert en Els Verstrynge (3 ECTS):

  During the academic years: 2018-2019, 2019-2020, 2020-2021
- Sterkteleer, deel 2 (B-KUL-H08W1A). Geert Lombaert en Stijn François (3 ECTS):

  During the academic years 2016-2017, 2017-2018
- Projectwerk multidisciplinaire bouwteams (B-KUL-H03Q5A). Staf Roels (6 ECTS), 2017-2018

for the following thesisses:

- Joren Vanherck. Development of Innovative Experimental techniques for low-frequency airborne sound insulation assessment. (2016-2017)

  Supervisor: Edwin Reynders; Assistant: Carolina Decraene
- Marjolein Faché. Acoustic optimization of laminated glazing in residential and office buildings. (2017- 2018)

  Supervisor: Edwin Reynders; Assistant: Carolina Decraene

- Karl Lauwers. Sound insulation of cross laminated timber walls and floors (2018-2019)

  Supervisor: Edwin Reynders; Assistants: Pengchao Wang, Carolina Decraene

- Dries Lams. (2020-present)

  Supervisor: Edwin Reynders; Assistants: Carolina Decraene, Daniele Giannini

August 2017 - July 2019
BAP representative of the Structural Mechanics Section

January 2017 - February 2019
Project engineer, Department of Civil Engineering, KU Leuven

for the following internal reports:

- C. Decraene, and E. Reynders. Voorstudie naar de ontwikkeling van een akoestische bouwknopenatlas: voorspelling van de lucht- en contactgeluidisolatie in een appartementsgebouw te Malle. Report BWM-2017-01, Department of Civil Engineering, KU Leuven, May 2017.

- C. Decraene, and E. Reynders. Voorstudie naar de ontwikkeling van een akoestische bouwknopenatlas deel 2a: gedetailleerde en vereenvoudigde analyse van een bouwsysteem met doorlopende betonvloeren, wanden in metselwerk en elastische tussenlagen. Report BWM-2017-09, Department of Civil Engineering, KU Leuven, July 2017.

- C. Decraene, and E. Reynders. Ontwikkeling van een akoestische bouwknopenatlas deel 2b: parametrische analyse van zes bouwconcepten met elastische muurstroken. Report BWM-2018-01, Department of Civil Engineering, KU Leuven, January 2018.

- C. Decraene, J. Van den Wyngaert, C. van hoorickx, and E. Reynders. Ontwikkeling van een akoestische bouwknopenatlas deel 3: experimentele validatie van de vereenvoudigde voorspellingsmethode in een proefgebouw in het Wienerberger Technicum. Report BWM-2018-11, Department of Civil Engineering, KU Leuven, September 2018.

- W. Stalmans, C. Decraene, and E. Reynders. Ontwikkeling van een akoestische bouwknopenatlas deel 4: vergelijkende studie tussen de voorspellingsmethode en de BACPRO rekentool. Report BWM-2019-07, Department of Civil Engineering, KU Leuven, June 2019.

March 2019 - May 2019 Academic visitor, Acoustics group, Department of Mechanical Engineering, the University of Auckland

Publications

Papers published in ISI journals

[1] C. Decraene, A. Dijckmans, and E. P.B. Reynders. Fast mean and variance computation of the diffuse sound transmission through finite-sized thick and layered wall and floor systems. Journal of Sound and Vibration, 422:131-145, 2018.

[2] G. Schmid, M.J. Kingan, L. Panton, G.R. Willmott, Y. Yang, C. Decraene, E. Reynders, and A. Hall. On the measurement and prediction of rainfall noise. Applied Acoustics, 171:107636, 2021.

Papers under review in ISI journals

[1] C. Decraene, G. Lombaert, and E. P.B. Reynders. Prediction of diffuse sound transmission through finite-sized periodic structures. Journal of Sound and Vibration. In preparation.

Papers published or accepted for publication in proceedings of international conferences

[1] E. Reynders, A. Dijckmans, and C. Decraene. Accounting for modal behavior in the efficient prediction of the sound transmission through layered walls and floors. Proceedings of the 45th International Congress and Exposition on Noise Control Engineering, INTER-NOISE 2016, pages 1108-1114, Hamburg, Germany, August 2016.

[2] C. Decraene, A. Dijckmans, and E. Reynders. A hybrid transfer matrix - statistical energy analysis approach to robust sound transmission modelling. Proceedings of the 6th Conference on Noise and vibration emerging methods, NOVEM 2018, pages 356-364, Ibiza, Spain, May 2018.

[3] C. Decraene, A. Dijckmans, and E. Reynders. Robust sound transmission modelling of finite-sized built-up walls and floors. Proceedings of ISMA2018 and USD2018, pages 4371-4381, Leuven, Belgium, September 2018.

[4] C. Decraene, E. Reynders, and G. Lombaert. Prediction of the sound transmission loss of two-dimensional periodic structures with a hybrid framework. Proceedings of the 23rd International Congress on Acoustics, ICA 2019, pages 1200-1207 Aachen, Germany, September 2019.

[5] C. Decraene, G. Lombaert, and E. Reynders. Predicting the sound transmission through simply supported building elements using a modal periodic structure theory. Proceedings of ISMA2020 and USD2020, pages 2413-2424, Leuven, Belgium, September 2020.

[6] J. Vastiau, C. Decraene, C. van hoorickx, and E. Reynders. Impact sound prediction of multilayered structures with the (modal) transfer matrix method. Proceedings of ISMA2020 and USD2020, pages 1761-1776, Leuven, Belgium, September 2020.

[7] C. Decraene, G. Lombaert, and E. Reynders. Accounting for modal behaviour in the prediction of sound transmission through periodic structures. Proceedings of e-Forum Acusticum 2020, December, 2020.

Other contributions at national conferences and meetings

[1] C. Decraene, A. Dijckmans, and E. Reynders. Efficient modeling of sound transmission through finite-sized thick and layered wall and floor systems. Acoustics '17 Boston, June 2017.

[2] C. Decraene, A. Dijckmans, and E. Reynders. Predicting the mean and variance of the sound transmission loss of finite sized walls and floors in the mid-frequency ranges. 4th ABAV PhD and Young Acousticians Day, Brussels, March 2018.

FACULTY OF ENGINEERING SCIENCE
DEPARTMENT OF CIVIL ENGINEERING
STRUCTURAL MECHANICS SECTION
Kasteelpark Arenberg 40, bus 2448
B-3001 Leuven (Belgium)
carolina.decraene@kuleuven.be
https://bwk.kuleuven.be/bwm